To the Graduate Council:

I am submitting herewith a thesis written by Scott Glenfield Tennent entitled "Experimental Investigation of a Confined Vortex Flow" I have examined the final copy of this thesis for form and content and recommend that it be accepted in partial fulfillment of the requirements for the degree of Master of Science, with a major in Aerospace Engineering.

Ahmad D Vakili, Major Professor

We have read this thesis
and recommend its acceptance:

Accepted for the Council:

Associate Vice Chancellor
and Dean of The Graduate School

STATEMENT OF PERMISSION TO USE

In presenting this thesis in partial fulfillment of the requirements for a Master's degree at the University of Tennessee, Knoxville, I agree that the Library shall make it available to borrowers under rules of the Library. Brief quotations from this thesis are allowable without special permission, provided that accurate acknowledgment of the source is made.

Permission for extensive quotation from or reproduction of this thesis may be granted by my major professor, or in his absence, by the Head of Interlibrary Services when, in the opinion of either, the proposed use of the material is for scholarly purposes. Any copying or use of the material in this thesis for financial gain shall not be allowed without my written permission.

Signature Scott [signature]

Date 24 Aug 93

EXPERIMENTAL INVESTIGATION OF A CONFINED VORTEX FLOW

A Thesis

Presented for the

Master of Science

Degree

The University of Tennessee, Knoxville

Scott Glenfield Tennent

December 1993

ACKNOWLEDGMENTS

I would like to thank my major professor, Dr. Ahmad Vakili, for his guidance and patience. I would also like to thank the other committee members, Dr. Ching Lo and Dr. James Wu for their comments and assistance in preparing this thesis. Furthermore, I would like to thank the laboratory staff of the University of Tennessee Space Institute for their valuable assistance in preparing and conducting the experiments. The guidance and expertise of Dr. N.R. Pauchapakesan was essential in conducting the hot film measurements. This research would not have been possible without funding granted by the Arnold Engineering Development Center. Finally, I would like to thank my parents, Richard and Lucene Tennent, for their love and encouragement over the past twenty six years.

ABSTRACT

This research attempted to quantitatively characterize the velocity field of a confined vortex in both single cell and multi cell modes as part of a larger research program attempting to understand the relationships between vortex stability and unsteady excitations. Although the motivation for the research program was to gain insight into vortex stability characteristics of the high pressure arc heater, the research results will have broad applications to many fluid dynamic problems.

An experimental program was conducted which obtained quantitative measurements in a water tunnel model geometrically similar to a high pressure arc heater. Single cell vortex data agreed well with the Burgers Vortex Model. Data was also obtained which will support the development of a three cell vortex theory. An analysis was conducted which addresses the similarity and utility of using water to simulate the high temperature air environment of the arc heater.

TABLE OF CONTENTS

CHAPTER PAGE

LIST OF TABLES

LIST OF FIGURES

FIGURE		PAGE

FIGURE PAGE

LIST OF SYMBOLS

C_P	Specific heat (constant pressure)
Dc	Diameter of Constrictor Region
$\bar{E}$	Output voltage of hot film instrument
$\bar{E}_c$	Temperature corrected hot film instrument voltage output
Ec	Eckert Number
f_{0_z}	Disturbance Frequency (Axial)
f_{0_θ}	Disturbance Frequency (Tangential)
f_z	Frequency of the Periodic Response (Axial)
f_z'	Frequency characteristic (Axial)
$f_{\dot{z}}'$	Frequency characteristic of the mass injection (Axial)
f_θ	Frequency of the Periodic Response (Tangential)
f_θ'	Frequency characteristic (Tangential)
$f_{\dot{\theta}}'$	Frequency characteristic of the mass injection (Tangential)
$\bar{f}_\theta$	Frequency of the Bulk Fluid = $\frac{V_\theta}{\pi D_c}$
g	Gravitational constant
h	Film Coefficient
I_s	Current through hot film wire in probe
k	Coefficient of thermal conductivity
k_f	Thermal conductivity of fluid at film temperature
l	length of film in probe
Lc	Length of Constrictor Region
$\dot{m}_i$	Mass flux entering at heater model constrictor station i
$\dot{m}_t$	Total Mass flux through heater model

Nu	Nusselt Number
P	Pressure
R	Hotwire resistance at arbitrary temperature
R_a	Resistance of hot film wire in probe at fluid ambient condition
R_{ac}	Resistance of hot film wire in probe at corrected ambient temperature
R_{cab}	Resistance of Cable
R_{in}	Internal resistance of circuit
R_r	Reference resistance at Reference temperature
R_s	Resistance of hot film wire in probe at over-heat condition wrt. ambient conditions
R_{sc}	Resistance of hot film wire in probe at over-heat condition wrt. corrected ambient temperature
T	Arbitrary temperature
T_a	Temperature of fluid ambient
T_{ac}	Corrected fluid ambient temperature
T_f	Temperature of the film $T_f = \frac{(T_s + T_a)}{2}$
T_r	Reference temperature
T_s	Temperature of hot film wire in probe at overheat condition wrt. ambient conditions
U	Magnitude of Local Velocity in the plane of the Hot film
U'	Magnitude of Total Local Velocity Vector
$\overline{U}_{eff}, V_{eff}$	Effective Velocity, velocity obtained by converting $\overline{E}$ to velocity using King's Law
$U'_{Parallel}$	Magnitude of Total Velocity Vector Parallel to Hot film
U'_{Perp}	Magnitude of Local Velocity Vector Perpendicular to Hot film
V	Average Axial Velocity
V_r	Local Radial Velocity

V_Z	Local Axial Velocity
V_θ	Local Tangential Velocity
α	Resistance temperature dependence coefficient
α_{OH}	Overheat ratio
β	Coefficient of thermal expansion
δ_z	Axial Distance Between mass injection stations
δ_θ	Circumfrential distance between slots
ϕ	Angle from flow axis to laboratory axis (See Figure B-1)
Γ_c	Circulation Measured at edge of wall boundary layer
μ	Coefficient of viscosity
θ	Angle from probe axis to laboratory axis (See Figure B-1)
Θ	Temperature difference (T_{wall} - $T_{stagnation}$)
ρ	Density
ψ	Angle from flow axis to probeaxis (See Figure B-1)

CHAPTER I

INTRODUCTION

Many fluid engineering applications utilize vortex flows. Performance of such systems is directly coupled to the generation, strength, and structure of the vortices involved. Vortex stability is a critically important parameter in many such fluid dynamic applications. One such application is the operation of an arc heated wind tunnel (Figure 1-1)*. This application requires a confined, high pressure air vortex to contain the path of a twenty-five megawatt electric arc. Breakdown of this vortex can result in nearly total destruction of the arc heater in a fraction of a second. Presently, the breakdown phenomenon is only empirically understood. Although a number of studies have been performed on the vortex stability and breakdown under various conditions, no theoretical model exists which predicts the vortex stability characteristics. However, both theoretical and experimental evidence indicate that both steady and unsteady interactions dramatically influence vortex breakdown. Better understanding of the physical mechanism involved would lead to the development of a rigorous theoretical foundation for the prediction of vortex burst. This would lead to control concepts in addition to more efficient design and engineering. Based on the present knowledge as evidenced in the open literature, geometry may play a critical role on the longevity of a confined vortex. In order to better understand the confined vortex stability and the factors which influence it, detailed experimental investigations and further theoretical analysis are necessary.

The present study is an experimental investigation of the vortex structure in a model geometrically similar to the Arnold Engineering Development Center (AEDC) H1 Arc Heater. Because of the adverse environment of the arc heater, the investigation is

* All figures are located in Appendix F.

performed using water. The water medium provides a reasonable level of similarity at low cost and with minimal risk. This model allows detailed flow measurement and flow visualization information to be gathered.

This thesis is composed of seven chapters. Chapter two describes the level of similarity between the water tunnel model and the arc heater, and introduces relevant theoretical models for stable vortex structures. This is accomplished after a formal analysis of the relevant parameters of each system, the flow field fluid mechanics, and the influences of non fluid mechanic phenomenon, such as the electromagnetic field generated by the arc. Chapter three outlines the objectives and requirements of the experimental study, focusing on developing accuracy specifications for the instrumentation. Chapter four details the experimental approach, including the selection and description of the instrumentation, as well as a test plan that outlines the specific steps taken to ensure obtaining quality data. Chapter five presents the results of the experimental study. Chapter six compares the data obtained to appropriate vortex models and discusses the feasibility of developing a three cell vortex model. Finally, Chapter seven concludes the study with recommendations for further study focusing on both the arc heater problem and the more generic vortex stability problem.

CHAPTER II

BACKGROUND

Literature Review

Extensive experimental and theoretical work has been performed in studies on vortex dynamics using both air and water as a medium. In this chapter, we will first review the physics of the arc heater in more detail, focusing on the fluid environment; attempts to model this environment computationally; and the effects of the arcs induced electromagnetic field on the fluid mechanics. Second, we will review previous work in the UTSI water tunnel in order to obtain qualitative insight into the possible types of vortex structures likely to be encountered in a geometry similar to AEDC's H1 heater. Third, we will review three vortex models which quantitatively characterize both single cell and two cell vortex velocity fields. And finally, we will explore previous efforts to define the effect of unsteady influences to the vortex core.

Arc Heater Description

In order to simulate the environmental conditions encountered during trans-atmospheric flight, ground test facilities must produce high total temperature and total pressure conditions. Although several devices (Shock Tubes, Hot Shot Facilities, and Impulse facilities) can simulate these severe conditions for a fraction of a second, arc heaters are the only viable devices available to produce adequate simulation conditions for several seconds or minutes necessary for several test types, such as: Aerothermal protection, scramjet combustor performance, antenna window cooling, and bore-sight error [1].

The Arnold Engineering Development Center (AEDC) operates the free world's largest high pressure segmented arc heaters [1]. AEDC is actively involved in expanding the reliability and capability of segmented arc heaters. In its effort to develop a technology base for the design of larger scale heaters, AEDC has identified a number of major development issues, one of which is understanding vortex breakdown at high circulation strengths.

Spatial stabilization of the arc is maintained by confining the high temperature, low density, current conducting gas to the centerline of the heater via a positive radial pressure gradient. This is accomplished by introducing the proper circulation needed to maintain a stable vortex (of some structure). Minimum circulation is defined as the minimum amount necessary to produce a sufficient radial inward centripetal force on the heated gas to offset the radial outward electromagnetic force acting on the current of the arc, thereby preventing discharge to the wall. Maximum circulation is defined as the highest circulation which will produce a steady vortex. The operational needs of the air flow inside the heater are not constant. In order to allow proper attachment at the electrodes, circulation must be below the minimum value. However, in the middle of the heater, it is essential that the circulation remain between the minimum and maximum limits.

The vortex created by the mass of air injected via the swirl rings is assumed to be of the forced type with the following attributes:

a) The circulation is zero at the centerline and increases continuously radially until the wall boundary layer.

b) The vorticity level at the core is high due to the rapid change in circulation.

c) The vorticity is convected with the gas and flows with it out through the throat.

d) Since the gas at the core of the vortex has a low average angular momentum, it must have lost momentum through friction with the wall, Therefore, the core flow is assumed to come from the wall boundary layer.

The mechanism for vortex breakdown is assumed to be as follows:

a) As the average circulation is increased, the centerline pressure, relative to the wall pressure, decreases.

b) The static pressure on the centerline at some axial position will become greater than the value at some upstream location, setting up an adverse pressure gradient. This adverse pressure gradient can be caused by:

1) Diffusion of circulation from the wall toward the centerline, raising the centerline pressure downstream.

2) Gas heating, decreasing the gas density, reducing radial pressure drop (increasing centerline pressure downstream).

3) Increase in channel area, resulting in a decrease in axial velocity, decreasing radial pressure drop.

c) A new stagnation point will form at that point, resulting in reverse flow on the centerline downstream of that point.

One may assume [2] that the arc must pass through heated gas. In other words, the temperature of the gas must be sufficiently high to cause ionization, allowing sufficient free electrons to support a continuous discharge on the order of 1000 Amperes. This gas will be of low density due to the high temperature, and therefore contained near the centerline of the heater due to the radial momentum equation.

Calculations based on arc visualization data [3] indicate that the actual arc diameter is approximately 0.5 inch at the anode, and tapers to 0.1-0.2 inch at the cathode (downstream end). At any given instant, only 2.8% by volume and 0.3% by mass of the gas inside the heater is resident in the arc. However, due to observed arc fluctuations, it is estimated that approximately 5% of the total mass will pass through the arc. This gas is assumed to reach 12,000^{o}K, while the rest of the gas is heated gradually from about 1000^{o}K near the anode to about 4000^{o}K near the cathode.

A computational analysis using an equilibrium air model and axi-symmetric geometry performed by Felderman [2] provides some useful insight into the effect of arc heating to the local thermodynamic properties. Before one can properly interpret the results of these calculations, one must consider the assumptions made in constructing the solution:

a) Axi-symmetric constant diameter tube: Neither the anode nor the cathode geometry was modeled.

b) Wall Roughness: A smooth wall was assumed instead of a ridged wall as found in the real heater.

c) The arc was assumed to occupy the centerline position instead of a time dependent path.

d) The swirl of the flow was artificially reduced (approximately 50%) in order to allow solution convergence.

e) The flow was assumed steady state instead of time dependent.

The results of Felderman's calculations are presented in Figures 2-1 through 2-5. The exact numerical values are not as important as the general trends in the properties. The following observations are especially noteworthy:

a) The gas temperature gradient is much more severe in the radial direction than in the axial direction.

b) The radial temperature gradient is most sever upstream, and gradually flattens out down stream.

c) The temperature at the wall can be a factor of ten lower than that of the centerline.

d) The density of the gas is a factor of at least three greater at the wall than at the centerline.

e) Axial velocity increases by a factor of four along the constrictor, yet the tangential velocity remains about the same. Therefore the swirl number:

$$\frac{\text{Tangential Velocity}}{\text{Axial Velocity}} = \frac{\Gamma}{D_c U_z} \qquad (2.1)$$

is greatest upstream, but gradually tapers off as the flow travels downstream.

f) Viscosity is highest on the centerline, but reduces by a factor of five at the wall.

The influence of the electromagnetic effects on the fluid dynamic variables was performed by MacDermott and Felderman [4]. The current in the arc and its associated magnetic field combine to produce a force governed by the Biot-Savart law. These forces produce three possible effects:

a) Pinch Forces: These forces tend to constrict the arc radially

b) Kink Forces: If there is a kink (helix type) in the arc, these forces will tend to force the arc toward the wall, contributing to arc instability.

c) Axial Forces: These forces tend to contract the arc axially if it were severed at the ends.

The assumed path of the arc in the heater indicates that the pinch force is the largest force of the three. It's influence to the aerodynamics of the heater shows up in the radial momentum equation:

$$\frac{\partial P}{\partial r} + \bar{J} \times \bar{B} - \frac{\rho V_\theta^2}{r} = 0 \qquad (2.2)$$

At even the highest current operation condition of the heater, the effect of the Biot-Savart Law term on pressure is very small compared to the steady state conditions (Figure 2-6). However, one may notice that the effect is on the same order as the radial pressure gradient due to swirl near the wall. Therefore, although the electromagnetic effects do not significantly change the operating condition of the heater, they may effect the stability of the core gas.

Previous UTSI Water Tunnel Work

Rigney [5] used a geometrically scaled Plexiglas model of the AEDC H1 arc heater to make qualitative observations of the flow structure using water as the fluid medium. She observed both three cell and single cell vortex structures in the constrictor region of the heater. A laser sheet photograph of the water tunnel model and the real arc heater (Figure 2-7) show good qualitative agreement. It is logical to conclude from Rigney's study, and Felderman's calculations that both single cell and multi cell vortices are present in the real arc heater. Therefore, it is important to characterize both types quantitatively.

Vortex Models

There are several theoretical vortex models used to analyze subsonic flows. Although none are general enough to describe the time dependent problem, they do provide some valuable insights into expected steady-state features. Three in particular will be described here. The first models the quasi-free, unconfined, single cell vortex; while the second and third model the confined, two-cell vortex. No known theory addresses the three cell vortex.

<u>Burgers Vortex Model:</u> Burgers' model [6] is based on the following assumptions:

a) Single Cell, Unconfined Vortex

b) Steady State, Axi-symmetric

c) $\frac{\partial}{\partial z}$ of the physical quantities is small

d) Radial Velocity V_r only depends on r

e) Axial velocity V_z must be a linear function in Z.

f) Boundary condition $V_{\theta\text{-}b}$, and $V_{r\text{-}b}$ defined

g) Constant fluid properties (Constant density, v_t/v, etc.)

Even with these seemingly restrictive conditions, the Burgers model does predict a vortex structure which behaves like a forced vortex near the centerline, and like a free (potential flow) vortex away from the centerline. His solution is an exact solution to the three dimensional Navier Stokes equation.

$$V_r' = \frac{V_r}{V_{rb}} = \frac{r}{b} \tag{2.3}$$

$$V_\theta' = \frac{V_\theta}{V_{\theta_{boundary}}} = \frac{1}{r'} \cdot \frac{1 - \exp(-R_{eb} \cdot r'^2 / 2) R_{eb}}{[1 - \exp(-R_{eb}/2)]} \tag{2.4}$$

$$V_z = f_0 + f(r) \cdot z \tag{2.5}$$

where f(r) is a constant. Reb is defined as:

$$R_{eb} = -\frac{b \cdot V_{rb}}{v_t} \tag{2.6}$$

The expression for V_θ' converges to:

$$V_\theta' = \frac{1}{r'} \tag{2.7}$$

for high Reynolds numbers (free vortex), and converges to:

$$V_\theta' = \frac{R_{eb}}{2[1 - \exp(-R_{eb}/2]} \cdot r' \tag{2.8}$$

for low Reynolds numbers (forced vortex). From these equations, one can define r_a', the radius corresponding to the maximum tangential velocity, $V_{\theta M}'$, as well as r_0', the radius corresponding to 99% of V_θ of the free vortex (Figure 2-8):

$$r_a' = \frac{1.59}{\sqrt{R_{eb}}} \tag{2.9}$$

$$r_0' = \frac{3.04}{\sqrt{R_{eb}}} \tag{2.10}$$

Figure 2-9 shows shapes of V_θ for various values of Re_b.

Experiments in water performed by Faler and Leibovich [7] agree well with the Burgers model (Figure 2, [7]). Their model had tangential fluid injection at one axial location with downstream fluid ejection.

One may also apply the Burgers model to the arc heater CFD calculations performed by Felderman. This application is tenuous at best since the arc heater flow field, although low speed, has high gradients in density and temperature. However, the turbulent viscosity only varies by about fifty percent from centerline to core. The table below summarizes the application of the Burgers model at an axial station midway through the constrictor of the heater.

Table 2-1: Burgers model Applied to Arc Heater

Parameter	**Centerline (nominal)**	**Wall (nominal)**
μ_t [N-Sec/M^2]	0.011	0.1
ρ [Kg/M^3]	1.5	10
ν_t (μ_t/ρ)	.0073	0.01
Re_b	0.79	0.58
r'_a	1.79	2.08

One may notice that the radius of maximum velocity is far greater than unity. Therefore one would expect a forced vortex behavior throughout, as the Felderman calculations show (Figure 2-3). However, it is conceivable that for some conditions, at some axial station, there could be a combined vortex (forced/ free) structure.

Sullivan Vortex Model: Sullivan [6] describes a two cell confined vortex which also satisfies the Navier Stokes equations. In this model, the flow does not always spiral in toward the centerline, but may spiral toward a finite radius r. Inside that radius, the flow spirals out in radius and upstream axially, creating a two cell structure (Figure 2-10). His model is based on the same assumption as Burgers' except V_z is a function of r multiplied by z instead of a linear function of z. The resulting equations of motion are:

$$V_r = -a \cdot r + 6(\frac{\nu}{r})[1 - \exp(-\frac{a \cdot r^2}{2\nu})] \tag{2.11}$$

$$V_\theta = \frac{\Gamma}{2\pi r}[\frac{H(\{a \cdot r^2\}/2\nu)}{H(Infinite)}] \tag{2.12}$$

$$V_z = 2 \cdot a \cdot z[1 - 3 \cdot \exp(-\frac{a \cdot r^2}{2\nu})] \tag{2.13}$$

where,

$$H(x)=\int_0^x \exp\{-t+3\int_0^t[\frac{1-\exp(-\tau)}{\tau}]d\tau\}dt \tag{2.14}$$

Numerical solutions of the above equations are presented in graphical form in Figure 2-11 for three Reynolds numbers. It is interesting to note that the existence of the two cell structure is dependent on the Reynolds number.

Ogawa Combined Vortex model: Like the Burgers model, the Ogawa model [6] defines both a quasi-forced vortex flow region (0< r < Rt) and a quasi-free vortex flow region (Rt < r < Ro), (Figure 2-12). This model is based on the following assumptions:

a) incompressible flow

b) negligible effects due to external body force

c) axi-symmetric flow

Separate assumptions about the velocity components are made for each region.

Quasi-forced Region:

$$V_r=-f\cdot r \tag{2.15}$$

$$V_\theta=Kr(1-\Lambda r) \tag{2.16}$$

$$V_z=2fz+V_{z0} \tag{2.17}$$

Quasi-free Region:

$$V_r=-\frac{m}{r} \tag{2.18}$$

$$V_\theta=\frac{\Gamma_n}{r^n} \tag{2.19}$$

$$V_z=V_{z1} \tag{2.20}$$

where

$$K=\frac{2V_{\theta M}}{a} \tag{2.21}$$

$$\Lambda=\frac{(1+n)}{(2+n)r_t}=\frac{1}{2a} \tag{2.22}$$

$$f=\frac{m}{r_t^2} \tag{2.23}$$

$$\frac{V_{\theta M}}{V_0} = \frac{1}{4}\left(\frac{2+n}{1+n}\right)^2 \cdot \left(\frac{D_1 - D_0}{2r_t}\right)^n \tag{2.24}$$

$$\Gamma_n = K r_t^{(1+n)} (1 - \Lambda r_t) \tag{2.25}$$

where **n** characterizes the energy dissipation (n = 1 for a free vortex, no dissipation, irrotational flow; and n = 0 for a forced vortex, solid body rotation).

The Burgers model will be compared to the single cell data later. No data will be available to compare directly to the two cell theories of Sullivan and Ogawa. However, if the underlying assumptions about the flow field are the same for two cell vortices (as stated by Sullivan and/or Ogawa) as three cell vortices (experimental data), then one would have faith that a three cell theory could be developed.

Vortex Core Disturbances

Observations of stable real vortex tube flows reveal small perturbations both spatially and temporally. Visually, these disturbances appear as core lumpiness and slight helical core wanderings. Mathematically, these small disturbances have been described as Tollmien-Schlichting waves, the first indication of laminar instability. A cursory analysis is presented later on in this chapter. The relationship between the nature of flow instabilities and overall vortex stability has been investigated by several authors. According to Chanaud [8], there are two possible causes of vortex breakdown. The first is that breakdown is caused by amplification of infinitesimal disturbances. The second is that the breakdown phenomenon is the result of an abrupt change between two basic types of rotating flows. Khorrami and Grosch [9] investigated instability growth rates in both single and two cell vortices and concluded that the growth rates of disturbances in multi-cell vortices are substantially higher than in single cell vortices. The authors even go so far as to suggest that an efficient mechanism to break down unwanted vortices is to induce a multi-cell structure. Vakili, et. al. [10], [11] have shown that the introduction of small forcing with a pulsing jet of fluid along the axis of the vortex at certain frequencies can stabilize a vortex in conditions that would otherwise result in vortex burst, or conversely, destroy a vortex in otherwise stable flow conditions. This suggests a strong coupling between forcing frequencies and naturally occurring disturbance frequencies. From the literature, one can conclude that it is important to characterize the dominant modes of natural disturbances as a prelude to investigating the vortex breakdown phenomenon.

Theoretical Analysis

From the discussion in the previous section, one can conclude that a more detailed understanding of the interactions between the fluid mechanics of the vortex and the boundary conditions is needed to identify the key parameters to focus an experimental investigation of the factors which influence the behavior of the vortex. First, a non-dimensional analysis was performed to identify all potential and key parameters. This was accomplished using the Buckingham-PI theorem [12]. Second, the equations of motion (continuity, momentum, and energy) were nondimensionalized in order to identify the key steady fluid mechanic parameters, narrowing the list obtained in the first analysis. Finally, a stability analysis was initiated to determine which factors could contribute to the instability of the vortex.

Dimensional Analysis

There are twenty five possible parameters (listed below) associated with the arc heater and the water tunnel model that could be relevant to the internal flow field. For simplicity, only the parameters associated with the constrictor region are considered. In order to evaluate the parameters properly, they must be grouped into non-dimensional terms. The Buckingham Pi theorem provides a structured approach. The dimensions of all twenty five variables are listed below:

Dimensions

Mass [M], Length [L], Time [T], Temperature [Θ]

L_c, D_c, δ_z, δ_θ	[L]
Θ	[Θ]
$f_\theta, f_z, f_{0_\theta}, f_{0_z}, f'_\theta, f'_z, f'_{\theta}, f'_{z}$	$[{}^{1}\!/_{T}]$
V	$[{}^{L}\!/_{T}]$
Γ_c	$[{}^{L^2}\!/_{T}]$
$\dot{m}_i$, $\dot{m}_t$	$[{}^{M}\!/_{T}]$
P	$[{}^{M}\!/_{LT^2}]$
ρ	$[{}^{M}\!/_{L^3}]$
μ	$[{}^{M}\!/_{LT}]$
C_p	$[{}^{L^2}\!/_{T^2\Theta}]$
k	$[{}^{ML}\!/_{T^3\Theta}]$
β	$[{}^{1}\!/_{\Theta}]$
g	$[{}^{L}\!/_{T^2}]$
h	$[{}^{M}\!/_{T^3\Theta}]$

Axial Analysis The frequency of the periodic response (Axial), f_z, is some function of the following nineteen variables:

$$f_z = f(L_c, D_c, \delta_z, \dot{m}_i, \dot{m}_t, V, P, \rho, \Theta, \mu, C_p, k, \Gamma, g, h, \beta, f'_z, f'_z, f_{0_z}) \tag{2.26}$$

(Any variation in diameter, representing a converging or diverging duct, may be viewed in the same way as D_C). These twenty variables contain only the dimensions [M], [L], [T], and [Θ]. In following the Buckingham Pi theorem of dimensional analysis, the following four repeating parameters are chosen: L_c, ρ, V, Θ. One would then expect (twenty parameters - four primary dimensions) sixteen non dimensional Pi factors ($\Pi_1, \Pi_2, \ldots \Pi_{16}$).

$$\Pi_1 = [M^0 L^0 T^0] = L_c^a \rho^b V^c \Theta^d D_c = {}^{D_c}\!/_{L_c} \tag{2.27}$$

$$\Pi_2 = [M^0 T^0 L^0] = L_c^a \rho^b V^c \Theta^d \delta_z = {}^{\delta_z}\!/_{L_c} \tag{2.28}$$

$$\Pi_3 = [M^0T^0L^0] = L_c^a\rho^bV^c\Theta^d\dot{m}_c = \dot{m}_c \big/ \rho V L_c^{\,2} \tag{2.29}$$

$$\Pi_4 = [M^0T^0L^0] = L_c^a\rho^bV^c\Theta^d\dot{m}_c = \dot{m}_t \big/ \rho V L_c^{\,2} \tag{2.30}$$

$$\Pi_5 = [M^0T^0L^0] = L_c^a\rho^bV^c\Theta^d\Gamma = \Gamma \big/ L_cV \tag{2.31}$$

$$\Pi_6 = [M^0T^0L^0] = L_c^a\rho^bV^c\Theta^d f_z = L_cf_z \big/ V \tag{2.32}$$

$$\Pi_7 = [M^0T^0L^0] = L_c^a\rho^bV^c\Theta^d f_z' = L_cf_z' \big/ V \tag{2.33}$$

$$\Pi_8 = [M^0T^0L^0] = L_c^a\rho^bV^c\Theta^d f_{\dot{z}}' = L_cf_{\dot{z}}' \big/ V \tag{2.34}$$

$$\Pi_9 = [M^0T^0L^0] = L_c^a\rho^bV^c\Theta^d f_{0_z} = L_cf_{0_z} \big/ V \tag{2.35}$$

$$\Pi_{10} = [M^0T^0L^0] = L_c^a\rho^bV^c\Theta^d P = P \big/ \rho V^2 \tag{2.36}$$

$$\Pi_{11} = [M^0T^0L^0] = L_c^a\rho^bV^c\Theta^d \mu = \mu \big/ \rho V L_c \tag{2.37}$$

$$\Pi_{12} = [M^0T^0L^0] = L_c^a\rho^bV^c\Theta^d C_p = C_p\Theta \big/ V^2 \tag{2.38}$$

$$\Pi_{13} = [M^0T^0L^0] = L_c^a\rho^bV^c\Theta^d k = \Theta k \big/ L_c\rho V^3 \tag{2.39}$$

$$\Pi_{14} = [M^0T^0L^0] = L_c^a\rho^bV^c\Theta^d \beta = \beta\Theta \tag{2.40}$$

$$\Pi_{15} = [M^0T^0L^0] = L_c^a\rho^bV^c\Theta^d g = gL_c \big/ V^2 \tag{2.41}$$

$$\Pi_{16} = [M^0T^0L^0] = L_c^a\rho^bV^c\Theta^d h = \Theta h \big/ \rho V^3 \tag{2.42}$$

A functional relationship exists between the sixteen Pi factors:

$$f_1(\Pi_1, \Pi_2, \Pi_3, \ldots \Pi_{16}) = 0 \tag{2.43}$$

Tangential Analysis The frequency of the periodic response (Tangential), f_θ, is some function of the following nineteen variables:

$$f_\theta = f(L_c, D_c, \delta_\theta, \dot{m}_i, \dot{m}_t, V, P, \rho, \Theta, \mu, C_p, k, \Gamma, g, h, \beta, f_\theta', f_{\dot{\theta}}', f_{0_\theta}) \tag{2.44}$$

These twenty variables contain only the dimensions [M], [L], [T], and $[\Theta]$. In following the Buckingham Pi theorem of dimensional analysis, the following four repeating parameters are chosen: D_c, ρ, V, Θ. One would then expect (twenty parameters - four primary dimensions) sixteen non dimensional Pi factors $(\Pi_1, \Pi_2, \ldots \Pi_{16})$. Many of these parameters will merely be the same as the pi factors derived in the axial analysis, multiplied by the aspect ratio, Π_1. Only five unique Pi factors will be introduced:

$$\Pi_{17} = [M^0T^0L^0] = D_c^a \rho^b V^c \Theta^d \delta_z = \delta_\theta / D_c \qquad (2.45)$$

$$\Pi_{18} = [M^0T^0L^0] = D_c^a \rho^b V^c \Theta^d f_\theta = D_c f_\theta / V \qquad (2.46)$$

$$\Pi_{19} = [M^0T^0L^0] = D_c^a \rho^b V^c \Theta^d f'_\theta = D_c f'_\theta / V \qquad (2.47)$$

$$\Pi_{20} = [M^0T^0L^0] = D_c^a \rho^b V^c \Theta^d f'_{\dot{\theta}} = D_c f'_{\dot{\theta}} / V \qquad (2.48)$$

$$\Pi_{21} = [M^0T^0L^0] = D_c^a \rho^b V^c \Theta^d f_{0_\theta} = D_c f_{0_\theta} / V \qquad (2.49)$$

A functional relationship exists between these five factors and eleven of the previous sixteen factors:

$$0 = f_2(\Pi_1, \Pi_3 \ldots \Pi_5, \Pi_{10} \ldots \Pi_{21}) \qquad (2.50)$$

Most of these Pi factors consist of familiar physical relations:

Π_1 - Aspect Ratio

Π_2 - Wall Roughness (Axial)

Π_3 - Mass Flux Coefficient (Entering tangentially through constrictor station i)

Π_4 - Mass Flux Coefficient (Total mass flow through heater)

Π_5 / Π_1 - $\frac{\Gamma}{D_c V}$ - Swirl Number

Π_6 - Strouhal Number (Longitudinal Response)

Π_{10} - Pressure Coefficient

Π_{11} - 1/ Reynolds Number (Based on Length)

$\frac{\Pi_{11}}{\Pi_1}$ - $\frac{\mu}{\rho V D_c}$ - 1/Reynolds Number (Based on Diameter)

Π_{12} - 1/Eckert Number

Π_{13} - 1/[Prandtl number][Eckert number][Reynolds number (Length)]

$\frac{\Pi_{14}\Pi_{15}}{\Pi_{11}^2}$ - $\frac{\beta \Theta g L_c \mathrm{Re}_{L_c}}{V^2}$ - Grashof Number

Π_{15} - 1/ Froude Number

$\frac{\Pi_{16}}{\Pi_{13}}$ - $\frac{hL}{k}$ - Average Nusselt Number

Π_{17} - Wall Roughness Tangential

$\frac{\Pi_{18}\Pi_1}{\Pi_5}$ - $\frac{f_\theta}{\bar{f}_\theta}$ Dimensionless Frequency (Fluid response)

Π_{18} - Strouhal number (tangential response)

One may notice that six Pi factors (Π_7- Π_9, Π_{19}-Π_{21}) are not involved in any of the above recognized dimensionless terms. All six are frequency based (four characteristic frequencies, and two forcing frequencies). These frequency based Pi factors can be related to other terms to create additional dimensionless frequencies.

$\frac{\Pi_1^2}{\Pi_5}\Pi_7$ - $\frac{f_z'}{\bar{f}_\theta}$ - Dimensionless Frequency (Axial Characteristic)

$\frac{\Pi_1^2}{\Pi_5}\Pi_8$ - $\frac{f_{\bar{z}}'}{\bar{f}_\theta}$ - Dimensionless Frequency (Axial Characteristic, mass injection)

$\frac{\Pi_1^2}{\Pi_5}\Pi_9$ - $\frac{f_{0_z}}{\bar{f}_\theta}$ - Dimensionless Frequency (Axial Disturbance Frequency)

$\frac{\Pi_1}{\Pi_5}\Pi_{19}$ - $\frac{f_\theta'}{\bar{f}_\theta}$ - Dimensionless Frequency (Tangential Characteristic)

$\frac{\Pi_1}{\Pi_5}\Pi_{20}$ - $\frac{f_{\bar{\theta}}'}{\bar{f}_\theta}$ - Dimensionless Frequency (Tangential Characteristic, mass injection)

$\frac{\Pi_1}{\Pi_5}\Pi_{21}$ - $\frac{f_{0_\theta}}{\bar{f}_\theta}$ - Dimensionless Frequency (Tangential Disturbance Frequency)

The strength of the Buckingham Pi theorem is that it can identify all of the relevant parameters. However, it gives no insight into the importance of each parameter. For this insight, one must first apply the relevant physical laws, and only afterward rely on engineering judgment. The most insightful physical relations are the non-dimensionalized equations of motion (Mass, momentum and energy). The following section derives these relations in polar coordinates.

Non-Dimensionalized Flow Equations

The first step in non-dimensionalizing the equations is to non-dimensionalize the independent variables:

$$r^* = r/R_0 \tag{2.51}$$

$$z^* = z/R_0 \tag{2.52}$$

$$\Theta^* = \Theta \tag{2.53}$$

$$V_r^* = Vr/V_0 \tag{2.54}$$

$$V_\theta^* = V_\theta/V_0 \tag{2.55}$$

$$V_z^* = V_z/V_0 \tag{2.56}$$

$$P^* = (P-P_0 + \rho g r \cos\theta)/\rho V^2 \tag{2.57}$$

$$\rho^* = \rho/\rho_0 \tag{2.58}$$

$$T^* = (T-T_0)/(T_w-T_0) \tag{2.59}$$

$$t^* = tV_0/R_0 \tag{2.60}$$

$$\mu^* = \mu/\mu_0 \tag{2.61}$$

$$k^* = k/k_0 \tag{2.62}$$

$$Cp^* = Cp/Cp_0 \tag{2.63}$$

The next step is to substitute the non dimensional parameters into the flow equations.

Continuity Equation: The continuity equation in general form is:

$$\frac{\partial \rho}{\partial t} + \nabla\cdot(\rho V) = 0 \tag{2.64}$$

expressed in cylindrical coordinates:

$$\frac{\partial \rho}{\partial t} + \frac{1}{r}\frac{\partial}{\partial r}(r\rho V_r) + \frac{1}{r}\frac{\partial}{\partial \theta}(\rho V_\theta) + \frac{\partial(\rho V_z)}{z} = 0 \tag{2.65}$$

One should note that this form of the continuity equation applies only to a region between two injection stations. A more general expression would have to consider the mass injection boundary condition.

Substitute in Non- dimensional parameters:

$$\frac{\rho_0 V_0}{R_0}\left[\frac{\partial \rho^*}{\partial t^*}+\frac{1}{r^*}\frac{\partial}{\partial r^*}(r^*\rho^* V_r^*)+\frac{1}{r^*}\frac{\partial}{\partial \theta^*}(\rho^* V_\theta^*)+\frac{\partial(\rho^* V_z^*)}{z^*}\right]=0 \tag{2.66}$$

Dividing through by $\frac{\rho_0 V_0}{R_0}$, yields:

$$\frac{\partial \rho^*}{\partial t^*}+\frac{1}{r^*}\frac{\partial}{\partial r^*}(r^*\rho^* V_r^*)+\frac{1}{r^*}\frac{\partial}{\partial \theta^*}(\rho^* V_\theta^*)+\frac{\partial(\rho^* V_z^*)}{z^*}=0 \tag{2.67}$$

No non dimensional parameters introduced.

<u>Momentum Equation</u> The momentum equation can be expressed as:

$$\rho\frac{DV}{Dt}=-\nabla P+F+\mu\nabla^2 V \tag{2.68}$$

Where

$$F=\rho\vec{g} \tag{2.69}$$

$$\rho=\rho_0(1-\beta\Delta \mathrm{T}) \tag{2.70}$$

$$\vec{g}=-g\cos\theta\hat{r}+g\sin\theta\hat{\theta} \tag{2.71}$$

Therefore:

$$F_r=-\rho_0 g\cos\theta+\rho_0\beta(\mathrm{T}-\mathrm{T}_0)g\cos\theta \tag{2.72}$$

$$F_\theta=\rho_0 g\sin\theta-\rho_0\beta(\mathrm{T}-\mathrm{T}_0)g\sin\theta \tag{2.73}$$

$$F_z=0 \tag{2.74}$$

The momentum equation can now be written in component form:

r direction:

$$\begin{aligned}&\rho\left(\frac{\partial V_r}{\partial t}+V_r\frac{V_r}{r}+\frac{V_\theta}{r}\frac{\partial V_r}{\partial r}+V_z\frac{V_r}{z}-\frac{V_\theta^2}{r}\right)=\\&-\frac{\partial}{\partial r}(P+\rho g r\cos\theta)+\rho_0\beta(\mathrm{T}-\mathrm{T}_0)g\cos\theta+\mu\left(\frac{\partial^2 V_r}{\partial r^2}+\frac{1}{r}\frac{\partial V_r}{\partial r}+\frac{1}{r^2}\frac{\partial^2 V_r}{\partial \theta^2}+\frac{\partial^2 V_r}{\partial z^2}-\frac{V_r}{r^2}-\frac{2}{r^2}\frac{\partial V_\theta}{\partial \theta}\right)\end{aligned} \tag{2.75}$$

After substituting in non-dimensional parameters and dividing through by $\frac{\rho_0 V_0^2}{R_0}$, One obtains:

$$\rho^*\left(\frac{\partial V_r^*}{\partial t^*}+V_r^*\frac{\partial V_r^*}{\partial r^*}+\frac{V_\theta^*}{r^*}\frac{\partial V_r^*}{\partial \theta^*}+V_z^*\frac{\partial V_r^*}{\partial z^*}-\frac{V_\theta^{2*}}{r^*}\right)$$
$$=-\frac{\partial P^*}{\partial r^*}+\frac{Gr}{\mathrm{Re}^2}\beta^* g^* T^*\cos\theta+\frac{1}{\mathrm{Re}}\left(\frac{\partial^2 V_r^*}{\partial r^{2*}}+\frac{1}{r^*}\frac{\partial V_r^*}{\partial r^*}+\frac{1}{r^{2*}}\frac{\partial^2 V_r^*}{\partial \theta^{2*}}+\frac{\partial^2 V_r^*}{\partial z^{2*}}-\frac{V_r^*}{r^{2*}}-\frac{2}{r^{2*}}\frac{\partial V_\theta^*}{\partial \theta^*}\right) \tag{2.76}$$

Where:

$$Gr=\frac{g_0\beta_0\rho_0^2R_0^3(T_w-T_0)}{\mu_0^2} \tag{2.77}$$

and:

$$\mathrm{Re}=\frac{\rho_0 V_0 R_0}{\mu_0} \tag{2.78}$$

Similar exercises can be done for the θ, and Z direction, but no new parameters will be found.

Energy equation (enthalpy form):

$$\rho\frac{\partial h}{\partial t}=\frac{DP}{Dt}+div(k\nabla T)+\Phi+\left[\frac{\partial Q}{\partial t}+\nabla\cdot q_{rad}\right] \tag{2.79}$$

Expressed in polar coordinates:

$$\rho\left[\frac{\partial h}{\partial t}+V_r\frac{\partial h}{\partial r}+\frac{V_\theta}{r}\frac{\partial h}{\partial \theta}+V_z\frac{\partial h}{\partial z}\right]=\left[\frac{\partial P}{\partial t}+V_r\frac{\partial P}{\partial r}+\frac{V_\theta}{r}\frac{\partial P}{\partial \theta}+V_z\frac{\partial P}{\partial z}\right]+\frac{1}{r}\frac{\partial}{\partial r}\left(rk\frac{\partial T}{\partial r}\right)+\frac{1}{r^2}+\frac{\partial}{\partial \theta}\left(k\frac{\partial T}{\partial \theta}\right)+\frac{\partial}{\partial z}\left(k\frac{\partial T}{\partial z}\right)$$
$$+\mu\left\{2\left[\left(\frac{\partial V_r}{\partial r}\right)^2+\left(\frac{1}{r}\frac{\partial V_\theta}{\partial \theta}+\frac{V_r}{r}\right)^2+\left(\frac{\partial V_z}{\partial z}\right)^2\right]+\left(\frac{1}{r}\frac{\partial V_z}{\partial \theta}+\frac{\partial V_\theta}{\partial z}\right)^2+\left(\frac{\partial V_r}{\partial z}+\frac{\partial V_z}{\partial r}\right)^2+\left(\frac{1}{r}\frac{\partial V_r}{\partial \theta}+\frac{\partial V_\theta}{\partial r}-\frac{V_\theta}{r}\right)^2\right\}+\left[\frac{\partial Q}{\partial t}-\nabla\cdot q_{rad}\right] \tag{2.80}$$

If one assumes that $h=C_p(T-T_0)$, substitutes in non dimensional factors, and multiplies through by $\dfrac{R_0}{V_0\rho_0C_{p_0}(T_w-T_o)}$ one obtains:

$$
\begin{aligned}
&\rho^{*}C_{p}{}^{*}\left[\frac{\partial h^{*}}{\partial t^{*}}+V_{r}{}^{*}\frac{\partial h^{*}}{\partial r^{*}}+\frac{V_{\theta}{}^{*}}{r^{*}}\frac{\partial h^{*}}{\partial \theta^{*}}+V_{z}{}^{*}\frac{\partial h^{*}}{\partial z^{*}}\right]\\
&=Ec\left\{\frac{\partial P^{*}}{\partial t^{*}}+V_{r}{}^{*}\frac{\partial P^{*}}{\partial r^{*}}+\frac{V_{\theta}{}^{*}}{r^{*}}\frac{\partial P^{*}}{\partial \theta^{*}}+V_{z}{}^{*}\frac{\partial P^{*}}{\partial z^{*}}\right]+\\
&\frac{1}{\mathrm{Pr}\mathrm{Re}}\left[\frac{1}{r^{*}}\frac{\partial}{\partial r^{*}}\left(r^{*}k^{*}\frac{\partial T^{*}}{\partial r^{*}}\right)+\frac{1}{r^{*2}}+\frac{\partial}{\partial \theta^{*}}\left(k^{*}\frac{\partial T^{*}}{\partial \theta^{*}}\right)+\frac{\partial}{\partial z^{*}}\left(k^{*}\frac{\partial T^{*}}{\partial z^{*}}\right)\right]\\
&+\frac{Ec}{\mathrm{Re}}\left\{2\left[\left(\frac{\partial V_{r}}{\partial r}\right)^{2}+\left(\frac{1}{r}\frac{\partial V_{\theta}}{\partial \theta}+\frac{V_{r}}{r}\right)^{2}+\left(\frac{\partial V_{z}}{\partial z}\right)^{2}\right]+\left(\frac{1}{r}\frac{\partial V_{z}}{\partial \theta}+\frac{\partial V_{\theta}}{\partial z}\right)^{2}+\left(\frac{\partial V_{r}}{\partial z}+\frac{\partial V_{z}}{\partial r}\right)^{2}+\left(\frac{1}{r}\frac{\partial V_{r}}{\partial \theta}+\frac{\partial V_{\theta}}{\partial r}-\frac{V_{\theta}}{r}\right)^{2}\right\}\\
&+\frac{R_{0}}{V_{0}\rho_{0}C_{p_{0}}(T_{w}-T_{0})}\left[\frac{\partial Q}{\partial t}-\nabla\cdot q_{rad}\right]
\end{aligned}
$$

(2.81)

Notice that the coefficient of bulk viscosity term has been neglected. The following similarity parameters fall out:

$$\mathrm{Pr}=\frac{\mu C_{p}}{k} \tag{2.82}$$

$$Ec=\frac{V^{2}}{C_{p}\theta} \tag{2.83}$$

$$\mathrm{Re}=\frac{\rho VD}{\mu} \tag{2.84}$$

Similarity Discussion

As one can see, the general equations are extremely complex. If one includes the time dependencies, both the water tunnel and the arc heater flow fields become nearly unsolvable. Instead of trying to solve the above equations in closed form, we will examine the individual terms of the equations in order to:

a) Introduce and baseline assumptions in a rigorous fashion.

b) Discuss similarity between flow in the water tunnel and the arc heater

c) Find the important parameters to be controlled and recorded during the water tunnel experiment.

Baseline Assumptions: In order to facilitate a comparison between the water tunnel and the arc heater, we must simplify the above equations as much as possible. These equations must be simplified separately for both the water tunnel and the arc heater cases.

Water tunnel: From the experimental results, one can clearly see a complex flow structure. At the test conditions, the flow field appeared nearly axi-symmetric with small perturbations. Therefore, we will analyze the flow field as a steady state plus perturbation. We will first re-examine the flow equations to gain insight into the physics underlying the steady case. This analysis will assume axi-symmetric flow with no time dependence.

<Continuity Equation>: Through flow visualization, and data obtained during preliminary testing, one can make the following assumptions:

a) Incompressible flow: V~10in/sec or M~0.001. Therefore,

b) Velocity gradients in the theta direction are much less than velocity gradients in the r, and z direction. Therefore

$$\frac{\partial V_{r,\theta,z}}{\partial \theta} << \frac{\partial V_{r,\theta,z}}{\partial r}, \frac{\partial V_{r,\theta,z}}{\partial z} \tag{2.85}$$

Therefore, we can rewrite the continuity equation:

$$\frac{\partial V_r *}{\partial r *} + \frac{V_r *}{r *} + \frac{\partial V_z *}{\partial z *} \approx 0 \tag{2.86}$$

Recall that this applies between mass injection locations. Because of the boundary layer growth along the constrictor wall between injection stations, we know that the net axial fluid velocity will increase in the axial direction. Therefore,

$$\frac{\partial V_z}{\partial z} > 0 \text{ so } (V_r + \frac{\partial V_r}{\partial r}) < 0 \tag{2.87}$$

at each streamwise station averaged. This relation has important consequences. If $\frac{\partial V_z}{\partial z}$ >0 everywhere (single cell vortex) outside the viscously dominated vortex core and wall boundary layer, then one of three cases must always be true:

Case 1: $\frac{\partial V_r}{\partial r}, \frac{V}{r} < 0$

$$\text{Case 2: } \frac{\partial V_r}{\partial r} > 0, \frac{V_r}{r} << 0$$
$$\text{Case 3: } \frac{\partial V_r}{\partial r} << 0, \frac{V_r}{r} > 0$$

Interpretation:

Case 1: Radial velocity would be lowest (largest negative) near the wall and continuously increase toward the centerline, where it would approach zero.

Case 2: Radial velocity would be lowest (largest negative) on the centerline and increase toward zero near the wall. This case is not physically possible for a single cell axi-symmetric vortex.

Case 3: Radial velocity would be highest on the centerline and decrease toward zero near the wall. This case is also not possible for a single cell axi-symmetric vortex.

Although Case 2 is the only condition applicable the single cell vortex, some combination of all three may be applicable to multi-cell vortices.

<Momentum Equation>: Because of the large Re of the water tunnel,

$$\mathrm{Re} \equiv \frac{V_\theta D_c}{\nu} \approx \frac{[0.3\frac{M}{Sec}][0.1M]}{[2x10^{-6}\frac{M^2}{\sec}]} \approx 15{,}000 \tag{2.88}$$

terms proportional to 1/Re number are small. Therefore, one can assume that viscosity is important only at the wall and at the vortex core (which may or may not be at the centerline). Furthermore, there is negligible temperature gradients (small Grashof number) within the flow. Including the assumptions described in the continuity equation, one can rewrite the momentum equations:

<<r direction>>:

$$(V_r * \frac{V_r *}{r *} + \frac{V_\theta *}{r *}\frac{\partial V_r *}{\partial r *} + V_z * \frac{V_r *}{z *} - \frac{V_\theta^2 *}{r *}) = -\frac{\partial P *}{\partial r *} \tag{2.89}$$

Assuming that

$$V_\theta^* >> V^*{}_r \text{ and } \frac{\partial V_r^*}{\partial r^*}, \frac{V_\theta^*}{r^*} \geq \frac{V_z^*}{z^*} \tag{2.90}$$

one can approximate:

$$\frac{V_\theta^2 *}{r *} \approx \frac{\partial P *}{\partial r *} \tag{2.91}$$

<<θ direction>>:

$$V_r * \frac{\partial V_\theta *}{\partial r *} + \frac{V_r *}{r *}\frac{\partial V_\theta *}{\partial \theta *} + V_z * \frac{\partial V_\theta *}{\partial z *} + \frac{V_r * V_\theta *}{r *} = -\frac{1}{r *}\frac{\partial P *}{\partial \theta *} \tag{2.92}$$

Based on the above assumptions, one can simplify: $\frac{\partial V_\theta}{\partial \theta} = 0$. Furthermore, in order to preserve constant circulation along a stream tube in the inviscid region, one can approximate that $\frac{\partial V_\theta}{\partial z} \approx 0$ since the stream tubes will be weak functions of z. Therefore, one can rewrite the momentum equation in the θ direction as:

$$V_r^*\left(\frac{\partial V^*_\theta}{\partial r^*} + \frac{V_\theta^*}{r^*}\right) = -\frac{1}{r^*}\frac{\partial P^*}{\partial \theta^*} \tag{2.93}$$

If we assume that the tangential pressure gradient is close to zero, then:

$$\frac{V_\theta}{r} \approx -\frac{\partial V_\theta}{\partial r} \tag{2.94}$$

Since V_θ is always positive, $\frac{\partial V_\theta}{\partial r} < 0$, or always decreasing as one moves from the centerline toward the wall. Experimental evidence shows that this is not the case even when the flow is very well behaved. Therefore, one is faced with one of the following conclusions (assuming Vr is predominantly negative):

a) $\frac{\partial P}{\partial \theta} > 0$ This would mean an adverse pressure gradient in the theta direction. This would be an excellent source for instability.

b) Viscous effects dominating. This option is highly unlikely.

c) Breakdown of one of the other previous assumptions.

The first conclusion is by far the most likely.

<<*Z Direction*>>: The nondimensionalized momentum equation in the z direction is (neglecting viscous terms):

$$\rho^*\left(\frac{\partial V_z^*}{\partial t^*}+V_r^*\frac{\partial V_z^*}{\partial r^*}+V_\theta^*\frac{\partial V_z^*}{\partial \theta^*}+V_z^*\frac{\partial V_z^*}{\partial z^*}\right)=-\frac{\partial P^*}{\partial Z^*} \tag{2.95}$$

Using the above assumptions, one can reduce this equation to:

$$\rho^*\left(V_r^*\frac{\partial V_z^*}{\partial r^*}+V_z^*\frac{\partial V_z^*}{\partial z^*}\right)=-\frac{\partial P^*}{\partial Z^*} \tag{2.96}$$

The impact of this equation is that it does not preclude a recirculating vortex in the minus z direction.

Since there is no temperature gradient or heat flow, there is no need to apply the energy equation to this flow field. The water tunnel is run for several minutes to reach steady state conditions before data is taken. Furthermore, the only mechanism for external heating is through frictional losses. This produces enough heat to raise the water temperature about one degree per hour. Therefore, one may assume that the water temperature is uniform both spatially and temporally.

Although we have assumed a well behaved single cell vortex for the constrictor flow, nothing in the above governing equations (in general form) precludes the displacement of the core off centerline or a multi cell vortex.

Arc Heater: The arc heater presents a much more difficult problem to analyze. The strong gradients in thermodynamic properties prevent any simplification of the Navier Stokes equations. Furthermore, the high temperatures near the core may require finite rate chemistry modeling for some portion of the flow. Although a general analysis of the arc heater flow is beyond the scope of this paper, some specific insights are attainable. An assessment of the continuity equation is difficult because of the lack of similarity parameters and the high density gradients. However, some sense can be made of the momentum equation. The Reynolds number of the heater is higher than that of the water tunnel:

$$\mathrm{Re} \equiv \frac{\rho U_\theta D_c}{\mu} \approx \frac{5[Kg/M^3]\cdot 200[M/\sec]\cdot 0.05[M]}{0.0001[NS/M^3]} = 500{,}000 \tag{2.97}$$

Furthermore, despite the high temperature gradients, one would still expect the Grashof number to be small compared to the Reynolds number squared.

$$\frac{Gr}{\mathrm{Re}^2} = \frac{gB_0\rho_0^2 D_c^{\,3}(T_w - T_0)\mu^2}{\mu^2\rho^2 U^2 D_c^{\,2}} = \frac{gB_0 D_c(T_w - T_0)}{U^2} = \frac{9.8(.05)B_0(T_w - T_0)}{(200)^2} \tag{2.98}$$

This is difficult to prove from the Grashof number itself, because the derivation of Grashof number is based on small gradients in temperature (not 10,000K in less than an inch), and small changes in density (not factors of ten). However, the purpose of this term is to compare convective driving forces to inertial forces. Despite the strong convective forces, 200 M/sec high density air circulating in a span of less than two inches will probably be inertia driven regardless of the temperature gradient. As a result, one may assume that the arc heater flow, like the water tunnel flow is not driven by viscosity or thermal convection.

Arc Heater - Water Tunnel Similarity: Through the above analysis, it is possible to make an attempt to ascertain the level of similarity between the arc heater and the water tunnel. Once the limitations and opportunities of this similarity are understood, reasonable and achievable test objectives can be established.

Similarity between the arc heater and the water tunnel is difficult to judge because of the arc heater flow field's severe gradients in bulk thermodynamic properties. One needs to be extremely careful applying incompressible models (Such as the Burgers Model) to the arc heater, even though the flow velocities are well in the subsonic regime. One puzzling aspect is the fact that Felderman's calculations indicate a forced vortex throughout the constrictor even though the Reynolds number of the arc heater is much higher than the water tunnel model which indicates a mixed free and forced vortex structure. One must keep in mind that in both the Water Tunnel and the Arc Heater an inviscid process is responsible for the vortex generation. Therefore, changes in flow structure with respect to Reynolds number may be of secondary importance rather than primary. Since the parameters involving bulk thermodynamic properties are impossible to simulate (Π_3,Π_4,Π_{10-16}) in the water tunnel model, we must adjust our similitude accordingly. The parameters which are possible to simulate are:

Π_1, Π_2,Π_5, Π_{17}, Geometry (Boundary condition) based

Π_{6-9},Π_{18-21}, Frequency based

The above factors, and their influence on vortex dynamics, should be the focus of water tunnel simulations. Once the influence of these parameters are understood, a comprehensive program involving computational simulation, cold and hot air tests, and full arc heater tests can be pursued with lower cost and risk to obtain the necessary insight to develop the tools outlined in the Introduction.

Important Parameters to Control in the Water Tunnel: As discussed in the previous section, the parameters which are most appropriate for the water tunnel to assess are related to the geometry, the boundary conditions, and the frequency of the flow field and its disturbances. Therefore, in this study , the independent controllable parameters are the tunnel model geometry (including water injection pattern), and the nature of the external disturbances. The dependent parameters important to record are the local swirl number (flow angle), and the frequencies of the flow field responses.

In addition, the steady state flow field must be quantitatively characterized in order to assess the type of vortex present (forced/ free, single cell/ multi cell, or any combination thereof). It is important to be able to compare the vortex pattern observed to theoretical and computational models of both the water tunnel and the arc heater both to validate the water tunnel as an important simulation tool, and to serve as a validating database for future vortex theories.

Perturbation Analysis

A stability analysis of the flow can be performed if an approximate analytical solution is available. In order to find out whether perturbations would cause a vortex breakdown or deviation from the approximate flow pattern, we will add a disturbance on the basic flow parameters of the form [13]:

$$\begin{aligned} &V = V_0 + v, P = P_0 + p \\ &v = \hat{u}, \hat{v}, \hat{w} \\ &\text{where } \hat{u}, \hat{v}, \hat{w}, p = f(r, \theta, z, t) \end{aligned} \tag{2.99}$$

We will assume these disturbances to be of the Tollmien-Schlichting form:

$$(\hat{v}_r, \hat{v}_\theta, \hat{v}_z, \hat{p}) = [\tilde{u}(r), \tilde{v}(r), \tilde{w}(r), \tilde{p}(r)]\exp[i\alpha\{r\cos(\theta - \theta_0)\cos\phi + z\sin\phi - ct\}] \tag{2.100}$$

These expressions will be substituted into the flow equations, as reduced from above. For the reader's convenience, they are summarized below:

$$\frac{\partial V_r^*}{\partial r^*} + \frac{V_r^*}{r^*} + \frac{\partial V_z^*}{\partial z^*} \approx 0 \tag{2.101}$$

$$\frac{V_\theta^{2*}}{r^*} \approx \frac{\partial P^*}{\partial r^*} \tag{2.102}$$

$$V_r\left(\frac{\partial V_\theta}{\partial r} + \frac{V_\theta}{r}\right) = -\frac{1}{r}\frac{\partial P}{\partial \theta} \tag{2.103}$$

$$\left(V_r^* \frac{\partial V_z^*}{\partial r^*} + V_z^* \frac{\partial V_z^*}{\partial z^*}\right) = -\frac{\partial P^*}{\partial Z^*} \tag{2.104}$$

If one forms the following expressions:

$$V_r = V_r + \hat{v}_r, V_\theta = V_\theta + \hat{v}_\theta, V_z = V_z + \hat{v}_z \tag{2.105}$$

and substitutes them in the above four equations, and subtract out the original equation, one obtains the following (the * notation has been dropped) linearized perturbation equations:

$$\frac{\partial \hat{v}_r}{\partial r} + \frac{\hat{v}_r}{r} + \frac{\partial \hat{v}_z}{\partial z} = 0 \tag{2.106}$$

$$\frac{2V_\theta \hat{v}_\theta}{r} \approx \frac{\partial \hat{p}}{r} \tag{2.107}$$

$$\hat{v}_r \frac{\partial V_\theta}{\partial r} + V_r \frac{\partial \hat{v}_r}{\partial r} + \frac{V_r \hat{v}_r}{r} = -\frac{1}{r}\frac{\partial \hat{p}}{\partial \theta} \tag{2.108}$$

$$V_r \frac{\partial \hat{v}_z}{\partial r} + \hat{v}_r \frac{\partial V_z}{\partial r} + V_z \frac{\partial \hat{v}_z}{\partial z} + \hat{v}_z \frac{\partial V_z}{\partial z} = -\frac{\partial \hat{p}}{\partial z} \quad (2.109)$$

In order to illustrate type of analysis performed, the perturbation equation is de-coupled into a θ and z component. We will illustrate the case for a perturbation in the z direction (no inclination angle). The perturbation expressions become:

$$(\hat{v}_r, \hat{v}_\theta, \hat{v}_z, \hat{p}) = [\tilde{u}(r), \tilde{v}(r), \tilde{w}(r), \tilde{p}(r)]\exp[i\alpha\{z - ct\}] \quad (2.110)$$

If one substitutes this equation into the above linearized perturbation equations, the following are obtained:

$$\tilde{v}_r'(r) + \frac{\tilde{v}_r(r)}{r} + \tilde{v}_z(r)[i\alpha] = 0 \quad (2.111)$$

$$\frac{2V_\theta \tilde{v}_\theta(r)}{r} \approx \frac{\partial \tilde{p}(r)}{r} \quad (2.112)$$

$$\tilde{v}_r(r)\frac{\partial V_\theta}{\partial r} + V_r \tilde{v}_r{}'(r) + \frac{V_r \tilde{v}_r(r)}{r} = 0 \quad (2.113)$$

$$V_r \tilde{v}_z'(r) + \tilde{v}_r(r)\frac{\partial V_z}{\partial r} + V_z \tilde{v}_z(r)[i\alpha] + \tilde{v}_z(r)\frac{\partial V_z}{\partial z} = -\tilde{p}\ (r)[i\alpha] \quad (2.114)$$

These four equations are coupled linear ordinary differential equations in $\tilde{v}_r, \tilde{v}_\theta, \tilde{v}_z$, and $\tilde{p}$. The other variables can be expressed as functions of r,θ, and z by curve fitting experimental data. Functions of θ are constant for the purpose of this analysis. Therefore, we have four equations and four unknown functions of r and z to find. One would then obtain the linearized stability equations for particular flow conditions and locations. Once validated, this information would be extremely valuable for identifying the envelope of frequencies which are likely to excite the vortex.

CHAPTER III

OBJECTIVES AND REQUIREMENTS OF THE EXPERIMENT

Exprerimental Objective

The primary objective of this study was to quantitatively characterize the velocity field in the water tunnel model. Since the flow field is low speed, the velocity field is described by an elliptic equation. The solution of this equation requires that the boundaries and all the inflow and outflow conditions be specified. Specifying Neuman boundary conditions is acceptable. Therefore, velocity profiles at two different axial stations, and mass flow rates through any tangential ports between the two stations must be known for each test condition. Two different conditions were chosen in order to characterize both single cell and combination single-cell multi-cell flow fields.

With the above objective in mind, a set of experimental requirements were developed in order to aid in the development of a test plan. Requirements are defined for the flow field measurements, and tunnel test conditions.

Flow field Measurement Requirements

Defining the velocity field requires velocity component measurements in all three directions (V_r,V_θ,V_z). Preliminary flow visualization studies revealed two important features of the flow. First, the flow field was mostly axi-symmetric. Therefore, obtaining velocity data at one theta station was validated. Second, the flow oscillations observed were small compared to the steady state values. Therefore, velocity measurements could be time averaged, while the oscillations could be measured (amplitude and frequency) separately.

Measurement Resolution

Because of the multi-cell nature of the flow field, large radial gradients were expected. Therefore, velocity measurements were needed every one tenth of an inch in the radial direction.

Measurement Accuracy

Developing accuracy requirements for measurements were necessary to ensure data of sufficient quality was obtained. Two factors drive the time averaged velocity flow field requirements. The first is determining the boundaries of the individual cells in a multi-cell structured vortex. The second is obtaining a discernible profile as a function of radius. The first factor also drives an accuracy requirement for angle measurements. An accuracy of +/- 10% for velocity, and +/- 5 degrees for angle were established. The requirements of the time accurate data (amplitude and frequency) were +/- 10% for amplitude and +/- 0.05 Hz for frequency. At first, the frequency requirement may seem stringent. However, the frequency range of interest was between 0.5 and 1 Hz.

Test Condition Requirement

The test condition is determined by the flow rate of water through the water tunnel circuit. Specifying accuracy requirements for the flow rate is important for four reasons. First, it establishes the repeatability of the test condition. Second, the tangential mass injection distribution is determined directly from flow rate measurements. Third, flow rate measurements serve as valuable checks to axial flow velocity measurements (conservation of mass). And fourth, variability of flow rate during a test will increase the error of the velocity measurements. The fourth reason imposes the most stringent requirement on flow rate measurements, requiring an accuracy of +/- 5%. The requirements are summarized in Table 3-1. A brief discussion of the actual error obtained is presented in Appendix E.

Table 3-1: Water Tunnel Accuracy Requirements

Parameter	Requirement	Actual
Velocity	+/- 10%	+/- 1 in/ sec
Angle	+/- 5 degrees	+/- 3 degrees
Radial Spatial Resolution	0.1 inch +/- .05 inch	+/- .05 inch
Amplitude	+/- 10%	< +/- 10%
Frequency	+/- .05 Hz	< +/- .16 Hz
Flow Rate	+/- 5%	+/- 6%

CHAPTER IV

EXPERIMENTAL APPROACH

Test Plan

Characterize the flow field qualitatively

Flow visualization data was necessary to obtain in order to select the test conditions, and develop the measurement requirements described in chapter three.

Select the instrumentation

The instrumentation (described in detail below) was selected to insure that the requirements detailed in chapter three were met economically within the scope of this study. A non-intrusive technique such as Laser Doppler Velocimetry or Particle Image Velocimetry would have provided the most accurate data. However, the cost and complexity associated with applying either of these techniques to the water tunnel model configuration to obtain three dimensional velocity data was traded for the simplicity of the hot film technique used in this study. Since both time averaged velocity measurements and time accurate fluctuation data was desirable, a single component hot film anemometer system was selected. Due to the extreme sensitivity of hot-wires to flow field temperature, obtaining accurate flow field temperatures was a must.

Calibrate the instrumentation

Most of the instrumentation was calibrated based on established standards prior to the program. The only devise requiring in-situ calibration was the hot film anemometer. A detailed account of the hot film calibration experience is given in appendix C.

Assess the instrumentation effects on the flow field

Since an intrusive velocity measurement system was selected, it was important to determine its effect on the flow field. Flow visualization techniques provided an adequate determination.

Obtain primary data:

As a result of the flow visualization data obtained in step a, flow rates of five gallons per minute and ten gallons per minute were chosen as the test conditions. At each condition, flow field velocity measurements were made at stations D and H (see Water Tunnel Model Description, later this Chapter). All four measurements were repeated at one half precision (velocity measurements at every 0.2 inches radius instead of 0.1) for validation purposes. The techniques used to obtain the velocity measurements are detailed in Appendix C. A summary of the test matrix is provided in Table 4.1.

Table 4.1: Water Tunnel Test Matrix

Run #	Station	Flow Rate	Precision
1	D	5 Gal/ min	Full
2	D	5	Half
3	H	5	Full
4	H	5	Half
5	D	10	Full
6	D	10	Half
7	H	10	Full
8	H	10	Half

Facility Description

Water Tunnel Circuit

The University of Tennessee Space Institute closed circuit water tunnel facility is substantially similar to the one used and described by Rigney [5]. Some of it's most important characteristics are:

a) 1,270 Gallon stainless steel stilling chamber with baffle plates

b) 6" Diameter PVC pipe circuit

c) Constant RPM pump capable of 25 gal/min pumping speed

The facility layout is shown in Figure 4-1. Since this experiment observed time accurate characteristics, some modifications to the facility as used by Rigney were necessary to reduce the possibility of water tunnel circuit effects on the data.

Rigney had used a variable RPM motor to control the flow rate in the circuit. It was felt that a variable frequency devise in an incompressible medium circuit could provide inconsistent influence to the data. We opted instead for a constant RPM motor. We controlled the flow rate by varying the amount of flow through the bypass line, or through an additional valve installed just above the stilling chamber. Flow rate was obtained by measuring the pressure drop across a baffle installed on the opposite side of the circuit from the water tunnel (see flow meter description, later this chapter).

Arc Heater Water Tunnel Model

The water tunnel model used in this description was nearly similar to the one used by Rigney. It is a two scale model of the AEDC H1 Arc Heater. Geometric similarity is preserved for all the major dimensions (Figures 4-2, and 4-3). Geometric aspects not correctly modeled are the exact mass distribution and the small scale perturbations along the arc heater wall. The effects of these geometric infidelities are an increase in the swirl number as compared to the real arc heater, and the elimination of a possible disturbance force.

Instrumentation Description

Hot Film Anemometer System

The hot film anemometer system included four different components: The hot film probe, which intrusively enters the flow; the probe injection device which positions the probe both with respect to depth (radius) and angle; the data acquisition system which contains the circuit necessary to balance the probe electronically, and record and display its output; and a calibration device used to calibrate the probe output to velocity and angle (see Appendix B).

Hot Film Probe - The hot film probe is a commercially available item from Thermo Systems Incorporated (TSI), Model 1210-20W. The diameter of the film is twenty microns. During this study, the film was replaced several times. However, all the final data was taken using one of two films. The properties of each are tabled below:

Table 4-2: Hot Film Probe Characteristics

	Probe $R_{100°C}$- $R_{0°C}$	**Probe R @ 0° C**	**Probe Internal R**
Hot film 1	1.47 Ohms	5.28 Ohms	0.20 Ohms
Hot film 2	1.41	5.67	0.20

This probe was specifically designed for water, and was operated well within its operational limits.

Probe injection Device - The probe injection device was constructed by UTSI laboratory technicians (Figure 4-4). It allowed for precise positioning (r direction, +/- 0.05 in) and orienting (Theta, +/- 2 degrees) of the probe, both in the water tunnel model and the calibration device.

Data Acquisition System - The data acquisition device was a commercially available item also from TSI, called the Intelligent Flow Analyzer 100. It is a constant temperature type anemometer. A complete description of the operation of the constant temperature anemometer is supplied in Appendix B.

Calibration Device - The hot film calibration device is shown in Figure 4-5. It was developed under a previous effort. Figure 4-5 shows the device with the hot film probe installed. The probe is translated horizontally in still water by a variable speed electric motor controlled by a personal computer. The probe is timed between two light sensitive diodes a known distance apart. The calculated velocity is correlated to the voltage output of the anemometer to obtain a probe velocity calibration (see Appendix B for calibration methodology). This device is used for both angle and velocity calibrations. The accuracy of the device has not been validated. Although the solid state electronics probably do not introduce significant error, there is a possibility of residual fluid velocities in the device introducing error. However, the repeatability of the velocity calibrations indicates that this error is also small (<5%).

Other Instrumentation

Thermometer - The temperature of both the water in the water tunnel and the calibration device was measured using an Omega Thermoelectric Type K thermometer. Although it may have had up to a two degree bias error from the true temperature, its precision was within 0.1 degrees. Since the same device was used to measure both the water tunnel temperature and the calibration water temperature, the 0.1 degree absolute error will be used in any analysis.

Flow Meter - Total water tunnel mass flow rate was measured using a device based on a Validyne differential pressure transducer. The devise is calibrated to SAME standards, with an error of 0.5% in pressure. It determines mass flow rate by measuring and comparing static pressure upstream and downstream of an orifice plate in the flow. Since mass flow rate scales as the square root of pressure, the mass flow rate is accurate to less than 0.5%.

Filter - A bypass type filter was installed to filter out fine rust particles (see Appendix A) that were contaminating the hot film probe. The device used was commercially available from Triton. It is capable of filtering solid particles down to the 10 micron range, while imposing a minimal pressure drop. Although effective at removing particles, it introduced undesirable flow disturbances. Therefore, the filter was not run during any of the data runs.

Flow Visualization Techniques

Flow Visualization data was obtained through the use of fluorescene dye. Its luminosity under ultraviolet light and viscosity properties were demonstrated by Rigney [5]. The dye was injected via a variable pressure device into twelve injection ports spaced evenly throughout the arc heater model (Figure 4-2). Images were recorded using a Video Camcorder, with selected frames scanned to provide the images seen in this thesis.

CHAPTER V

EXPERIMENTAL RESULTS

Preliminary Flow Visualization

Preliminary flow visualization successfully depicted both the single cell and three cell vortex structure. Furthermore, it validated the assumption that the flow field was steady enough to be analyzed as a steady state plus perturbations instead of a general time varying flow field. Figures 5-1 through 5-4 show the single cell structure present at Station H at 5.6 gallons per minute flow rate. Figures 5-5 through 5-8 show the three cell structure present at station D at 10 gallons per minute flow rate. For both flow rates station D exhibited three cell structure, while station H exhibited single cell structure. Extending to higher flow rates caused cavitation in the vortex core, while lower flow rates exhibited significant unsteady behavior. However, the lower flow rate exhibited single cell structure further up stream than the higher flow rate.

Facility Effects on the Flow Field

Since the prime objective of the experimental program was to determine the effect of disturbances on the vortex, it was important to know that the only significant disturbances would come from the mechanical forcing device. Preliminary runs indicated that tangential forcing frequencies of the order 0.7- 0.8 Hz significantly effected the vortex core. In order to asses the effect of the water tunnel circuit on the vortex core, the hot film probe was injected into the flow near the centerline ($r = 0.3$ inches, $\theta = 0$ deg), at Station D, at a tunnel flow rate of 10 gal/min. Figure 5-9 shows a fast fourier transform (amplitude vs frequency) of the anemometer output. Although the figure shows data only from 0 to 1 Hz, no appreciable oscillations were observed below 10 Hz. It appears that the predominant peak wanders (over an average of sixteen passes of frequency scans, each approximately thirty seconds long) between 0.74 and 0.88 Hz. Figure 5-9 supports the above observations, perhaps indicating a natural frequency of the flow field. Another important characteristic of the flow field is the low amplitude of the oscillations. Even the greatest peak amplitude is more than two orders of magnitude lower than the steady state value (~20 mV vs ~3V). In order to get an idea of the corresponding velocity fluctuation, one must apply a king's law calibration. Recall that the King's law is defined as:

$$E^2 = A + BV^n \tag{5.1}$$

Therefore,

$$\frac{\partial V}{\partial E} = \frac{2E}{nB}\left(\frac{E^2 - A}{B}\right)^{\frac{1}{n}-1} \tag{5.2}$$

Since the data was obtained at Station D, r= 0.3 in, 0 degree probe orientation, and a flow rate of 10 gal/min; one would expect nominally a 5 inch/ sec effective velocity at that orientation (Figure C-4). The corresponding king's law equation had the following factors: A = 1.075, B = 3.364, n = 0.337, Veff = 5 in/sec, E = 2.62 Volts. Therefore, $\frac{\partial V}{\partial E} = 13.5$. Since $\Delta V \approx \frac{\partial V}{\partial E}(\Delta E)$, then $\Delta V_{eff} \leq (13.5)\cdot(.025) = 0.34 \text{ in/sec}$. Therefore, it is reasonable to assume that disturbances to the vortex from facility operation are small. Similarly, any observed vortex motions are the result of the interaction between the internal arc heater model geometry and associated flow field.

Hot film effects on the flow field

Figures 5-10 through 5-12 show the effect of the probe interference at various radii. The dye was injected upstream of the probe injection location. One can see that the effect of interference is most severe near the centerline, decreasing in severity as the probe nears the wall. Steady state measurements obtained of a stable core structure are reasonably valid until very near the centerline. However, hot film anemometer would not be an effective technique for obtaining point velocity measurements in vortex structures which are marginally stable or transitioning from stable to unstable. Furthermore, in a multi-cell environment, the probability that significant disturbances will be fed "upstream" are substantially higher than for a single cell environment.

Calibration Results

Excellent calibration of the hot film was obtained before and after each test run. Detail of the calibration process is given in Appendix B.

Primary Data

Time Averaged Data

The reduced hot film data is presented in Figures 5-13 through 5-20. The data reduction technique is described in appendix B. All points in the proposed test matrix were successfully obtained. However, we were unable to generate a stable single cell structure throughout the entire water tunnel model. The lower flow rate (5.6 gal/min) exhibits slightly smaller swirl angles. Data near the centerline ($r < 0.4$ inches) will not meet the accuracy limit established earlier due to four factors:

a) Vortex core oscillations

b) Increased unsteadiness (turbulent flow) near the center of the vortex

c) The radius of curvature of the flow is on the same order as the length of the hot film.

d) Probe interference

Likewise, data gathered at radial stations greater than 1.6 inches for station D and 1.8 inches for station H will include unacceptable error. Station D is located near a water injection port. The close proximity of the water injection port tends to increase the local tangential velocity near the wall. However, this is a local effect, not an indication of the general vortex structure. Both stations D and H will encounter the local effects of the probe injection cavity near (r > 1.8 inches) the wall.

One may also notice that the verification data set for station D at high velocity (Run #6, as identified in table 4.1) is a full data set rather than a half data set. These two data sets were the first two final sets obtained and represent the transition between preliminary data and final data. Since they agreed so well, an additional half set was deemed unnecessary.

Mass injection information is derived indirectly by measuring the total mass flow through the water tunnel circuit, and assuming constant mass injection through each port in the constrictor. From Figures 5-15 and 5-19, it appears that the tangential velocity near the wall is relatively constant for a given flow rate as a function of position. Therefore, it appears that this assumption is at least valid in the constrictor. In the next chapter, this information will be used for a first order continuity equation check.

Time Accurate Data

Time accurate data were successfully obtained as planned. A typical spectrum of the frequency content is presented in figure 5-9.

CHAPTER VI

DISCUSSION

Continuity Check

A first indication for qualifying the velocities obtained through the hot film system is to perform a continuity check. Since flow rate through the injection orifices can not be measured accurately, only a qualitative check of continuity may be performed. One would expect that the mass flow through station H (downstream) would be greater than that through station D (upstream). Furthermore, the flow rate through either should be less than the total mass flow through the water tunnel. Appendix D describes a method for calculating mass flow rates from axial (V_Z) velocity profiles. In performing these calculations for station D, the axial velocity value for the 1.6 inch radial station was repeated for all radii greater than 1.6 inches, for reasons described in Chapter five. Similarly, the axial velocity values for the 1.8 inch radial station was repeated in the calculations for station H. There are sixteen injection stations upstream of station D, eleven between station D and H, and twenty six downstream of station H. The table below shows the values calculated for the primary data sets.

Table 6-1: Continuity Check

Location	Flow Rate (Gal/ min)	Flow Rate (Gal/ min)
Station D	1.32	1.54
Station H	3.05	6.16
Total	5.6	10.0

The above values (Table 6-1) appear very reasonable, especially the values for station H. Although the flow rate through each constrictor injection port is approximately the same for a given total flow rate, the flow rate through the ports in the anode and cathode (figure 4-2) are probably less (due to lower tangential velocity, resulting in reduced pressure drop). The flow patterns in the anode and cathode are extremely complex, and velocity dependent. Therefore, it is unlikely that the mass flow rate into them would scale linearly with increases in total flow rate. This is one possible explanation for why the ratio of flow rate through station D to flow rate through station H is not constant.

Another way to check the flow rate values is to determine the flow rate through each constrictor injection port between station D and H. If we assume that the flow rate is approximately the same through each, this is relatively straightforward. There are 44 (11 stations x 4 per station) injection ports between D and H, each 1/16 inch in diameter. According to experiments performed by Rigney [5], the flow rate through a hole this size would not exceed about 0.1 gal/min for reasonable pressure gradients. This is on the order of the flow rate predicted through each port at a water tunnel flow rate of 10 gal/min. It is reasonable to conclude that the calculated flow rate for Station D at 10 gal/min is slightly low.

Set to Set Comparisons

In most cases the data from the primary data run and the data from the corresponding verification data set agreed well. However, one comparison warrants closer attention. V_θ for station D at 10 gal/min (Figure 5-19) shows unacceptable disagreement between the two data sets. The source of the disagreement can be traced to the velocity calibration of the verification set. An enlargement of the calibration scale (Figure 6-1) reveals a velocity drift between the calibration before the tunnel run versus after the tunnel run (Classic case of particle accumulation as described in Appendix A).

The King's Law [14] curve fit appears to fit the data obtained after the run in the 6-8 in/sec range. Therefore, the King's law curve fit over predicts the velocity by probably one in/sec, especially for the outer radii. If one applied a one in/sec correction downward to the tangential velocity, the data would agree well with the prime data set.

Comparison with Theory

Several features of the velocity profile lend themselves to comparison with the vortex models described in Chapter 2.

Burgers model

Since this model is intended for use on single cell vortices, we will evaluate only the data from station H. Although this model is intended for use on an unconfined vortex, it does allow one to specify boundary conditions at some radial location. Most of the assumptions appear valid:

a) d/dz is small - from Figures 5-13 through 5-20, it appears that gradients with respect to z are small for all three velocity components.

b) Vr only depends on r - see Figure 5-13 and 5-17. Vr changes with respect to z are small. Flow visualization data indicate minimal flow dependence on theta.

c) Axi-symmetric, steady state flow field - Figure 5-9 indicates that the amplitude and velocity of the oscillations are much less than the steady state value. This was also confirmed through flow visualization.

d) Vz constant with respect to r - This assumption is more valid for the low flow rate case (if at all) than the high one (Figures 5-14 and 5-18).

Figures 6-2 through 6-5 show comparisons between values predicted by the Burgers model against data obtained at station H for both flow rates. Figure 6-2 and 6-3 were obtained by varying the turbulent viscosity of the Burgers Model in order to obtain the best fit to the data. Figures 6-4 and 6-5 were obtained by forcing the Burgers function to peak in velocity at the same radial location that the least squares curve fit of the data peaked, which determines the theoretical turbulent viscosity. From these two methods of reduction, it appears that the profile at the lower flow rate agrees well (within the accuracy of the data) with the Burgers model. However, the model over predicts both the magnitude and the radial station of the peak tangential velocity by a substantial margin. One must recall that the Burgers model applies to single cell vortex structures. Although both velocity profiles are single celled, the global flow field at the higher flow rate exhibited a longer axial length of multi cell structure. Furthermore, the Burgers Model was validated [7] by core injection of vorticity, while the arc heater and water tunnel rely on an inviscid tangential injection at the wall. Therefore, it is unlikely that viscous forces are as dominant. Recall that Reynolds number was not varied independent of other factors such as circulation, local swirl number, etc.

Sullivan and Ogawa

As mentioned previously, no direct comparison between these models and the data is applicable. Instead, The underlying assumptions will be compared (Table 6-2). Although no data was obtained in the theta direction, the flow visualization images confirmed the axi-symmetric nature of the flow field. Due to some probe interference, core pulsations, and the length of the hot film, it is difficult to gain interference free quantitative insight about the nature of the flow field near the core. However, qualitatively, the V_θ component of the data agrees well with both models. The only assumption made by either model that may need modification before applying to a three cell vortex, is the Sullivan assumptions that V_z is independent of r for each cell. From the data, Figures 5-14 and 5-18, it appears that V_z is a strong function of r for both flow rates and both stations. This dependence appears to be more gradual than a boundary layer between two cells. It appears that progress in modeling the three cell vortex is possible using the assumptions similar to those of the Sullivan model.

Table 6-2: Flow field Features

Parameter	**Sullivan Model**	**Ogawa Model**	**Water Tunnel Data**
$\mathbf{V_r}$	f (r) only	[k r] (quasi forced) [k /r] (quasi free)	[Weak f(z)] (both quasi-forced and quasi-free)
$\mathbf{V_\theta}$	f (r) only	[k r(1-kr) (quasi forced) [kr^{-k}] (quasi free)	[Weak f(z)] (both)
$\mathbf{V_z}$	$z \times f(r)$	[k +kz] (quasi forced) k (quasi free)	[Insufficient data for f(z)] [Strong f(r)] (both)

Note: All k's are constants and are independent of each other.

7.0 Conclusions and Recommendations

The experimental program and associated analysis revealed valuable insight into the vortex flow structure in a model with a geometry similar to the AEDC H1 Arc Heater. It was observed that the water tunnel model of the arc heater can support both single cell and multi cell vortex structures for different conditions and at various axial locations. Detailed measurement of the flow structure was performed at two axial stations, D and H for two flow rates. The model flow rate was controlled to generate both multi-cell and single-cell vortex structures in the constrictor region. Reynolds numbers and swirl numbers corresponding to the two flow conditions (based on conditions near the wall at station H) are presented in Table 7-1.

Table 7-1: Flow Field Parameters

Parameter	Low Flow Rate	High Flow Rate
Reynolds Number - based on D_c	5,000	10,000
Swirl Number	3	3

A single component hot film probe was used for these measurements. Detailed data was obtained to characterize the flow fields at the two stations. Such data, unavailable in the past, could be the basis for developing a three cell vortex flow theory. Although there is a substantial amount of theoretical foundation for single cell vortices, almost none exists for a three cell vortex. Therefore, this study not only provided insight into the arc heater type flow field, but valuable data on which to base assumptions for constructing a three cell vortex model. The single cell low flow rate data agreement with the Burgers Vortex Model supports the experimental method (However, the influence of viscous effects in the water tunnel is not as strong as that in Burgers verification experiments). From this baseline, one could observe the effects of the multi cell structure on the velocity field. Two primary conclusions could be drawn:

a) Multi cell structure at any location in this model can substantially influence the velocity profile at other single-cell regions in the same flow field.

b) data obtained on the velocity flow field in a three cell environment are sufficiently similar to the assumptions for the single and two cell vortex theories, that one should have faith that a satisfactory model of the three-cell vortex is possible.

A satisfactory method for extrapolation of results from the water tunnel to the arc heater is not yet available. However, the fact that both single cell and multi-cell structures are expected to occur in the arc heater, and have been shown to occur in the water tunnel, establish the water tunnel as an important simulation tool. This tool is a member of a group of simulation tools needed to obtain the knowledge base required to develop the analytical techniques necessary to predict vortex behavior in the presence of unsteady excitations. Other members of this group include computational models and cold and hot flow air experimental models. These three tools can gain valuable insight into vortex dynamics which will greatly reduce the number and risk of necessary arc heater runs.

The next step in the water tunnel simulation is to conduct non-intrusive measurements, using time accurate techniques such as Particle Image Velocimetry, at several stations in order to ascertain the effect of disturbances on the vortex core. In particular, to find those frequencies which enhance or degrade the vortex structure (i.e. vortex burst). Especially important, is to determine how these frequencies vary with respect to swirl number, arc heater geometry, and vortex pattern (single cell/ multi cell, forced/ forced-free combination).

LIST OF REFERENCES

REFERENCES

[1] Laster, M.L., et al, unpublished technical material.

[2] Felderman, E.J., unpublished technical material and discussions.

[3] MacDermott, W.N., et al., "Flow Contamination and Flow Quality in Arc Heaters Used for Hypersonic Testing, AIAA-92-4028.

[4] MacDermott, W.N., and Felderman, E.J., "Arc Heater Scaling Parameter Predicted with the SWIRLARC Code," AIAA-93-2797.

[5] Rigney, S.J., unpublished technical material.

[6] Ogawa, Akira, Vortex Flow, CRC Press, 1993.

[7] Faler, J.H. and Leibovich, S., "Disrupted States of Vortex Flow and Vortex Breakdown," The Physics of Fluids, Vol. 20, No. 9, 1977.

[8] Chanaud, R.C., "Observations of Oscillatory Motion in Certain Swirling Flow," Journal of Fluid Mechanics (1965), vol 21, part 1.

[9] Khorrami, M. and Grosch, C., "Temporal Stability of Multiple Cell Vortices," AIAA 89-0987

[10] Vakili, A.D., Eramo, R.S., "Influence of Forced Disturbances on the vortex core and the vortex burst," AFOSR Univ POS_210_9MG_056, October, 1989.

[11] Vakili, A.D., et al, "Increasing and Decreasing the Stability of a Confined Vortex by Forcing," AIAA 93-3039.

[12] Fox, R.W., McDonald, A.T., Introduction to Fluid Mechanics, John Wiley & Sons, 1992.

[13] White, F.M., Viscous Fluid Flow, McGraw-Hill, Inc., 1991

[14] Goldstein, R.J., Fluid Mechanics Measurements, Hemisphere Publishing Corporation, 1983.

APPENDIXES

APPENDIX A

FACILITY SHAKEDOWN, HOT FILM ANEMOMETER

In order to ensure that quality data was obtainable, a conscientious shakedown program was followed. The two main thrusts were to ensure that the water tunnel circuit was not introducing significant disturbances to the arc heater model, and calibrate the hot film anemometer system for taking time averaged flow field measurements. The first effort was described in Chapter 5. The second is described Below.

Hot Film Anemometer

Extensive problems were encountered calibrating the hot film anemometer system. The first indication of problems was the inability to obtain reasonable velocity calibrations. The errors primarily consisted of two types: hysteresis error, and repeatability error (or precision error).

An example of the hysteresis error is shown in figure A-1. There are two features of this error that are particularly noteworthy. First, that it only occurs at a certain range of velocity. Second, it appeared during the same calibration run. The phenomenon was most likely to appear when one waited for the flow fluctuations in the calibration device to dissipate between velocity runs. If one proceeded to the next velocity point immediately after the previous one without waiting for the disturbances to settle, the phenomenon appeared less severe. It was supposed that the phenomenon was related to the interaction between the high frequency probe vibration and the damping effect of vortices left in the flow from the previous velocity point. This was not an entirely acceptable explanation, since high frequency turbulence dissipates very quickly. Never the less, the problem was eventually solved by a combination of three fixes:

a) Improving the bearing mechanism of the calibration device to reduce probe vibration.

b) Installing a larger drum on the axis of the electric motor of the calibration device. This increased the tension on the cable, reducing the potential for slip between the cable and the drum.

c) Reducing the distance between the time measuring gates. The reduced distance between the gates tended to minimize any acceleration or deceleration during calibration. The distance was still large enough to cover many cycles of the high frequency probe vibration.

The second type of error, repeatability error, is the measure of the difference between two calibrations sets (Figure A-2). Accuracy of the probe measurements is determined by calibrating the probe output voltage vs velocity both before and after a tunnel data run. The source of this problem was especially difficult to diagnose. Multiple calibration runs repeated in succession yielded good agreement (Figure A-3). However, calibrations obtained before and after a data run yielded poor agreement (Figure A-2). The data acquisition system was cleared as a possible source by inputting a known constant voltage into the system and receiving the same constant voltage out. Insight into the source of the error came from comparing the probe output voltage to the tunnel flow rate data over a long period of time with the probe maintained at a single location and orientation inside the water tunnel (Figures A-4 and A-5). Notice the gradual degradation in anemometer output, while the tunnel flow rate (as measured by the pressure transducer) remained relatively constant. Contamination of the probe was suspected. Since cleaning of the hot film with isopropyl alcohol restored the anemometer output (Figure A-6), accumulation of contaminating particles was suspected, rather than a chemical reaction.

In order to ascertain the nature of the contamination, samples of the water tunnel water were sent to the AEDC Chemical Laboratory for analysis (Reference x). Based on the results of the AEDC laboratory, three actions were taken:

a) The water in the tunnel was drained and replaced with water from another source which did not contain the large organic fibrous material.

b) A filter was installed (see Chapter 4) which would remove particles down to the five micron level. Since the circuit contained some non-stainless steel components which contributed rust particles to the system, the filter was run for at least twenty-four hours between runs.

c) The water tunnel model and circuit were thoroughly cleaned to reduce the likelihood of contaminants being added to the flow field during a data run.

As a result of the above actions, the level of contamination dropped dramatically (Table A-1). More importantly, anemometer output remained stable over the typical two hour period of a data run. Figure A-7 shows the typical excellent agreement between velocity calibrations obtained before and after one of the final data runs.

Table A-1: Water Tunnel Particle Contamination

Paticle Size in Microns						
Sample	**5-15**	**15-25**	**25-50**	**50-100**	**>100**	**fibers >100**
Contaminated (concentration/ ml)	113	12	0.35	0.17	0.15	0.08
Filtered	0.95	0.77	0.09	0.05	0.05	0.03

APPENDIX B

INSTRUMENTATION CALIBRATION

Hot Film Anemometer Calibration

General Description

A constant temperature hot wire anemometer indicates local fluid velocity by measuring the circuit output voltage required to maintain a constant resistance across the immersed probe wire [14]. The resistance of the wire is directly proportional to its temperature. Therefore, the anemometer is measuring the voltage required to maintain a constant temperature across the wire. This temperature is usually slightly greater than that of the mean fluid. Since there is a temperature difference between the probe wire and the fluid, heat is transferred from the wire to the fluid. For low speed flow, the heat transferred is proportional only to the temperature difference (held fixed) and the fluid velocity. In order to maintain the temperature (and resistance) of the wire for increasing flow rates (heat transfer rates), greater power must be supplied to the wire. Therefore, a greater current must be applied across the probe wire. The variation in this current across a reference resistor gives a voltage for calibration of the system. One can calibrate fluid velocity versus output voltage.

Theory

<u>Velocity Calibration:</u> The first step in calibrating a constant temperature hot film is to calibrate output voltage versus fluid velocity for flow perpendicular to the probe wire as shown in figure A-7. This is relatively straight forward since one can assume all of the increase in heat transfer is due to the velocity of the probe relative to the fluid, and that the

probe wire resistance is linearly dependent on temperature. Convective heat transfer from a wire to the surrounding medium has been defined [14] as:

$$\dot{Q} = I_s^2 R_s = Nu \cdot \pi \cdot (2l) \cdot k_f \cdot (T_s - T_a) \tag{B.1}$$

Where Nusselt Number has been found to vary empirically with respect to velocity

$$Nu = A' + B' \overline{U}_{eff}^{n} \tag{B.2}$$

Where A' and B' depend on flow Prantl number and kinematic viscosity, neither of which change appreciably during the test. This relationship is valid for $0.71 \leq \Pr \leq 525$, and $2.0 \leq Nu \leq 20.0$. For this study these values were approximately Pr = 6.9, and Nu >= 2 (Velocity greater than 1.1 in/sec). One can also assume that the probe film resistance is directly proportional to temperature:

$$R = R_r[1 + \alpha_r (T - T_r)] \tag{B.3}$$

If one substitutes R_s and R_a in for R in equation 3, one can easily obtain:

$$(R_s - R_a) = \alpha_r R_r (T_s - T_a) \tag{B.4}$$

The output voltage (by Ohms Law) of the anemometer is:

$$\overline{E} = [R_s + R_{cab} + R_{in}] I_s \tag{B.5}$$

Equations B.1, B.2, B.4 and B.5 can be combined to form:

$$\overline{E}^2 = \frac{2\pi l k_f (R_s - R_a)(R_s + R_{cab} + R_{in})^2}{\alpha_r R_r R_s} [A' + B' \overline{U}_{eff}{}^{n}] \tag{B.6}$$

Therefore, one can empirically define parameters A and B for Kings Law:

$$\overline{E}^2 = A + B \overline{U}_{eff}^{n} \tag{B.7}$$

Where:

$$A = \frac{2\pi l k_f (R_s - R_a)(R_s + R_{cab} + R_{in})^2}{\alpha_r R_r R_s} A' \tag{B.8}$$

$$B = \frac{2\pi l k_f (R_s - R_a)(R_s + R_{cab} + R_{in})^2}{\alpha_r R_r R_s} B' \tag{B.9}$$

Since resistance is dependent on temperature, it is necessary to define a temperature correction. There are two types of temperature corrections necessary: Intra-data set corrections, and set to set corrections

The first, intra-data set, corrects for heating during a run. In this situation, the operating resistance and temperature of the hot film probe remain constant while the ambient temperature of the fluid changes. Therefore, the overheat ratio changes during the test. One can define a King's Law for both the temperature corrected and uncorrected case:

$$\overline{E}_c^{\,2} = A_c + B_c\overline{V}_c^{\,n} \tag{B.10}$$

$$\overline{E}_a^{\,2} = A_a + B_a\overline{V}_a^{\,n} \tag{B.11}$$

If one substitutes in equations eight and nine, assumes constant fluid properties, and recognizing that U is the same for both ten and eleven:

$$\frac{A_c}{A_a} = \frac{B_c}{B_a} = \frac{\dfrac{(R_s - R_c)}{R_{sc}}(R_s + [R_{cab} + R_{in}])^2}{\dfrac{(R_s - R_a)}{R_s}(R_s + [R_{cab} + R_{in}])^2} \tag{B.12}$$

Which reduces to:

$$\frac{A_c}{A_a} = \frac{B_c}{B_a} = \frac{R_s - R_c}{R_s - R_a} = \frac{T_s - T_c}{T_s - T_a} \tag{B.13}$$

If one combines equations B.10, B.11, and B.13, the temperature correction becomes:

$$E_c = \left(\frac{T_s - T_c}{T_s - T_a}\right)^{\frac{1}{2}} E_a \tag{B.14}$$

Although this is the most elegant way to define the correction, it is not the most useful in practice since the sensor temperature is not known. Instead, one sets an overheat ratio,

$$\alpha_{OH} = \frac{R_s}{R_c} \tag{B.15}$$

If one substitutes in equations B.4 and B.15 into B.14, and performs routine algebraic manipulations, one obtains:

$$\frac{E_c}{E_a} = \left\{\frac{1}{1 + \dfrac{(T_c - T_a)}{\dfrac{[\alpha_{OH} - 1]}{[\alpha_r R_r]} R_c}}\right\}^{\frac{1}{2}} \tag{B.16}$$

At first equation B.16 may appear awkward. However, it is expressed in terms that are specified by the probe manufacturer, specified by the user, or obtained during the test. The system used in this study had the following characteristics:

a) $[\alpha_{OH} - 1] = 0.05$, a user controlled input of the anemometer system . This was the value used throughout the study.

b) $[\alpha_r R_r] = [\frac{R_{100°C} - R_{0°C}}{100}] = 0.0147$, as specified by the hot film probe manufacturer.

c) R_C, the initial cold resistance as measured by the anemometer system.

d) T_C, T_a, as measured by the thermometer.

NOTE: T_C is the initial water ambient temperature of the run, while T_a is the ambient temperature at each subsequent data point in the run.

The second temperature correction, data set to data set, allows accurate comparison of two data sets taken at the same overheat ratio, but at different starting temperatures, T_C. This type of correction is often used to apply calibration data taken at one temperature to tunnel data taken at another. Before this correction can be applied, each data set must be "intra data set" temperature corrected as outlined above. The analysis below assumes that data set two is being temperature corrected to compare with data set one.

Substituting the corrected operating conditions of each set into equation B.6 and dividing yields:

$$\left(\frac{E_{2corr}}{E_2}\right)^2 = \frac{\frac{(R_{s1} - R_{c1})}{R_{s1}}(R_{s1} + [R_{cab} + R_{in}])^2}{\frac{(R_{s2} - R_{c2})}{R_{s2}}(R_{s2} + [R_{cab} + R_{in}])^2} \tag{B.17}$$

Since $R_{s1}, R_{s2} >> [R_{cab,} + R_{in}]$, and overheat ratio $\alpha_{OH} = \frac{R_{s1}}{R_{c1}} = \frac{R_{s2}}{R_{c2}}$,one can rewrite equation B.17 as:

$$(\frac{E_{2corr}}{E_2})^2 = \frac{(1+2\frac{[R_{cab}+R_{in}]}{R_{s1}})R_{s1}{}^2}{(1+2\frac{[R_{cab}+R_{in}]}{R_{s2}})R_{s2}{}^2} \tag{B.18}$$

If one assumes that $(1+2\frac{(R_{cab}+R_{in})}{R_{s1}}) \cong (1+2\frac{(R_{cab}+R_{in})}{R_{s2}})$, then equation B.18 becomes:

$$(\frac{E_{2corr}}{E_2})^2 = (\frac{R_{s1}^2}{R_{s2}^2}) = (\frac{R_{c1}}{R_{c2}})^2 = [1+\frac{\alpha_r R_r}{R_{c2}}(T_{c1}-T_{c2})]^2 \tag{B.19}$$

or finally

$$\frac{E_{2corr}}{E_2} = 1+\frac{\alpha_r R_r}{R_{c2}}(T_{c1}-T_{c2}) \tag{B.20}$$

The probe used in this study had the following characteristics:

$R_{in} = 0.20$

$R_{cab} = 0.315$

$\alpha_r R_r = 0.0147$

$R_c =\sim 5.7$ Ohms in the temperature range used

For the probe used in this study, a temperature difference of about four degrees centigrade would be required to cause a one percent correction to the output voltage value. The corresponding error in velocity would be:

$$\frac{\partial U}{U} = \frac{E}{U}(.01)\frac{\partial U}{\partial E} = \{\frac{(.02)E^2}{nBU}\}(\frac{E^2-A}{B})^{(\frac{1}{n}-1)} \tag{B.21}$$

For a typical calibration, Figure A-7, (A=1.890, B= 2.301, n=.418) a point at 10 in/sec, 2.8 Volts would experience an error of 6.1 %. Or approximately 1.5 % per degree. However, a four degree temperature correction in the intra-data run correction would cause an over four percent correction in output voltage, resulting in a 9 % correction in velocity, or about 2.3 % per degree.

Clearly, it is very important to accurately correct for temperature effects, especially if the ambient fluid temperature changes during a run.

Yaw Angle Calibration: The second step is to calibrate over different yaw angles. This is a little more complicated since the heat transfer is proportional to both the velocity perpendicular and parallel to the probe wire. One can not assume that the probe is measuring the component of velocity perpendicular to the wire. The 'velocity' one obtains by correlating the output voltage to the King's Law velocity calibration in step one is called the effective velocity, V_{eff}. In order to obtain the actual velocity U, one must apply a yaw angle correction. At this point it is necessary to define an angle convention (Figure B-1):

theta (θ)= angle from the probe axis to the laboratory axis (counter-clockwise

phi (ϕ)= angle from the flow axis to the laboratory axis (counter-clockwise

psi = (phi-theta)= (ψ)= angle from the flow axis to the probe axis (counter-

Note: the probe is not necessarily front to back symmetric. Therefore, there is a slight, but important difference between (phi-theta) =0 and (phi-theta) =180 degrees. However, the probe is left-right symmetric. Therefore, (phi-theta)= -(phi-theta).

If one assumes a left-right symmetry, one can define an even function over the range -90 deg < (ψ) < 90 deg which will fit yaw data over this range. This equation takes the form:

$$\frac{U_{eff}}{U} = a_0 + a_1 \cos(\frac{\psi}{2}) + a_2 \cos(\psi) + a_3 \cos(2\psi) + a_4 \cos(4\psi) \qquad \text{(B.22)}$$

or

$$U = \frac{U_{eff}}{a_0 + a_1 \cos(\frac{\psi}{2}) + a_2 \cos(\psi) + a_3 \cos(2\psi) + a_4 \cos(4\psi)} \qquad \text{(B.23)}$$

The shape of the curve defined by equation 16 depends weakly on velocity. Figure B-2 shows two curves. One taken at 5 in/sec and one taken at 10 in/sec. This represents the velocity range of the data for the upper flow rate. If one constructed a single curve to fit both data sets, the maximum angle error introduced would be four degrees. For a complete error analysis, see the Appendix E.

Procedure

Both velocity calibrations and angle calibrations were performed in the UTSI hot film calibration device (See Chapter 4). In order to minimize the difference in temperature between the calibration and the data, water from the water tunnel tank was used for the calibration.

Velocity Calibration: Velocity calibration was performed in ascending velocity from zero up to approximately twenty inches per second and then from twenty down to zero inches per second. This was done to ensure that there was no measurement hysteresis.

Yaw Angle Calibration: Yaw angle calibrations were performed at multiple constant velocity settings between two and a half and ten inches per second. Since the flow axis and the calibration axis were coincident, $\phi = 0$. Therefore, $\theta = \psi$ for the calibration. For each velocity, theta ranged from -100 deg to +100 deg. The wide angle range was used to ensure that the complete probe face was calibrated even in the event of a slight error in angle setting.

Curve Fitting

Velocity Calibration: All four velocity calibrations (before data gathering: up and down in velocity, and after data gathering: up and down in velocity) were used to define a single King's Law calibration curve (Figure A-7). The King's Law coefficients A, B, n were chosen using a least squares curve fit procedure.

Yaw Angle Calibration: Yaw angle calibration reduction is accomplished for each velocity in the following steps:

a) The voltage output data are converted using the King's Law coefficients obtained in the velocity calibration above.

$$U_{eff} = \left[\frac{E^2 - A}{B} \right]^{\frac{1}{n}} \tag{B.24}$$

b) The Ueff is divided by U, the true velocity, obtained from the calibration devise.

c) The ratio Ueff/U is normalized by multiplying the it by U/Ueff at zero degrees. This, of course, automatically gives a value of one at zero degrees. This normalization is applied to prevent random error from unduly influencing the curve fit. Furthermore, by definition, Ueff/U=1 at $\psi = 0$.

d) If necessary, the whole curve is shifted by some angle if it appears an angle bias is present due to incorrect initial setting of the probe angle.

e) Finally, a cosine function defined in equation 19 is fitted using the least squares technique.

Hot film Calibration Results

Velocity Calibration: Two velocity calibrations were obtained for each run, one before the run, and one after. A representative velocity calibration is shown in Figure A-7. Notice the close agreement between the velocity calibration data and the King's Law profile.

Yaw Angle Calibration: Two sets of angle calibration data were obtained. The hot film probe insulation was damaged during an unreported run, necessitating a probe film replacement. In order to save time, a backup probe was used. Since small changes in probe geometry can influence hot-wire sensitivity to cross flow, it was necessary to perform yaw angle calibrations for each probe. As one can observe from Figure B-2, angle calibration is sensitive to mean fluid velocity. Therefore, yaw angle calibration data was obtained at several mean velocities. In reducing the primary data, angle calibrations were used which best represented the velocities encountered in the flow. If the flow field experienced wide measurements of velocity, angle calibrations from two bounding velocities were averaged (Figure B-2). If the probe is assumed to be left-right symmetric (response at ψ is the same as the response at $-\psi$), then one can obtain an idea of the accuracy of angle measurement through data reduction (Appendix C). Table B-1 displays the angle error for six yaw angle calibration runs, with Figure B-3 showing an offset calibration example. Since it is far easier to obtain a line of sight indication of angle in the actual water tunnel than in the calibration device, one should consider the errors to be upper bounds of the random error associated with aligning the probe axis with the tunnel axis.

Table B-1: Yaw Calibration Angle Error

Yaw Calibration #	Error (deg)
1	2.90
2	2.80
3	0.90
4	0.03
5	0.15
6 (Figure B-3)	3.22
Average	~ 1.7

Yaw calibrations four and five (Table B-1) indicate almost serendipitous accuracy (Blind luck!). Those two calibrations were taken sequentially without removing the probe from the calibration device between calibration runs. A conservative estimate of angle offset error, based on the limited population, would be about three degrees.

APPENDIX C

HOT FILM DATA

ACQUISITION AND REDUCTION PROCEDURE

Objective

The objective of acquiring hot film data is to define a time averaged velocity field (V_r,V_θ,V_z as functions of radius) at a given axial station. The Procedure and Reduction paragraphs below outline the methodology used in this study to obtain the above mentioned flow field data at one particular station. One should be aware that this reduction procedure obtains a three dimensional velocity field, despite the fact that calibration data was obtained in only two dimensions. The assumption is made that the probe's sensitivity to pitch inclination is independent of pitch angle. Therefore, the probe is sensitive only to flow perpendicular and parallel to the film.

Procedure

The data acquisition procedure consisted of the following steps:

Preparation of facility and instrumentation

After several months of working with the hot film anemometer system, several operational procedures were discovered which greatly aided data accuracy. The list below is by no means exhaustive, but does serve to document some lessons learned that might not be easily obtained from the literature.

Purify the water: As described in Appendix A, slight contamination of the fluid, especially by rust particles, can degrade anemometer output by over 200mV/hr. Since the

UTSI water tunnel does have non stainless steel sections, contamination would build during a test. Therefore, it was necessary to run the filter (described in Chapter 4) overnight before each run.

Equilize the temperature throughout the water tunnel curcuit: The water tunnel circuit contained walls of stainless steel, PVC pipe, and optically clear Plexiglas. Each has distinct insulation properties, possibly yielding a thermal gradient inside the circuit. [Note: the circuit has enough heat capacity that it is generally not in equilibrium with the surrounding environment] As demonstrated in Appendix B, temperature differences of only a few degrees can have substantial impact on the data. For the UTSI system, thirty minutes of running was adequate.

Stabilize the temperature of the electronics: Many electronic components possess properties which vary with temperature. Allowing them to "warm up" before data gathering reduces the likelihood of the data acquisition electronics from degrading the accuracy.

Hot Film Velocity Calibration

Two velocity calibration runs were performed, one before and one after each tunnel data series. The purpose was to ensure that the velocity calibration was valid for the entire run. This was especially important considering the velocity drift we occasionally encountered due to contamination. Each velocity calibration data point obtained the following data:

a) Hot wire output voltage

b) Velocity

c) Temperature

Typically, each calibration consisted of ten data points starting at 0 in/sec and ascending in velocity by increments of about 2 in/sec to a peak of 20 in/sec, and ten data points descending in velocity from 20 to 2 in/sec (Figure A-7). Data from both would calibrations would be used to determine the king's law coefficients.

Tunnel Data

Each tunnel data run consisted of data points taken at incidence angles θ ranging from -10 to 190 degrees in increments of ten degrees, at radii ranging from 0 (centerline) to 1.9 inches. At every point the following information was obtained:

a) Tunnel flow rate (as measured by the pressure transducer)

b) Hot wire Voltage output

c) Tunnel Temperature

d) Radius

e) Angle (theta)

The radius and angle parameters were manually entered into the Data Acquisition System (DAS). The flow rate, hot wire voltage, and tunnel temperature were measured quantities digitized by the DAS, with no manual intervention.

Facility shakedown and preliminary flow visualization data indicated that the dominant fluctuations occurred at 0.7 Hz or slightly greater (Figure 5-9). Therefore, a time greater than four wavelengths (approx. six seconds) was chosen for obtaining the hot-wire voltage data for each data point. The voltage data would consist of 4096 samples evenly distributed throughout the 6 seconds. At all angle and radius stations, the 4096 points were averaged. However, at theta = 90 degrees, for all radii, an additional point was obtained which sent all 4096 voltage values to a file. The reason for obtaining this time accurate data was to obtain average fluctuation frequency and amplitude information, not time accurate Velocities.

Data Reduction

Averaged data

In summary, the process is to assume a V_r, U, and ϕ and generate a Veff which matches the Veff obtained from the data. The process is described in detail below:

Temperature correction Voltage data from both the velocity calibration and the tunnel data must be corrected to the same value. Appendix B describes in detail how this is done.

Voltage to effective Velocity correlation: A King's law curve (as described in Appendix B) is best fitted to a data set consisting of both velocity calibration runs, yielding an analytical expression between hot wire output voltage and effective velocity (Veff). All of the tunnel hot-wire voltage data is then converted into effective velocities.

Iteration loop: The process now is to iterate to find the unique combination of V_r, U, and ϕ that will yield the profile obtained in step b. The iteration is performed on the set of data from each radius. Figure C-1 illustrates the geometry of the terms used in the iteration. The steps in each iteration cycle are outlined below:

Step 1 Assume U, Vr and ϕ.

Step 2 Calculate the total velocity perpendicular to the probe for each angle theta:

$$U'_{perp} = \{[U_{assumed}\cos(\phi-\theta)]^2 + [V_r]^2\}^{\frac{1}{2}} \qquad \text{(C.1)}$$

Step 3 Calculate the total velocity parallel to the probe for each angle θ

$$U'_{Parallel} = U\sin(\phi-\theta) \qquad \text{(C.2)}$$

Notice there is no V_r component since V_r is always perpendicular to the probe wire.

Step 4 Compute the total velocity impinging the probe:

$$U' = \{U'^2_{Perp} + U'^2_{Parallel}\}^{\frac{1}{2}} \qquad \text{(C.3)}$$

Step 5 Compute the effective angle of the flow relative to the probe at each angle θ:

$$(\phi-\theta)' = \tan^{-1}\left(\frac{U'_{parallel}}{U'_{perp}}\right) \tag{C.4}$$

Notice that

$$(\phi-\theta)' \neq (\phi-\theta) \tag{C.5}$$

Step 6 Compute the effective velocity at each angle θ:

$$V'_{eff} = U' \cdot \cos fn[(\phi-\theta)'] \tag{C.6}$$

where,

$$\cos fn[z] = a_0 + a_1 \cos(\frac{z}{2}) + a_2 \cos(z) + a_3 \cos(2z) + a_4 \cos(4z) \tag{C.7}$$

The coefficients are defined by the yaw angle calibration (Appendix B), which is performed once per probe.

Step 7 Compute the error: At each angle θ, the difference between the Veff predicted in step 6 and the value Veff obtained by reducing the data is squared. The squares of the differences at each angle theta are added together to obtain one value.

Step 8 Repeat steps 1 through 7, minimizing the sum of the differences squared. Once a converged value of Veff is reached, then the components U_Z and U_θ are easily obtained:

$$U_z = U\cos(\phi),\ U_\theta = U\sin(\phi) \tag{C.8}$$

Note that all of these values are averaged. Therefore they will contain a steady state component plus the average of the absolute amplitude of the fluctuations. This non-steady component is especially significant in the Vr direction. Figures C-2 through C-6 show the typical agreements between the data and the predicted profile based on the converged values of Vr, V_θ, and Vz. The level of deviation (least squares) is shown in Figure C-7.

APPENDIX D

AXIAL MASS FLOW CALCULATIONS

In order to obtain the axial mass flow through a given station of the water tunnel model, one needs two pieces of information:

1. The axial velocity V_z
2. Radius station where the velocity was obtained

The more radial stations where axial velocity was obtained, the more accurate the flow rate. The actual formula for obtaining the flow rate is straight-forward:

$$\dot{m}_z = \rho\pi\sum_{i=1}^{n}\{(r_{i+1}^2 - r_i^2)\cdot(\frac{V_{z_{i+1}} + V_{z_i}}{2})\} \tag{D.1}$$

This assumes that the increments are equal, r_0 is the centerline, and that r_n is one increment from the wall.

APPENDIX E

ERROR ANALYSIS

The error analysis presented in this chapter is in large part a summary of analysis presented throughout this thesis. The parameters analyzed follow the order outlined in Table 4-1.

Velocity

As stated in Chapter 4, the error in velocity appears to be typically about +/- 5% based on the velocity calibrations. However, for some runs, the error in velocity was up to 10 %. The velocity drift due to contamination was the dominant factor. The error due to average temperature variation was probably within 1%. The thermometer used had a temperature repeatability within 0.1 degree, enabling a very accurate temperature correction (Appendix B). A spatial variation in temperature of one degree would have caused an error of up to 2.25 % (Appendix B).

Angle

As thoroughly described in Appendix B, the error in probe angle setting is within 3 degrees for the calibration devise, but probably less for the water tunnel due to the improved line of sight.

Radial Spatial Resolution

With the aid of a micrometer, the depth of the probe was able to be precisely positioned. However, flex in the probe holder prevents accuracy from surpassing +/- 0.05 inches.

Amplitude

Although not specifically determined, the dominant source of error is the hot-wire probe used to obtain the front end data. Therefore, an absolute error of at least 10% is reasonable.

Frequency

The frequency resolution is determined by the number of samples and the length of the period sampled. For this study

n (number of Samples) = 4096

Δt (Sampling Interval) = 6 sec/ 4096 samples = 0.0015 sec

f_s (Sampling Frequency) = $1/\Delta t$ =667

Δf (Frequency Resolution) = f_s/n = **0.16**

Flowrate

Although the instrument is capable of measuring flow rate accurately to within 1%, the fluid noise at the orifice causes flow rate fluctuations of up to 0.3 gal/min (even after averaging over 6 sec) causing an error of about six percent for the lower flow rate. The long period of the oscillations could indicate some large scale facility interactions. However, the amplitude of these fluctuations was less at the water tunnel model (Chapter 5).

APPENDIX F

FIGURES

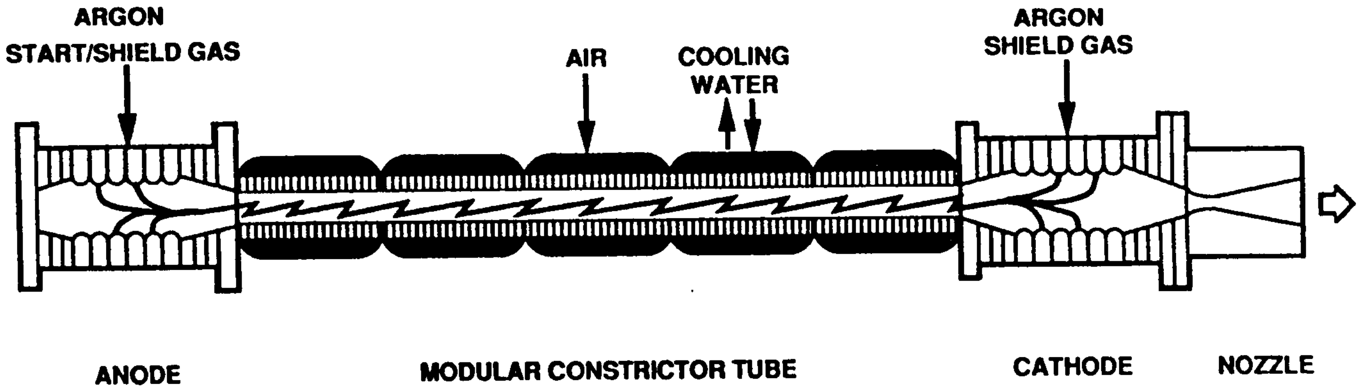

FEATURES

• HIGH ENTHALPY	TO 20,000 BTU/LB (AT 1 ATM.)
• HIGH PRESSURE	TO 120 ATM. (AT 4,000 BTU/LB)
• RELATIVELY CLEAN FLOW	10 - 100 PPM
• FIXED LENGTH ARC	REPEATABLE PERFORMANCE
• COMPLEX HARDWARE	DIFFICULT MAINTENANCE

Figure 1-1: Arc Heater Configuration

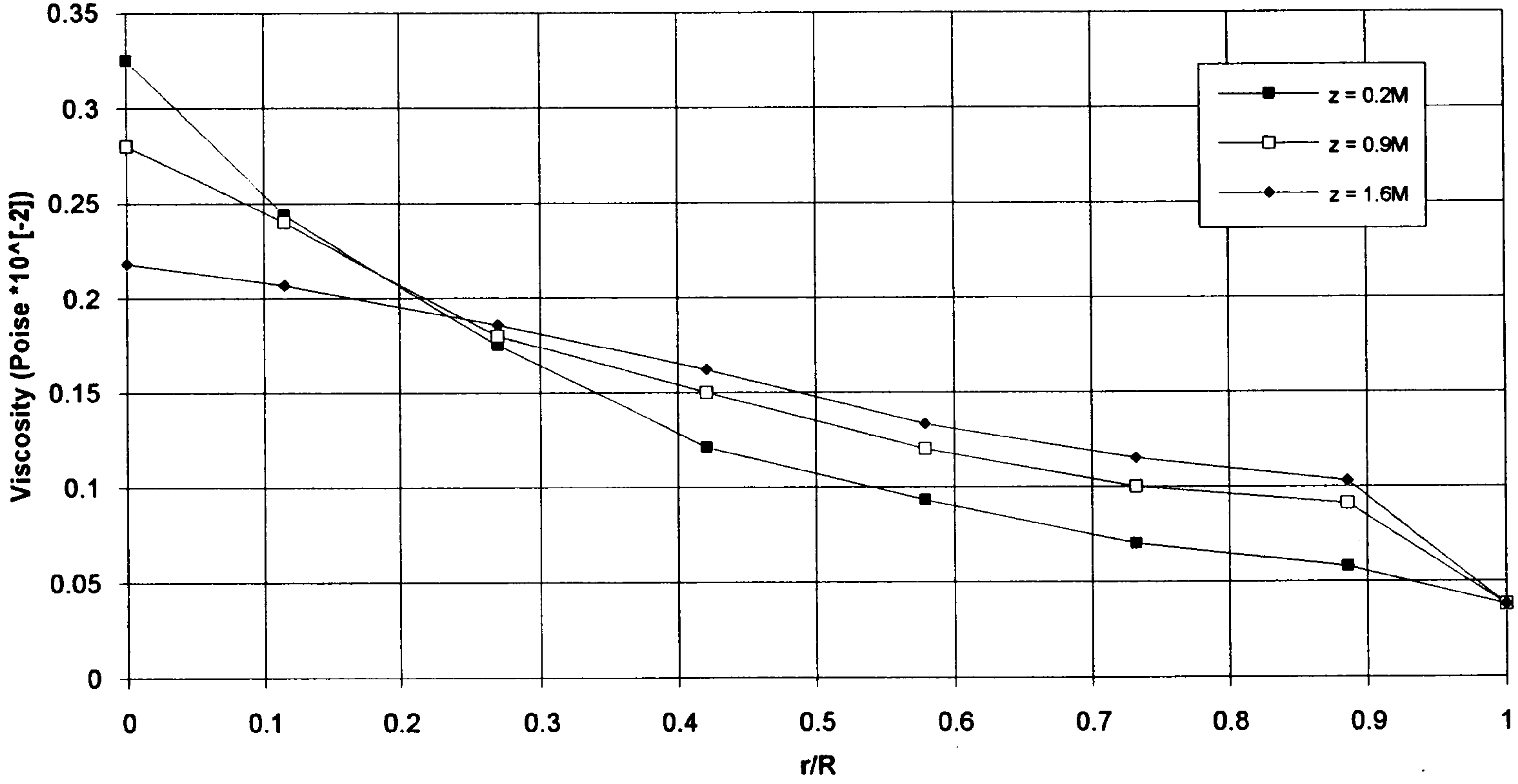

Figure 2-1: Coefficient of Viscosity vs. Radius

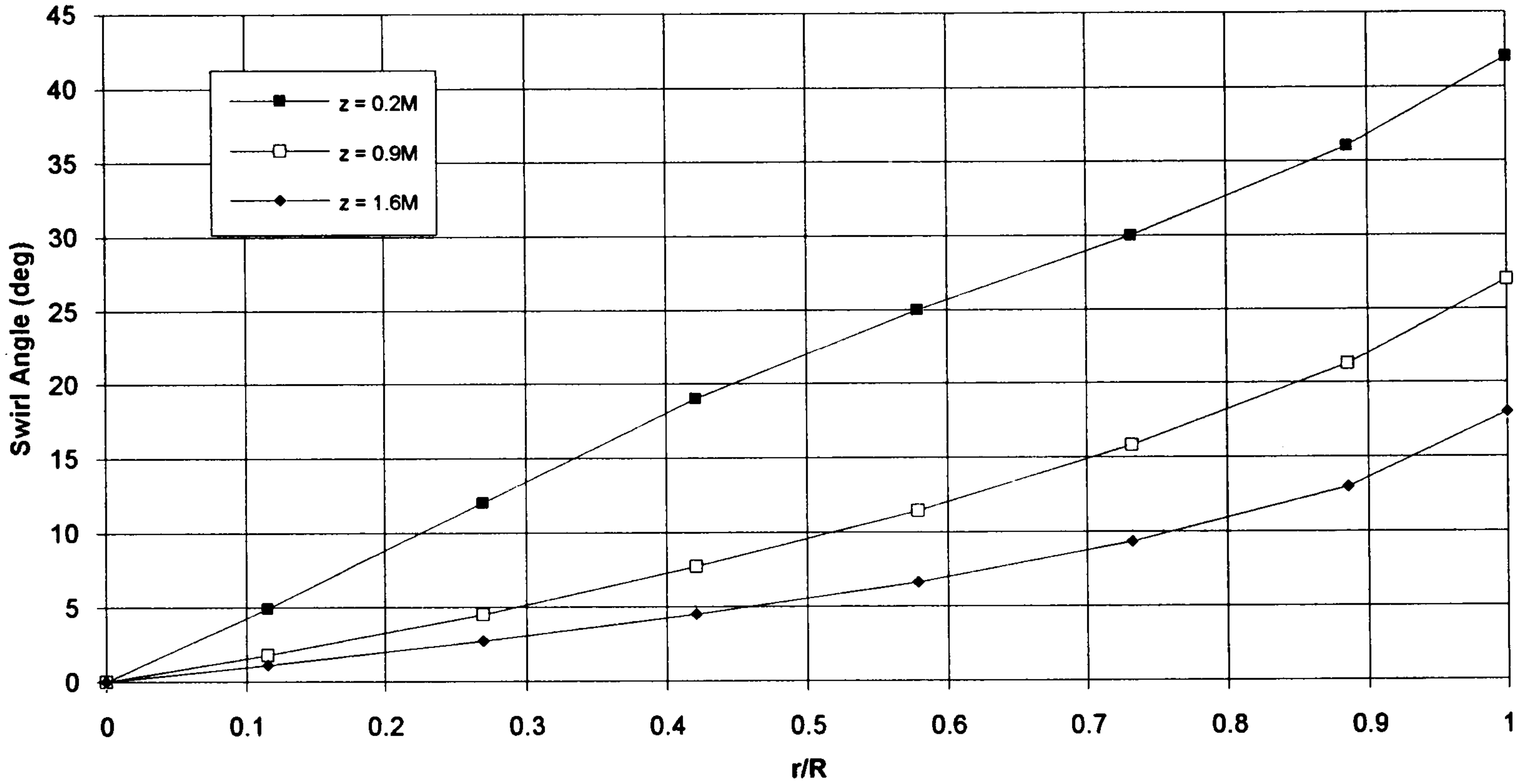

Figure 2-2: Swirl Angle vs. Radius

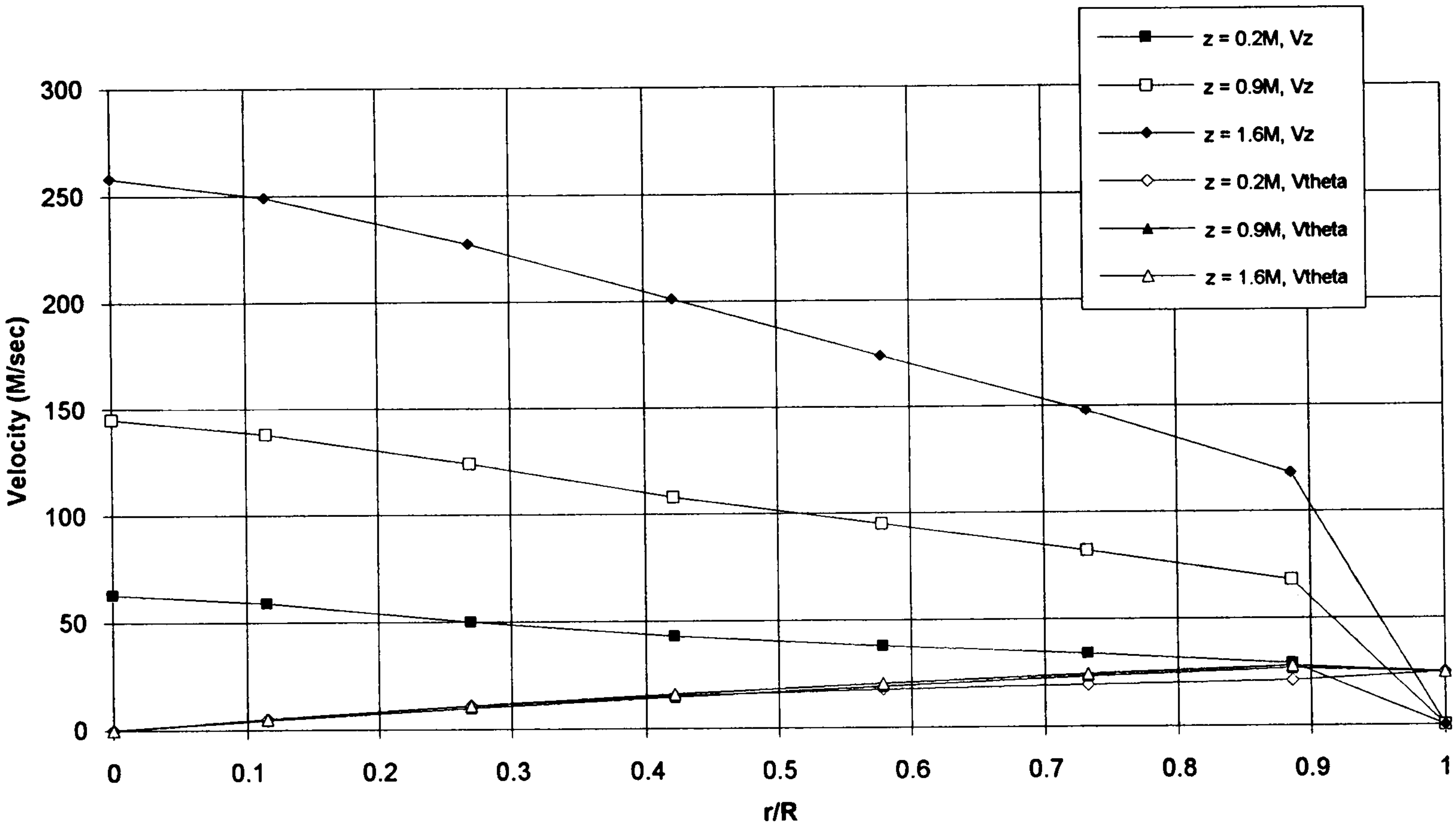

Figure 2-3: Local Velocity vs. Radius

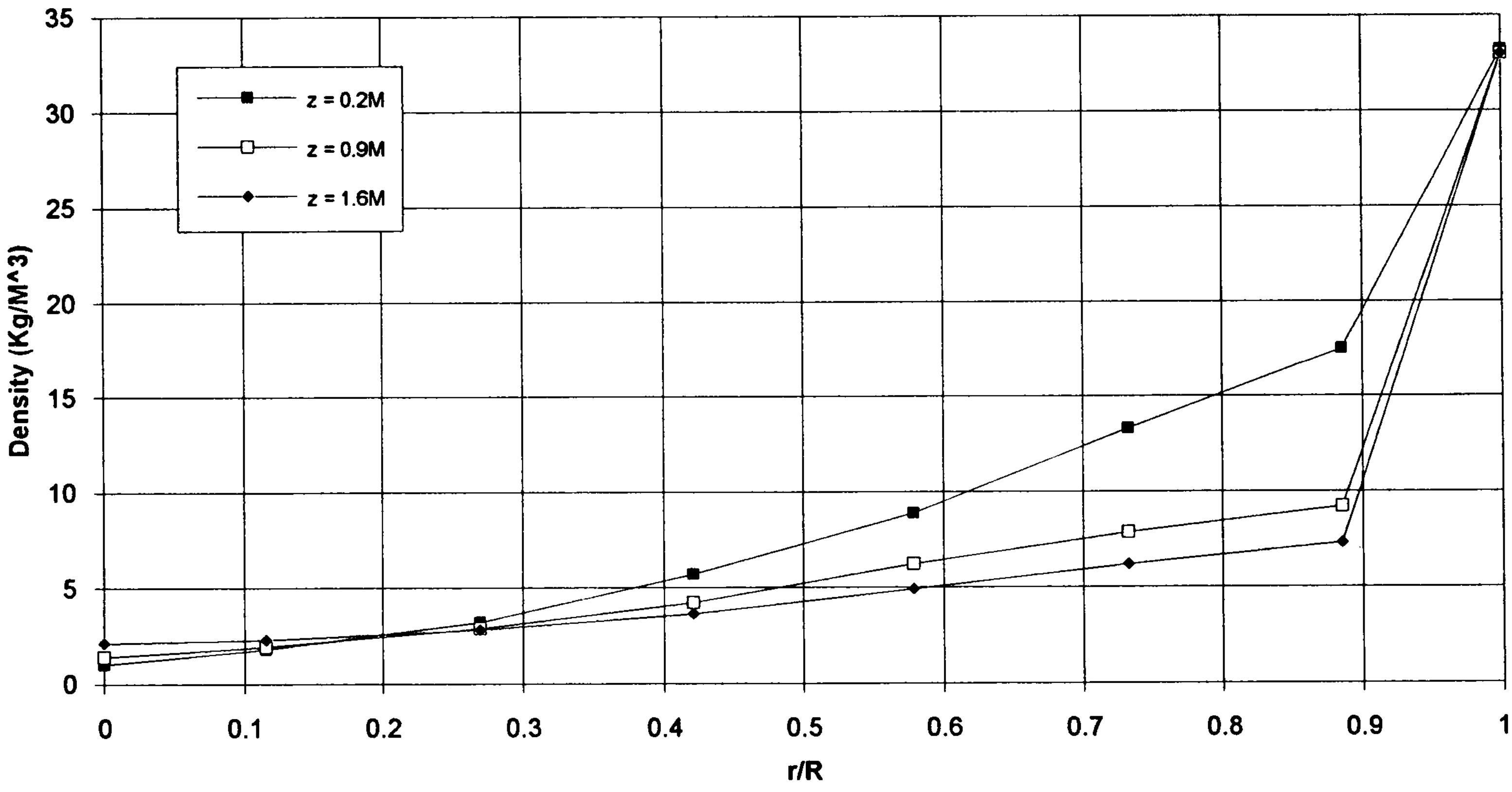

Figure 2-4: Density vs Radius

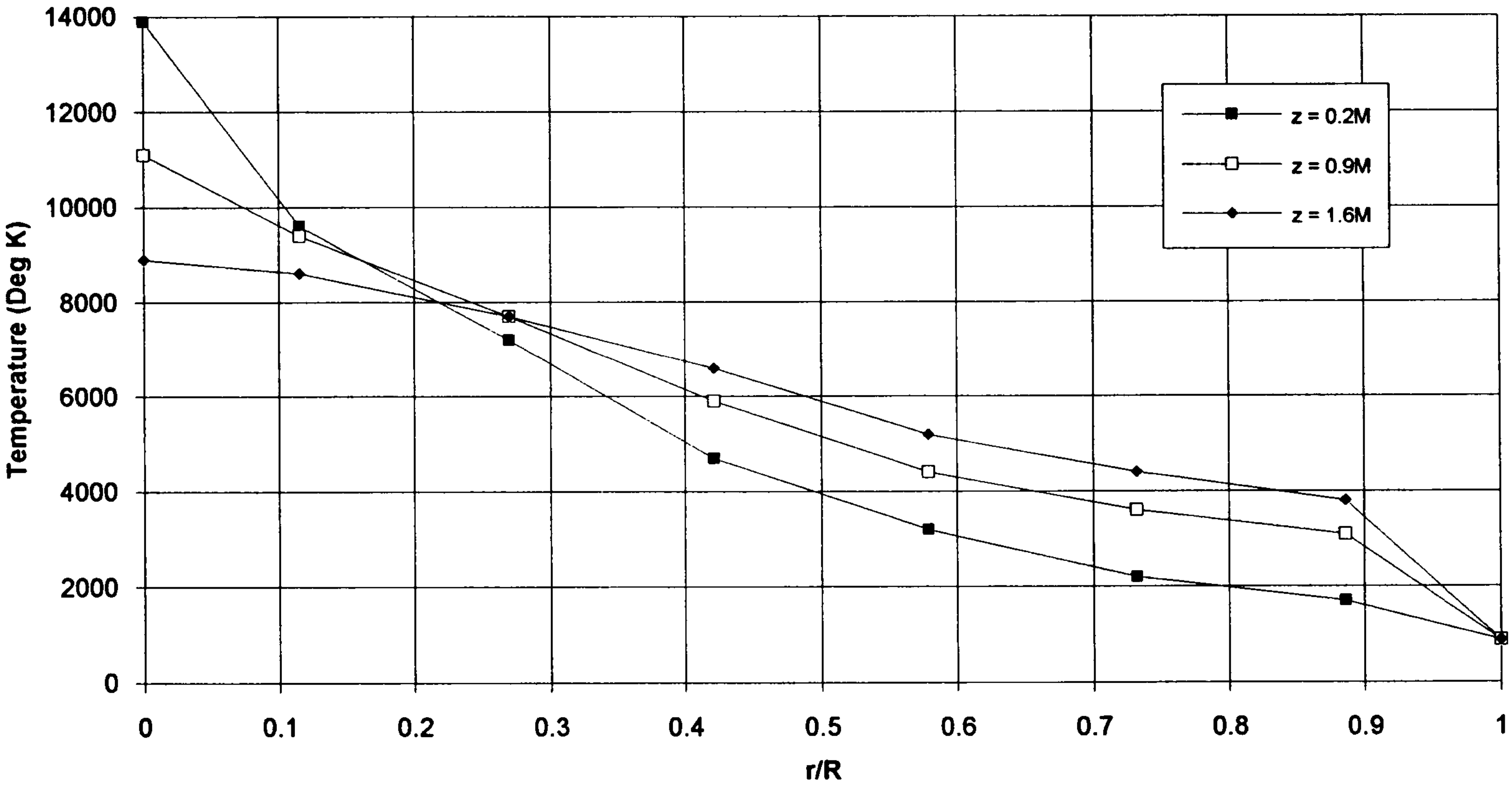

Figure 2-5: Gas Temperature vs Radius.

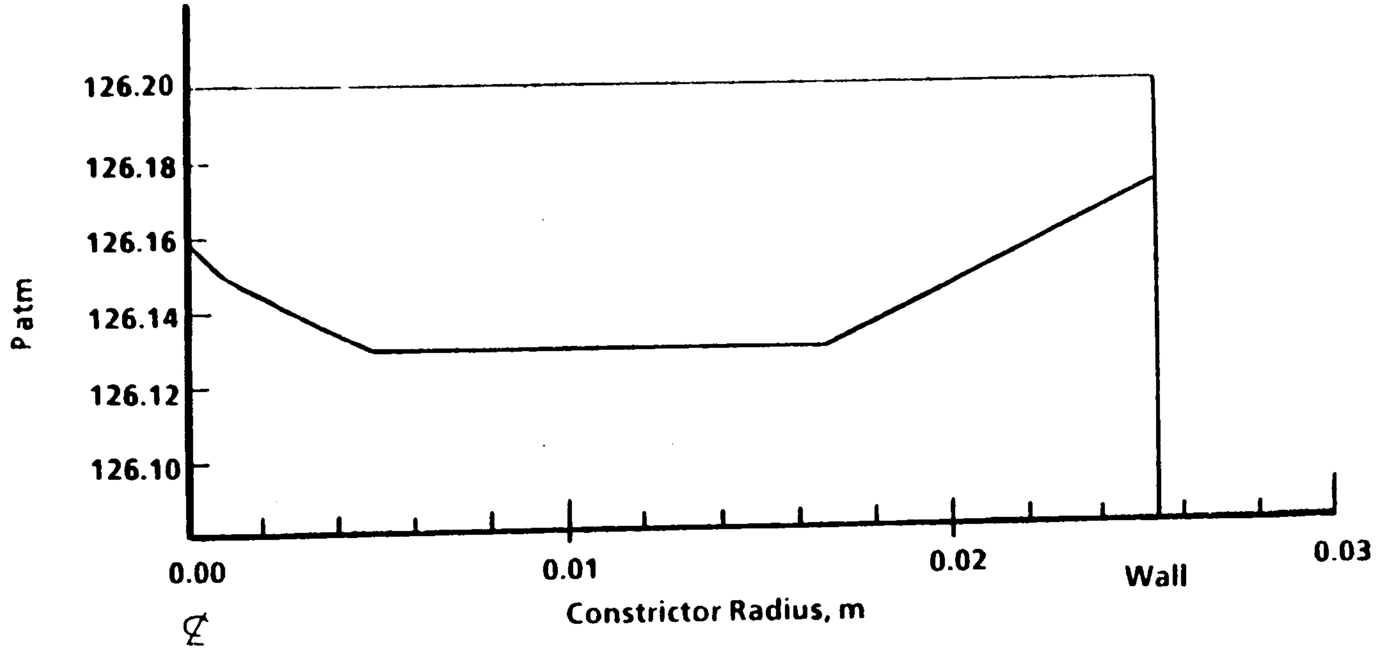

Figure 2-6: Arc Heater Chamber Pressure vs Radius

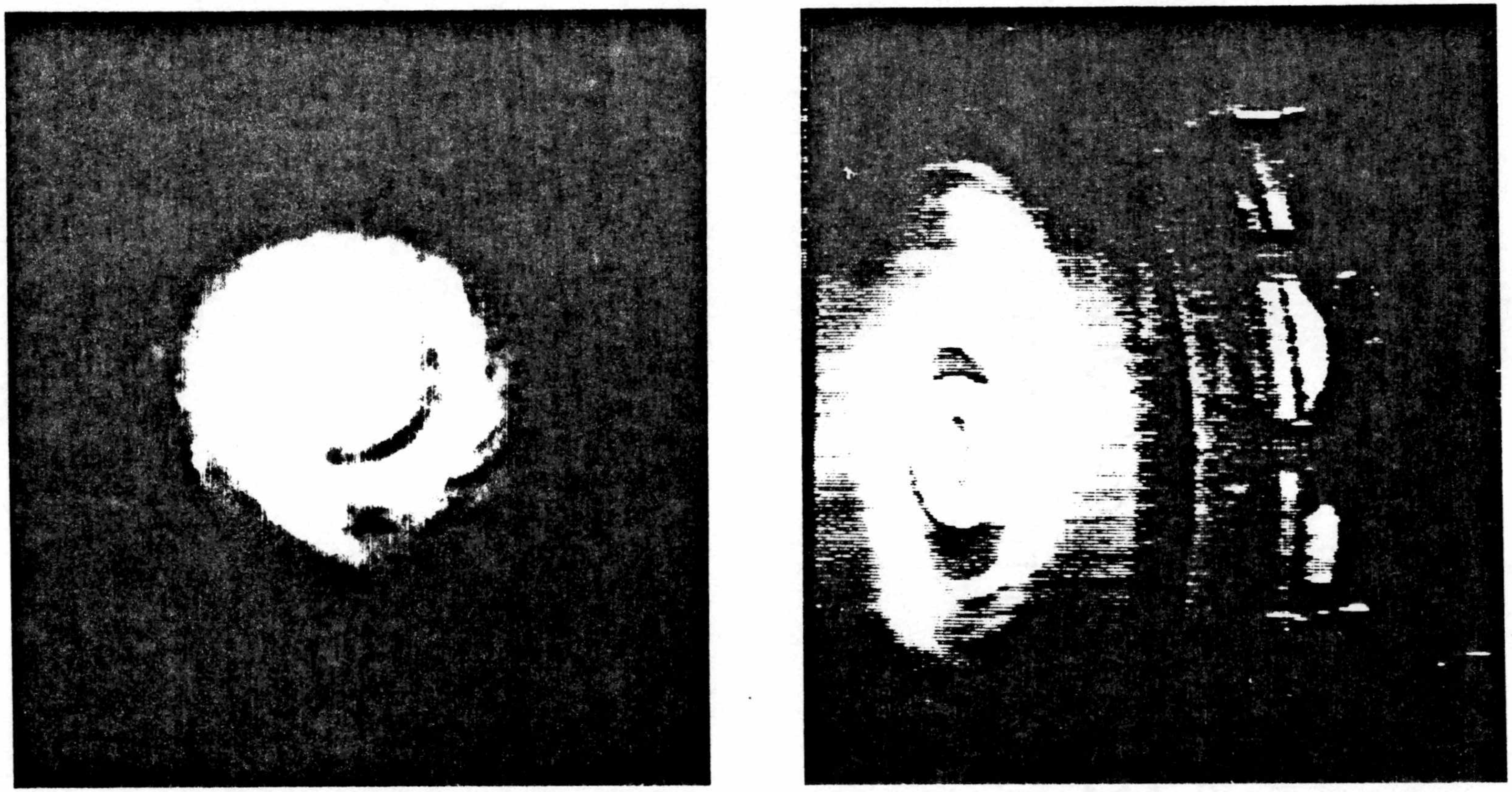

a. HEAT-H1 arc heater swirl flow **b. Laser cross section of the water tunnel swirl flow**

Figure 2-7: Water Tunnel Arc Heater Flow Field Comparison

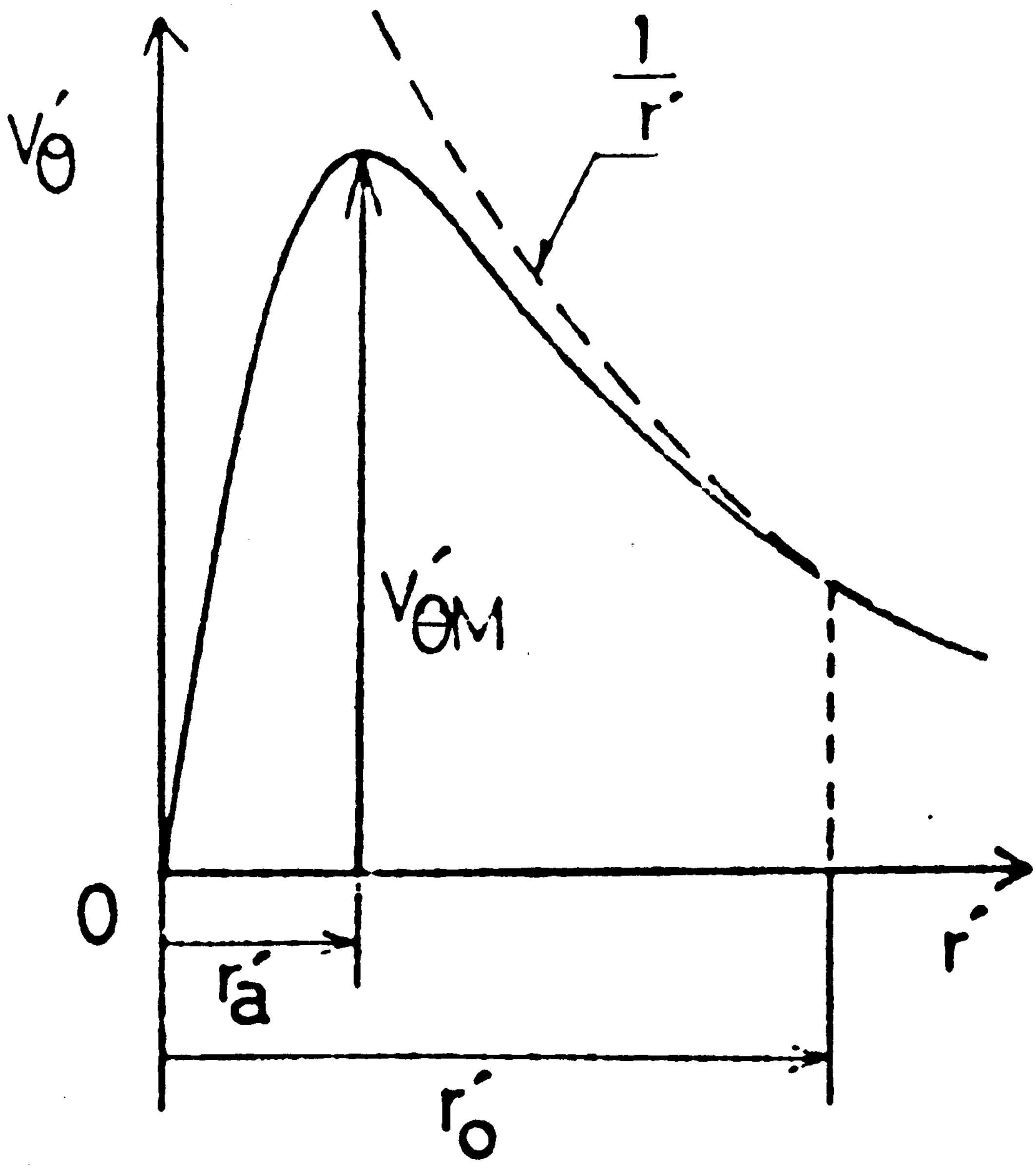

Figure 2-8: Burgers Vortex Model, Main Features

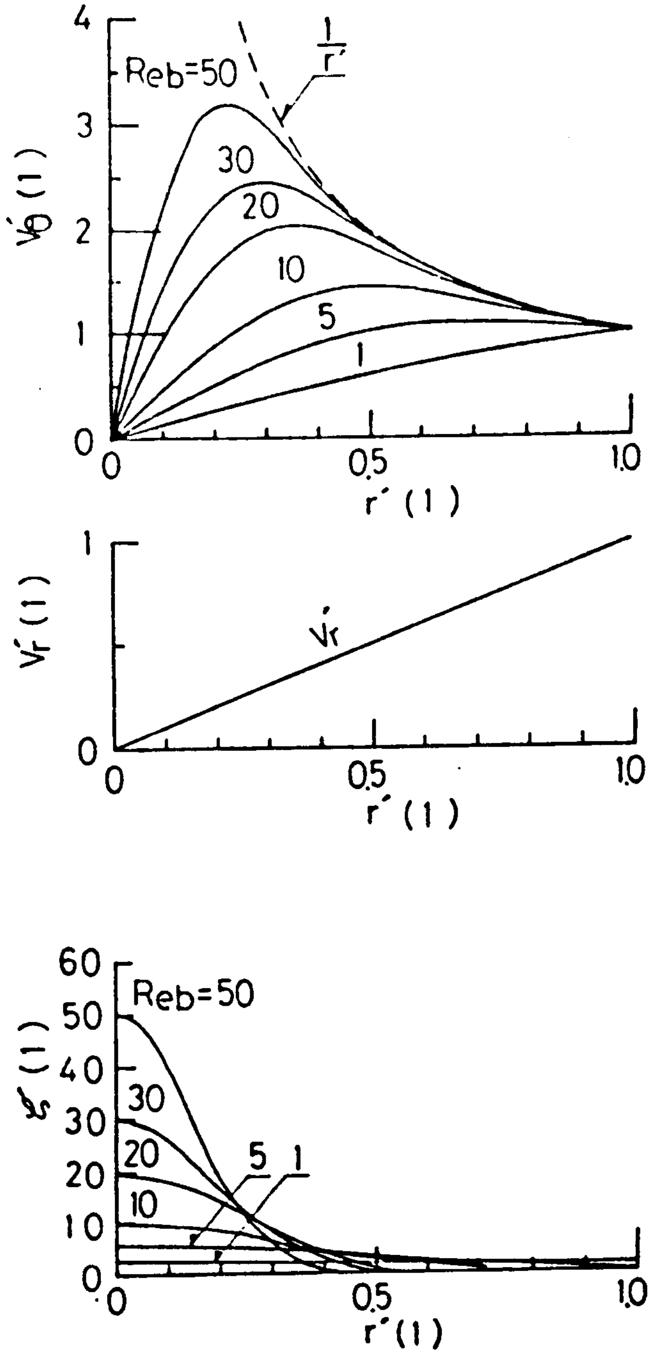

Figure 2-9: Burgers Model vs Re

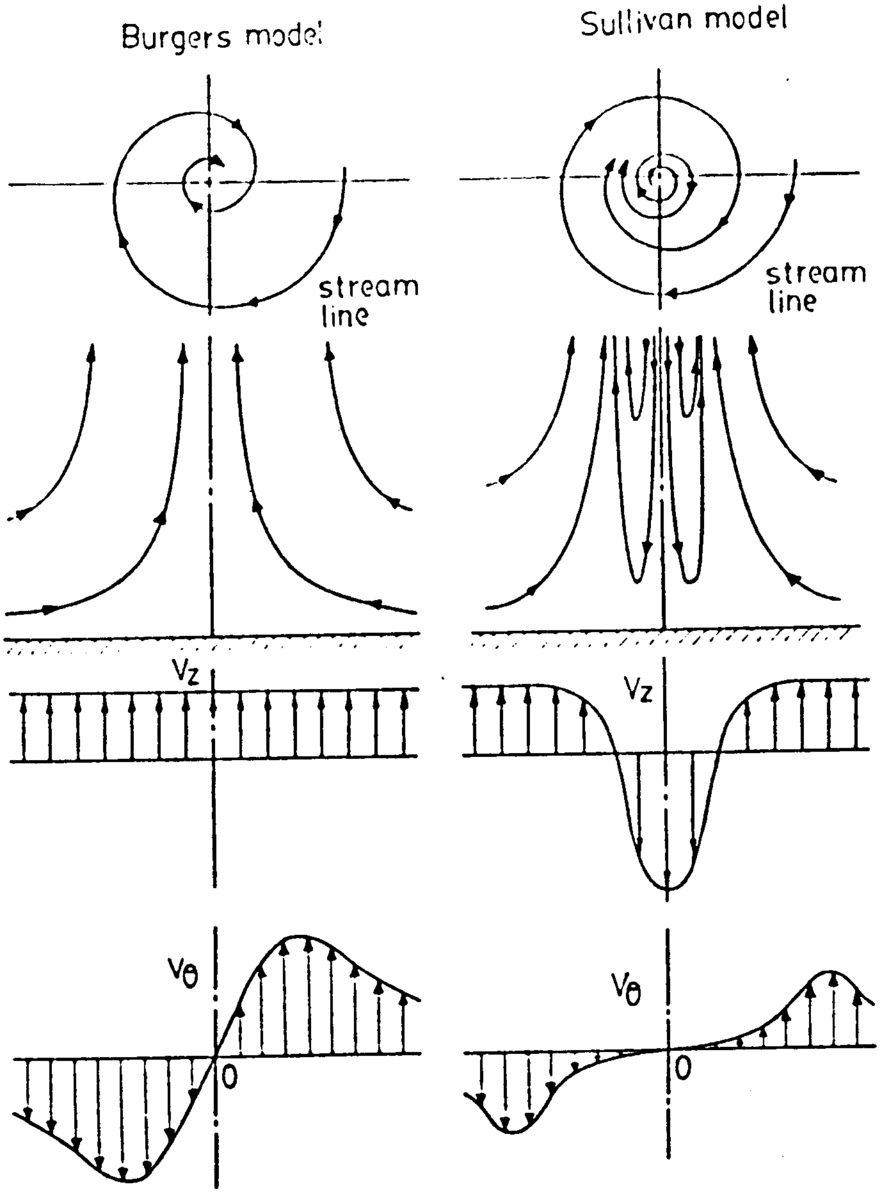

Figure 2-10: Burgers Model vs Sullivan Model

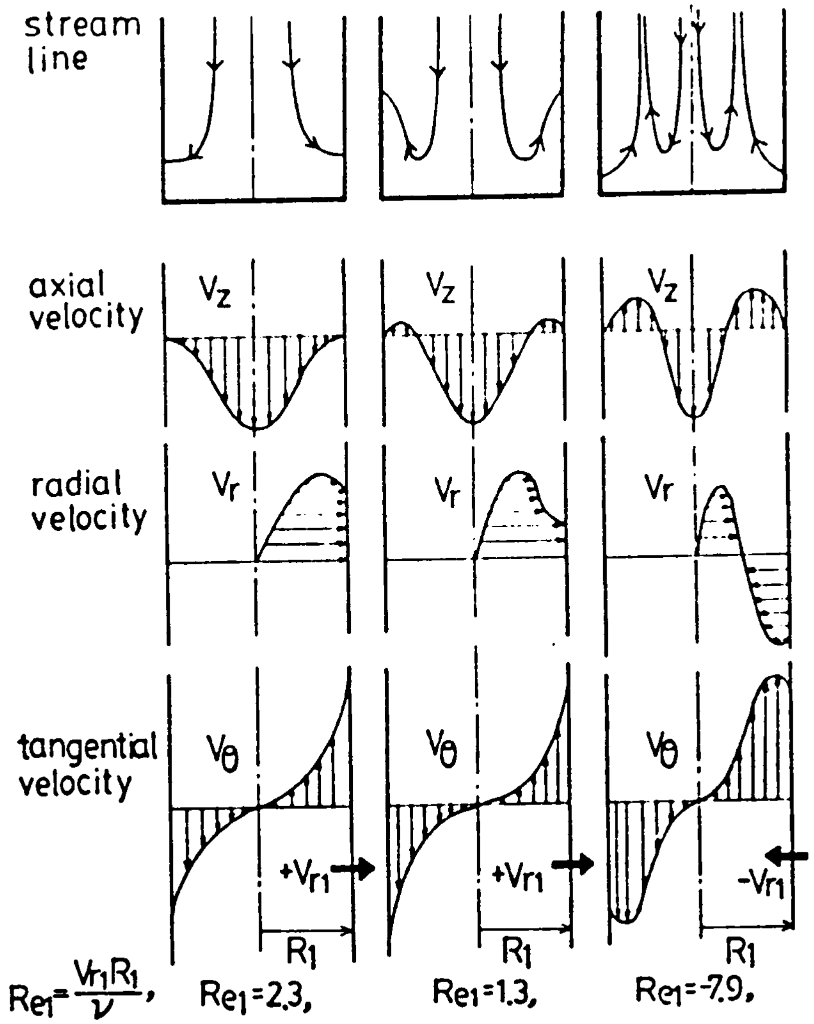

Figure 2-11: Sullivan Model vs Re

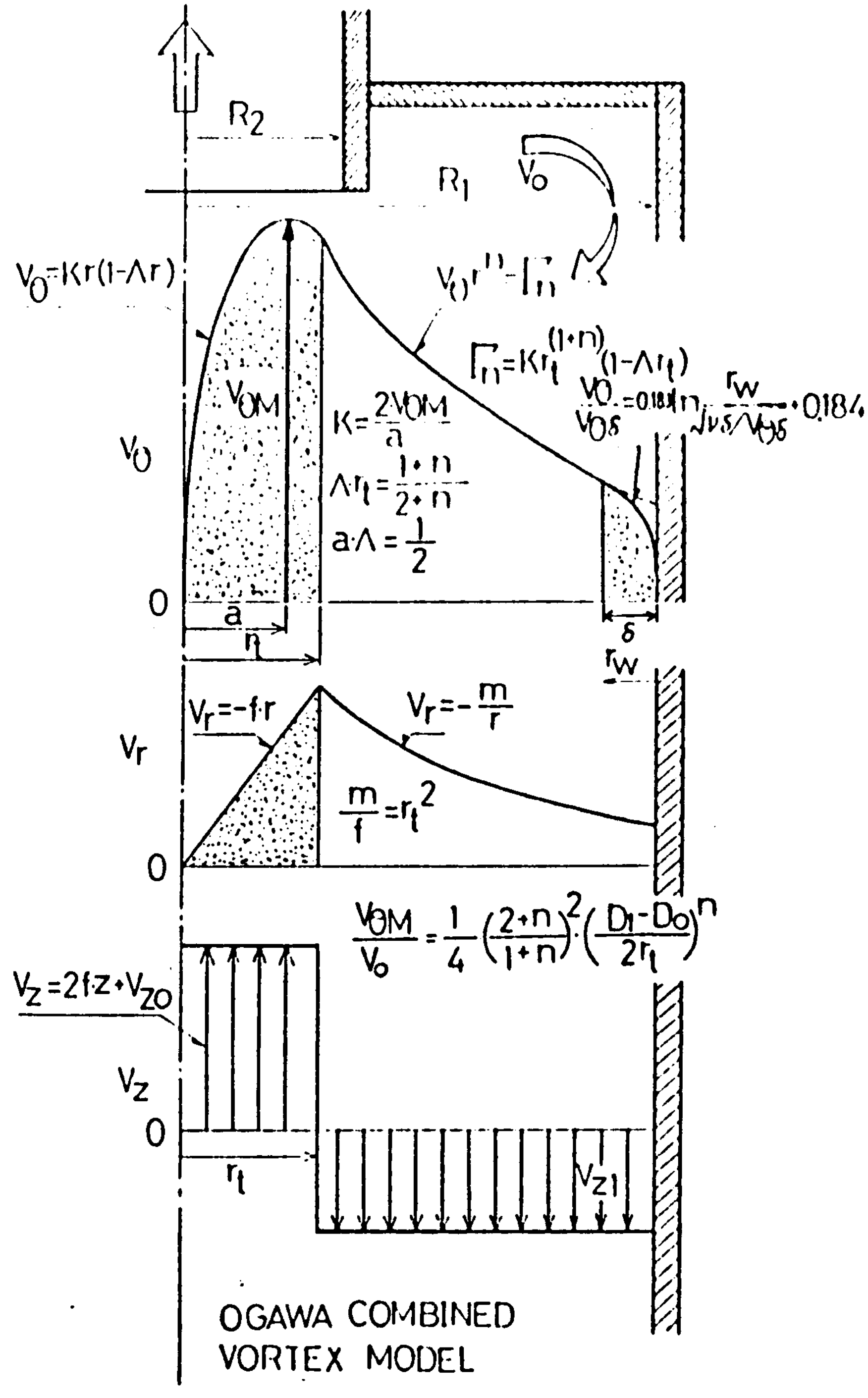

Figure 2-12: Ogawa Combined Vortex Model

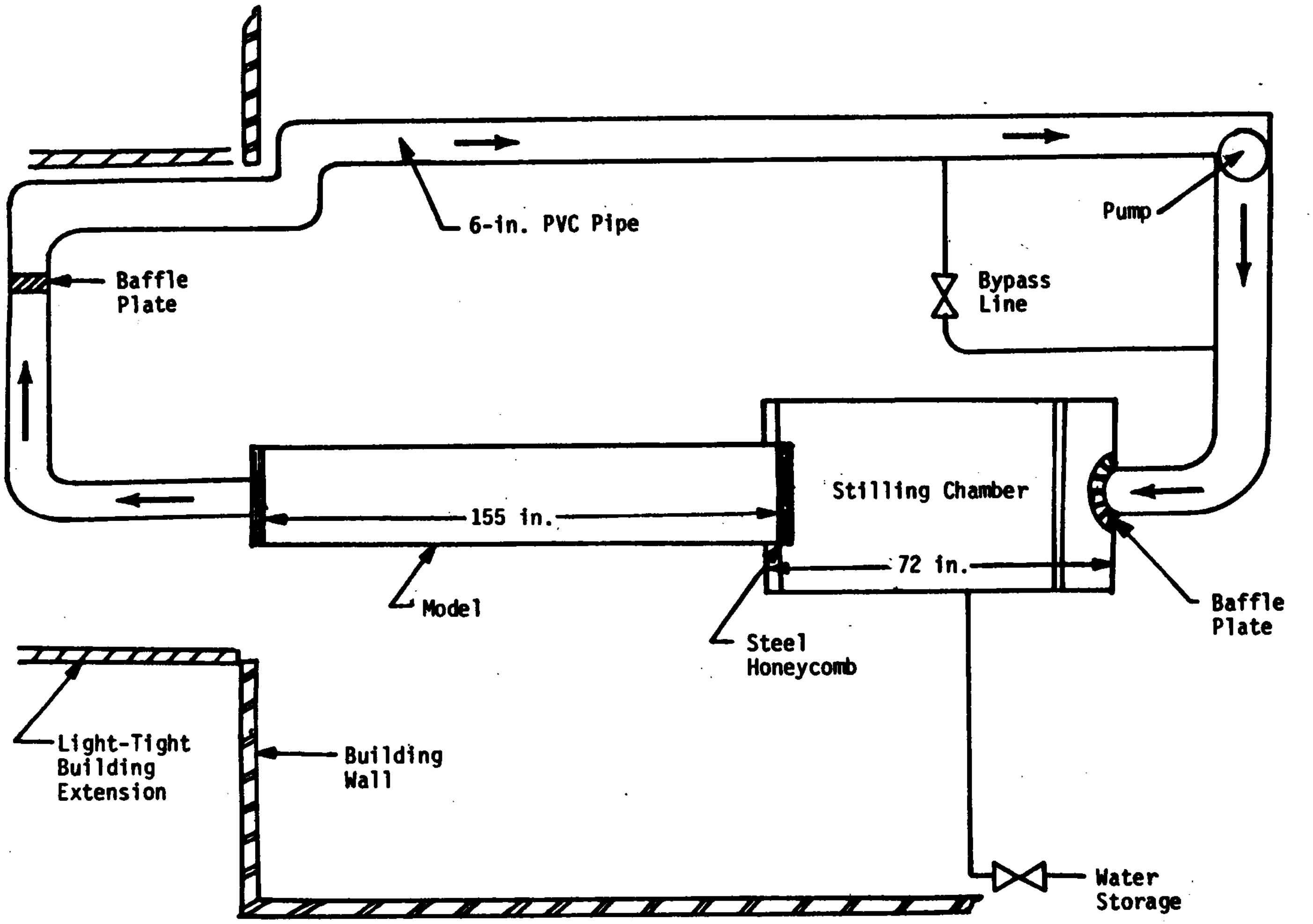

Figure 4-1: UTSI Water Tunnel Facility Layout

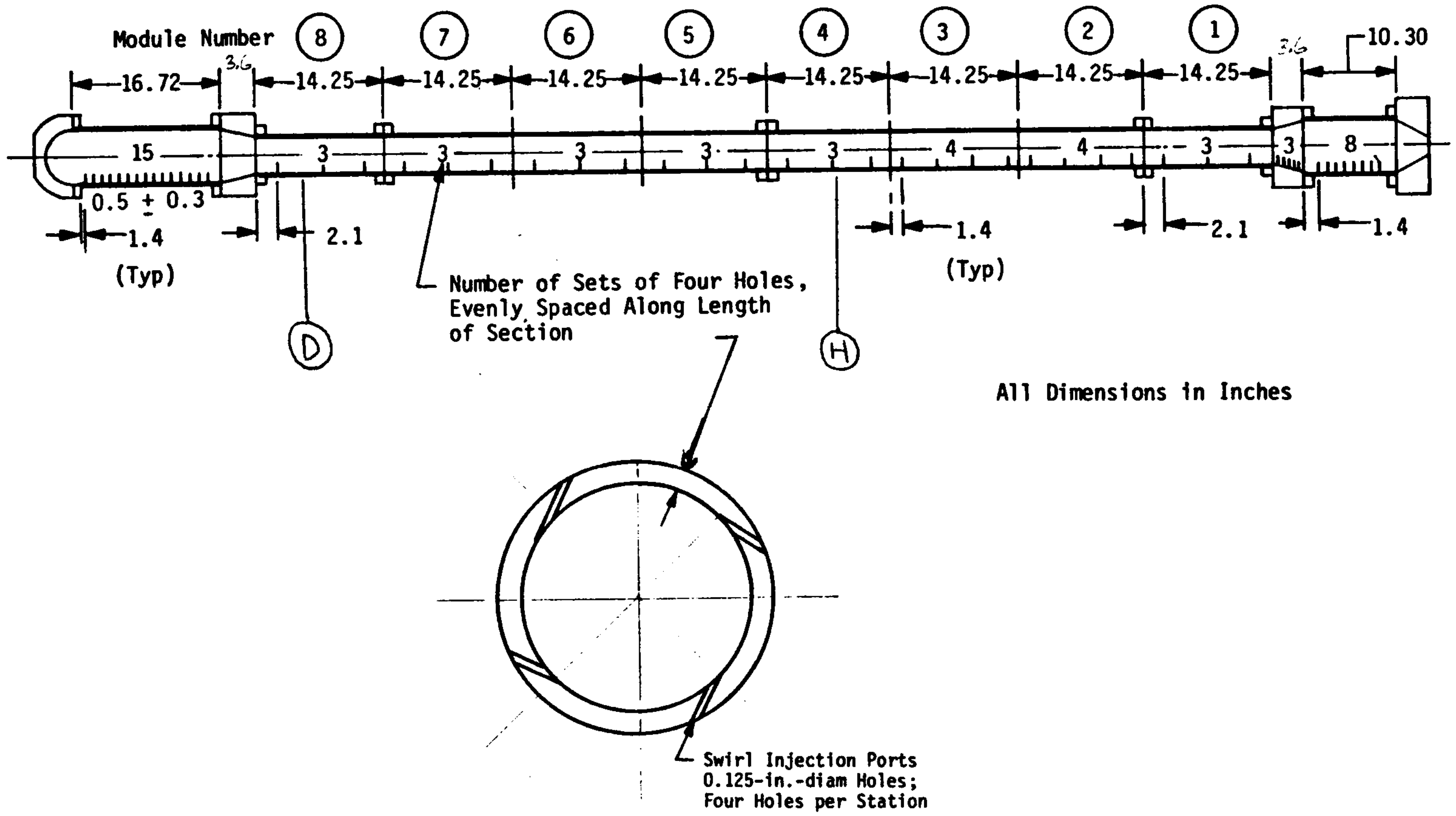

Figure 4-2: Arc Heater Water Tunnel Model (Schematic)

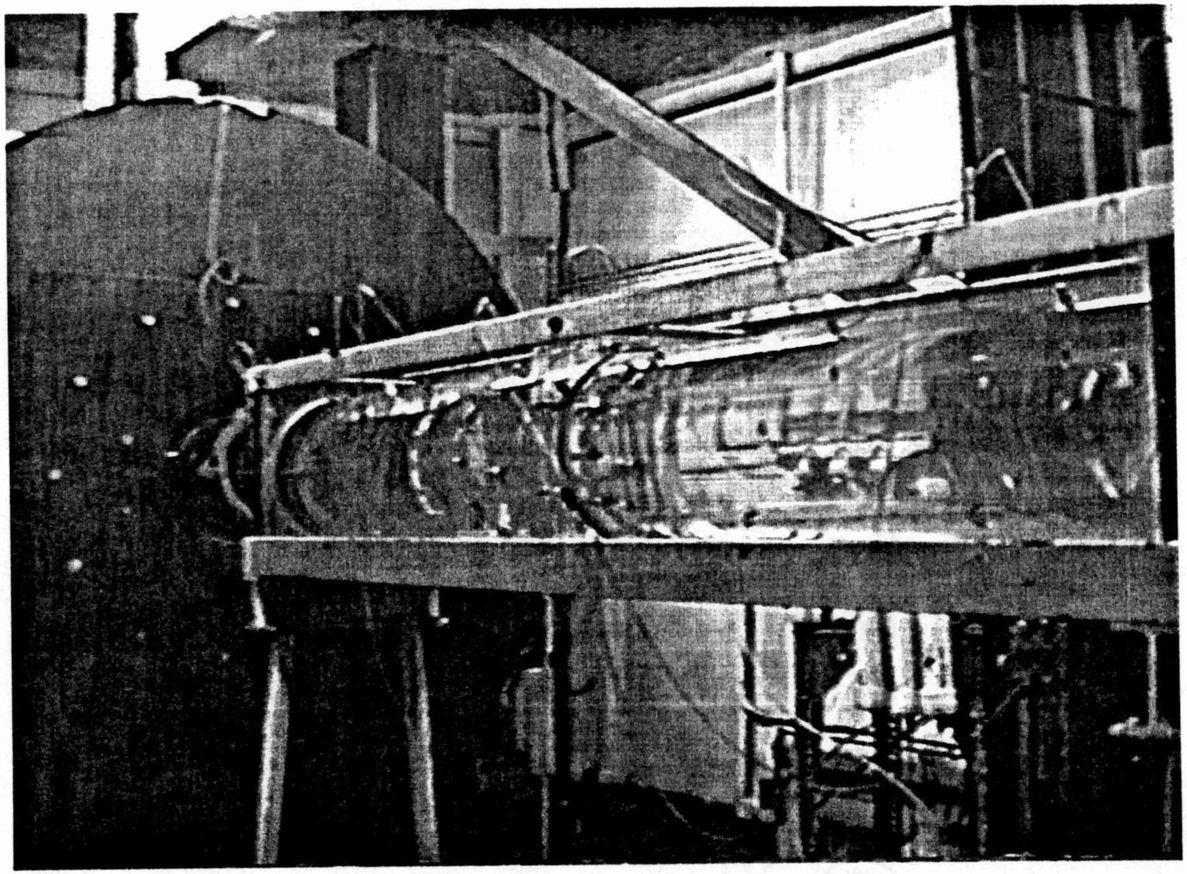

Figure 4-3: Water Tunnel Model (Photograph)

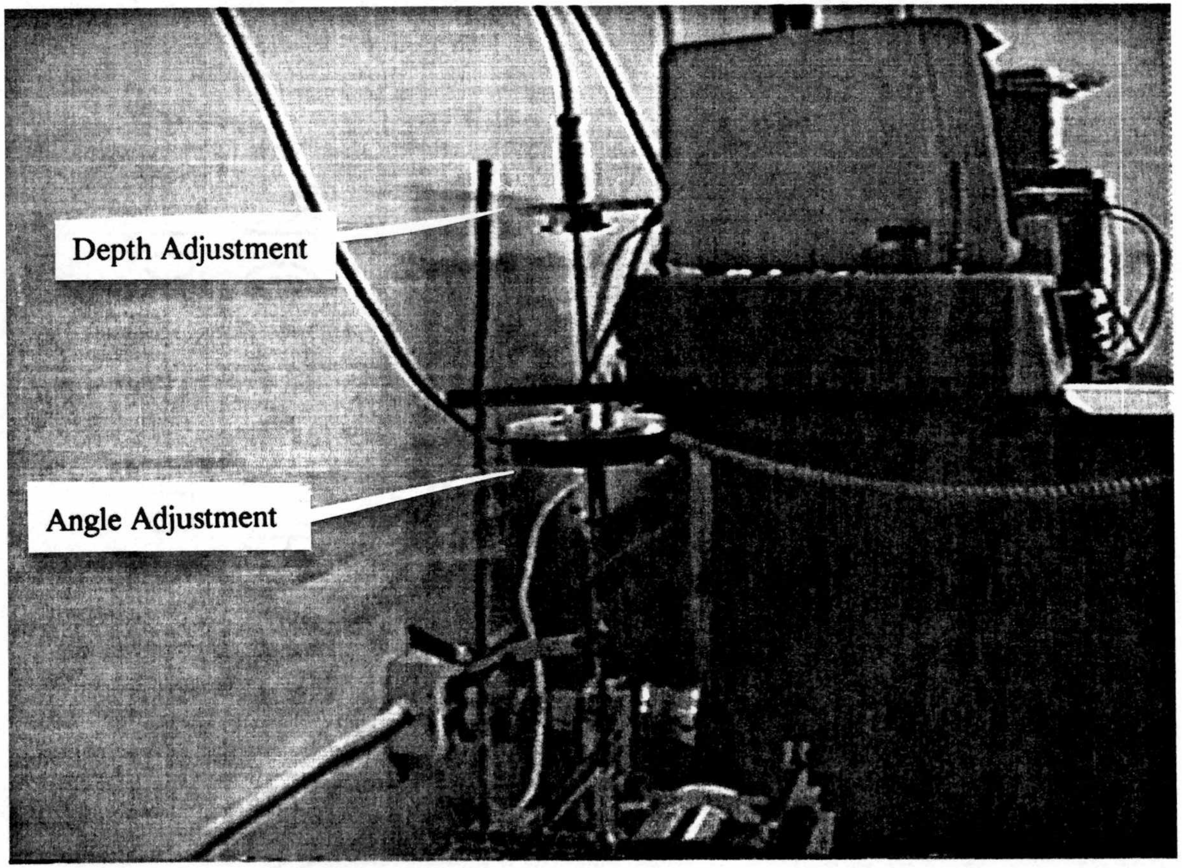

Figure 4-4: Hot Film Probe Injection Device

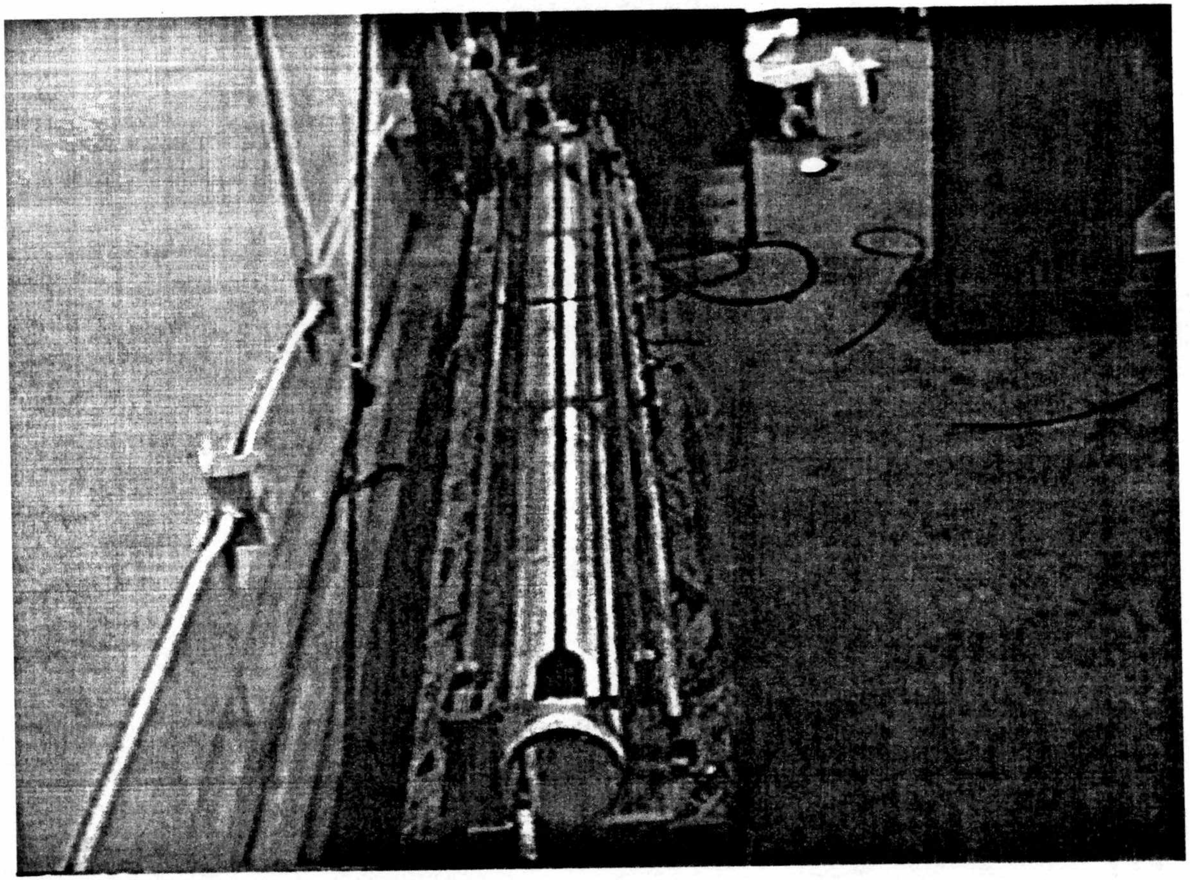

Figure 4-5: Hot Film Probe Calibration Device

Figure 5-1: Flow Visualization: Station H, 5.6 Gal/min, r~0.5 in

Figure 5-2: Flow Visualization: Station H, 5.6 Gal/min, r~1.0 in

Figure 5-3: Flow Visualization: Station H, 5.6 Gal/min, r~1.5 in

Figure 5-4: Flow Visualization: Station H, 5.6 Gal/min, r~2.0 in

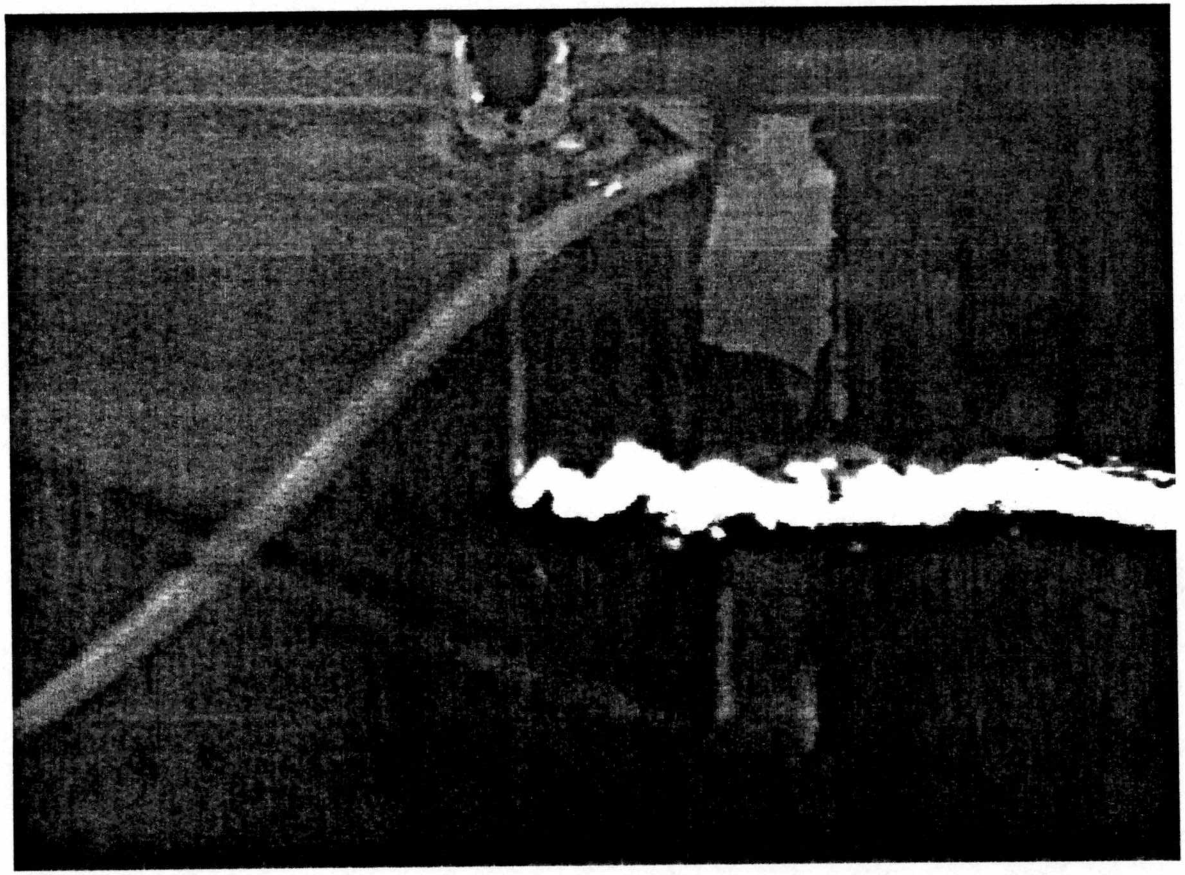

Figure 5-5: Flow Visualization: Station D, 10 Gal/min, r~0.25 in

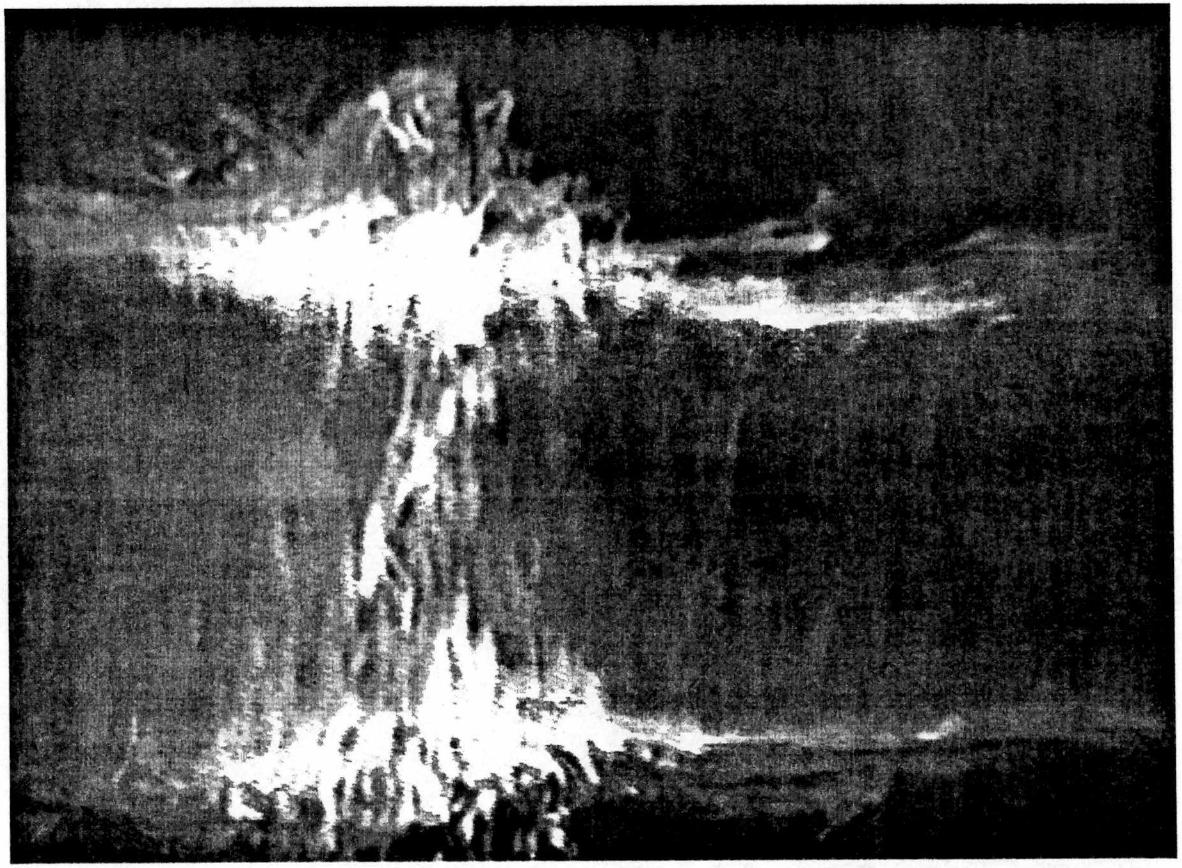

Figure 5-6: Flow Visualization: Station D, 10 Gal/min, r~1.0 in

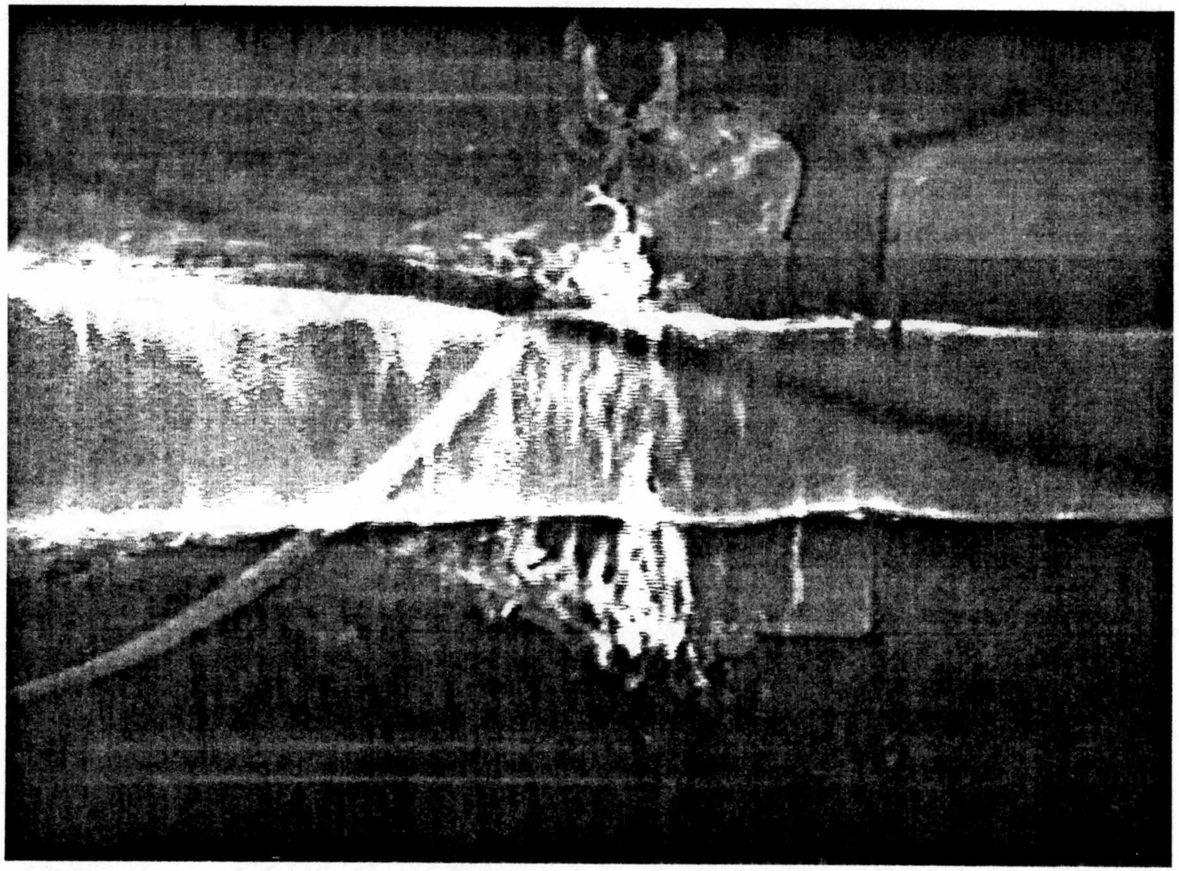

Figure 5-7: Flow Visualization: Station D, 10 Gal/min, r~1.5 in

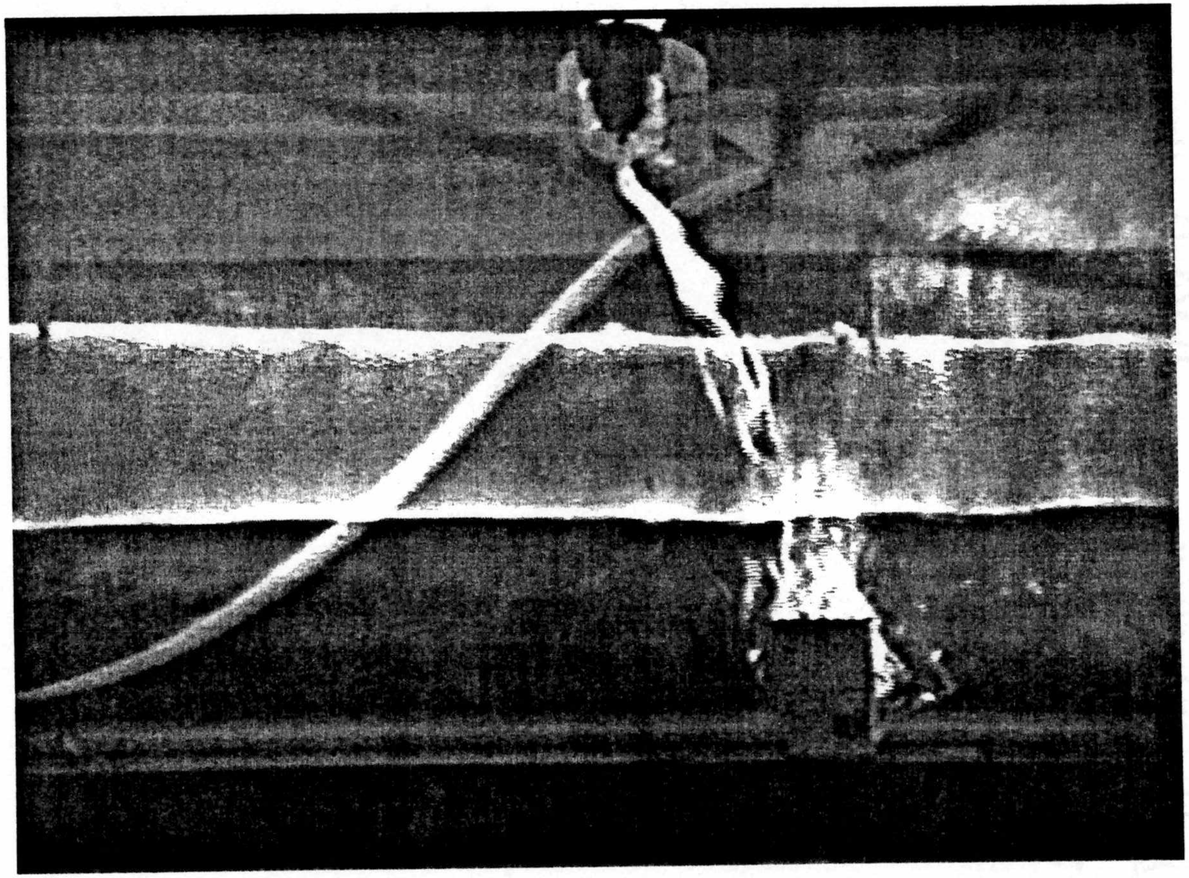

Figure 5-8: Flow Visualization: Station D, 10 Gal/min, r~2.0 in

Flow Rate	10 gal/min
Injection Station	D
Probe θ	0 degrees
Radius	0.3 inches
Band Width	14.5 mHz
First Peak	
Magnitude	19 mV
Frequency	0.744 Hz
Second Peak	
Magnitude	21.5 mV
Frequency	0.776 Hz

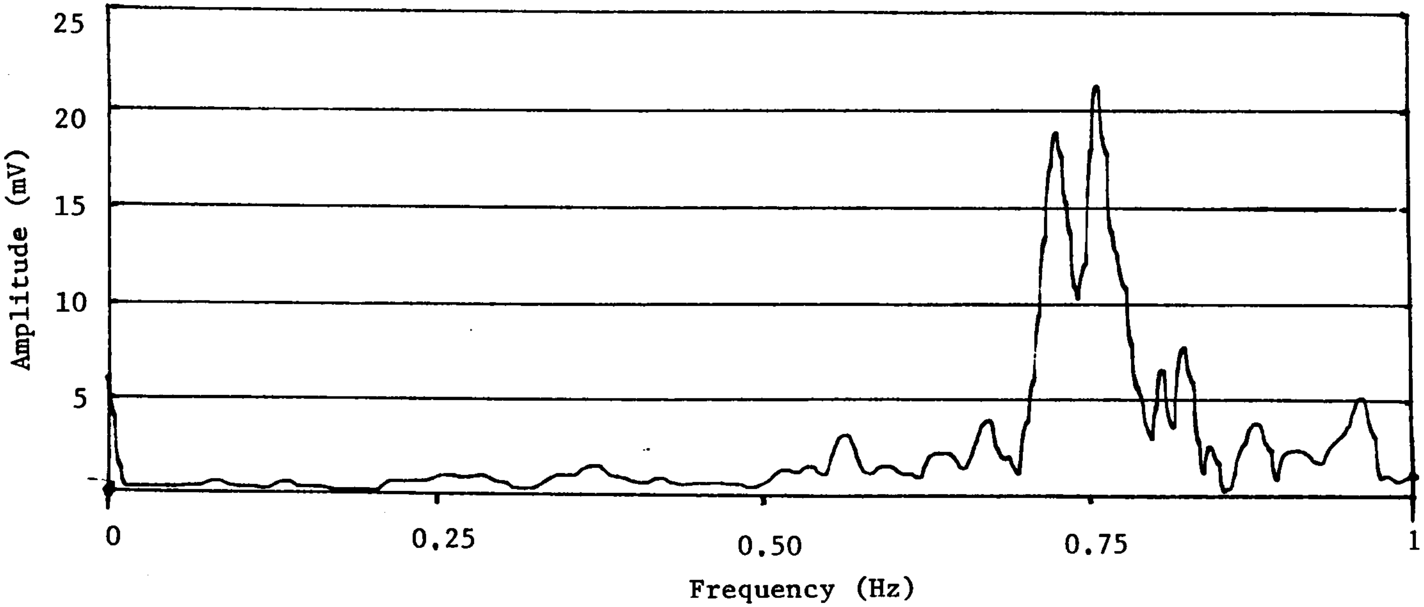

Figure 5-9: Fast Fourier Transform, 0-1 Hz

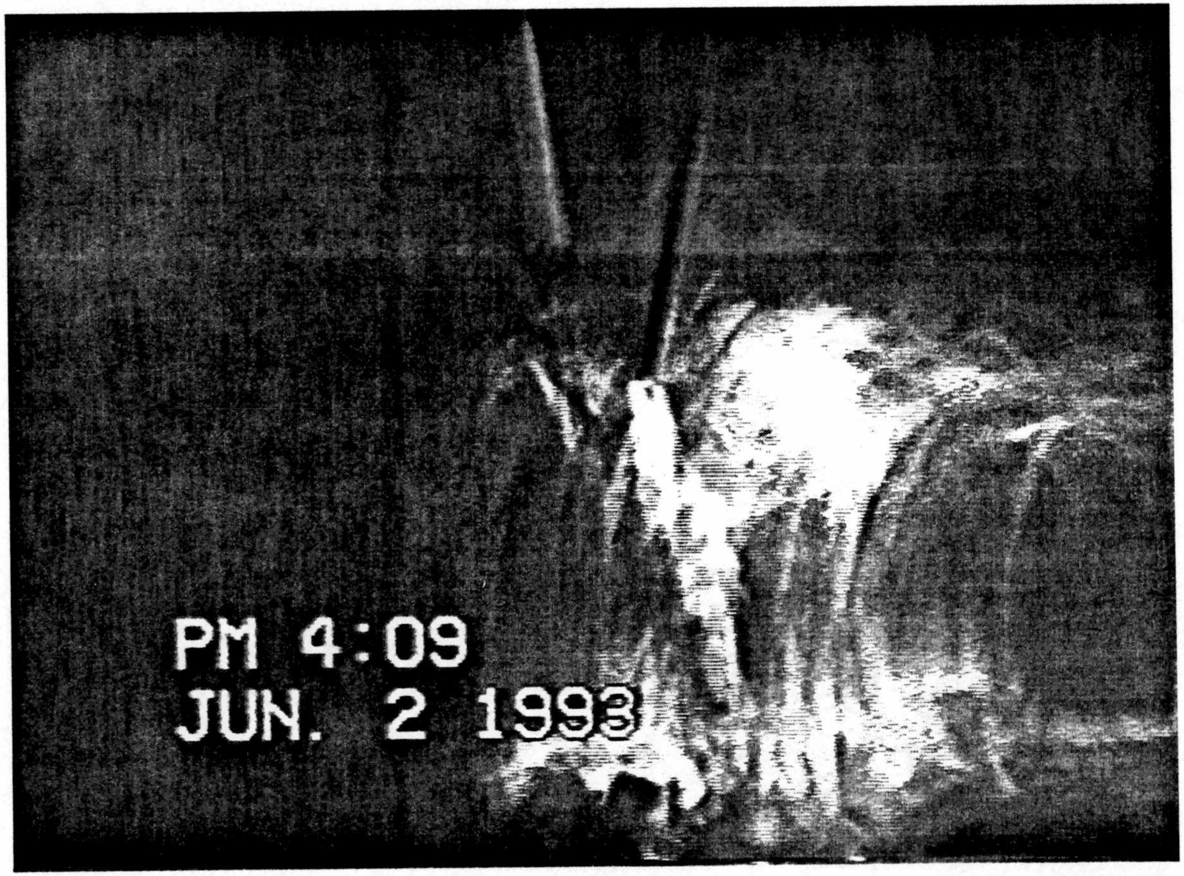

Figure 5-10: Hot film Probe Interference, r > 0.5 in

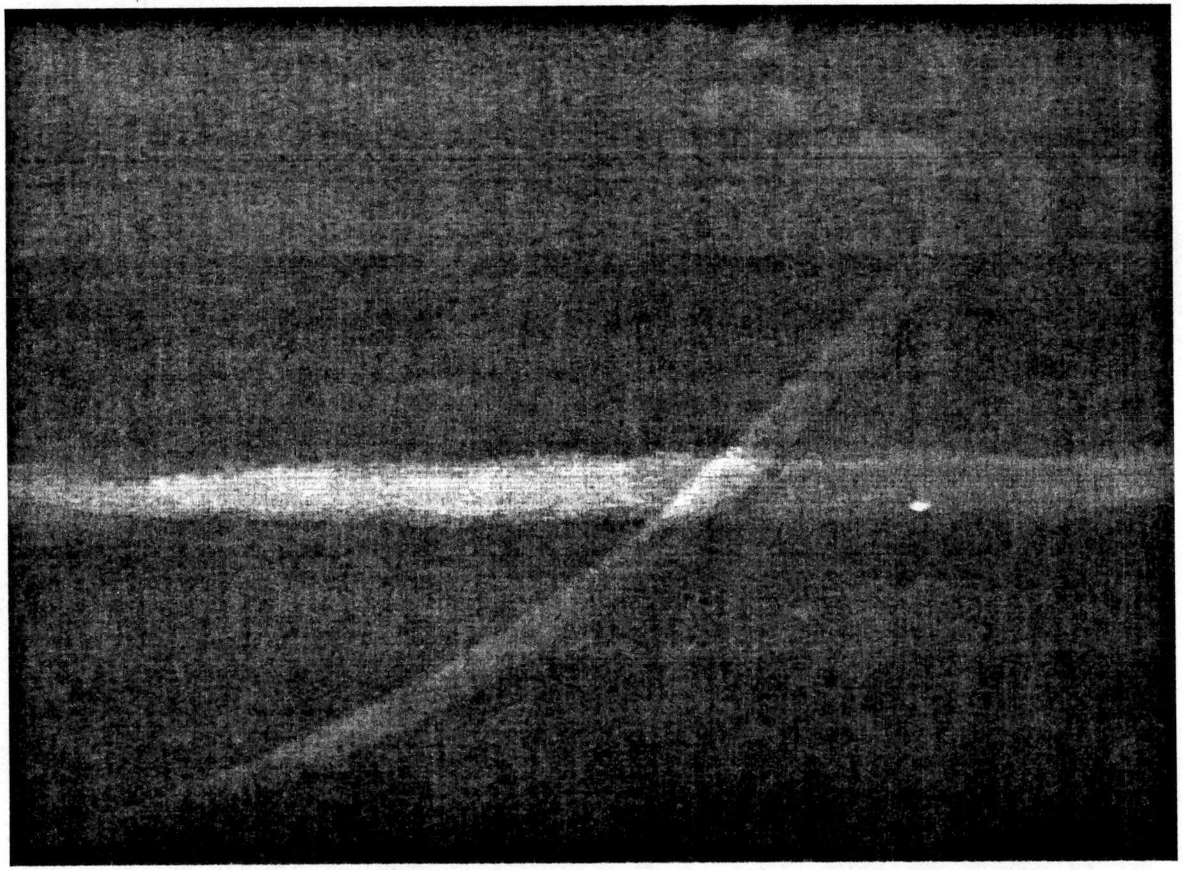

Figure 5-11: Hot film Probe Interference, No probe

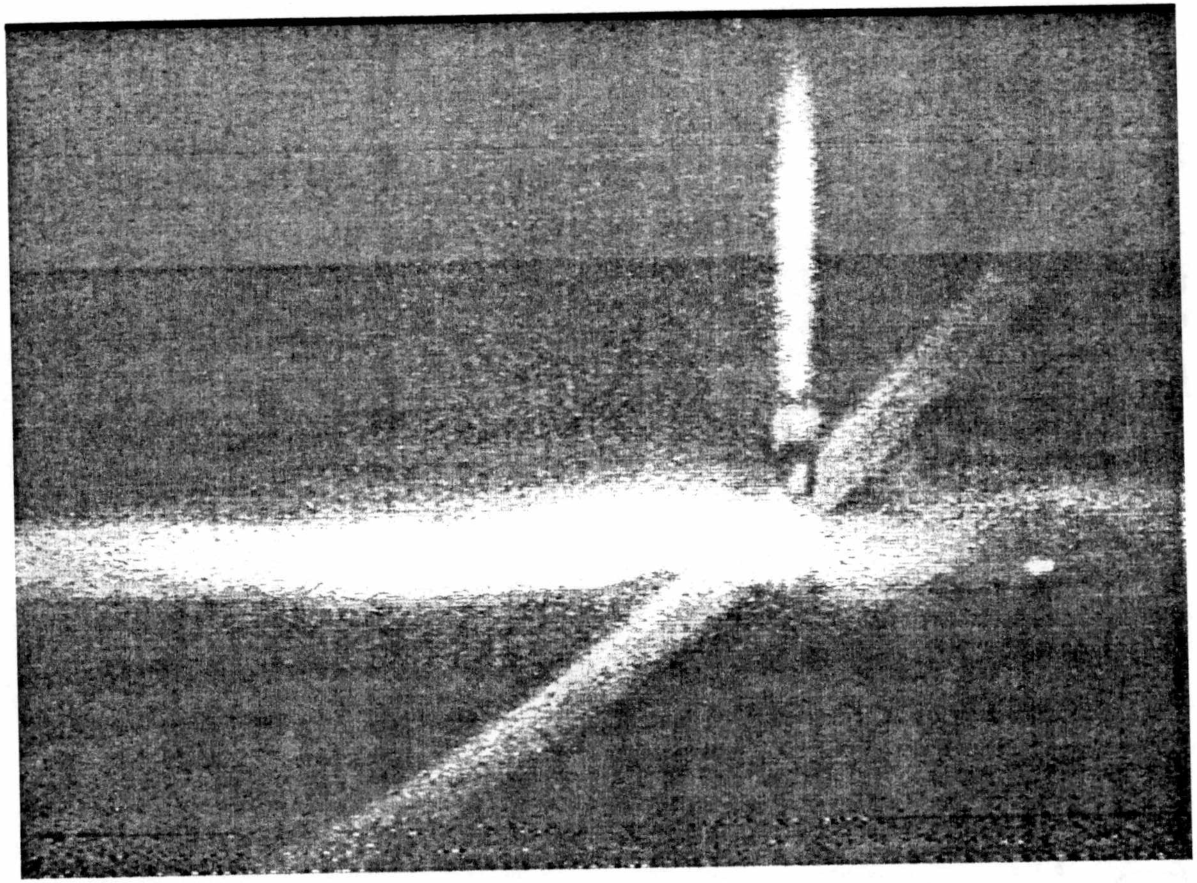

Figure 5-12: Hot film Probe Interference, r < 0.5 in

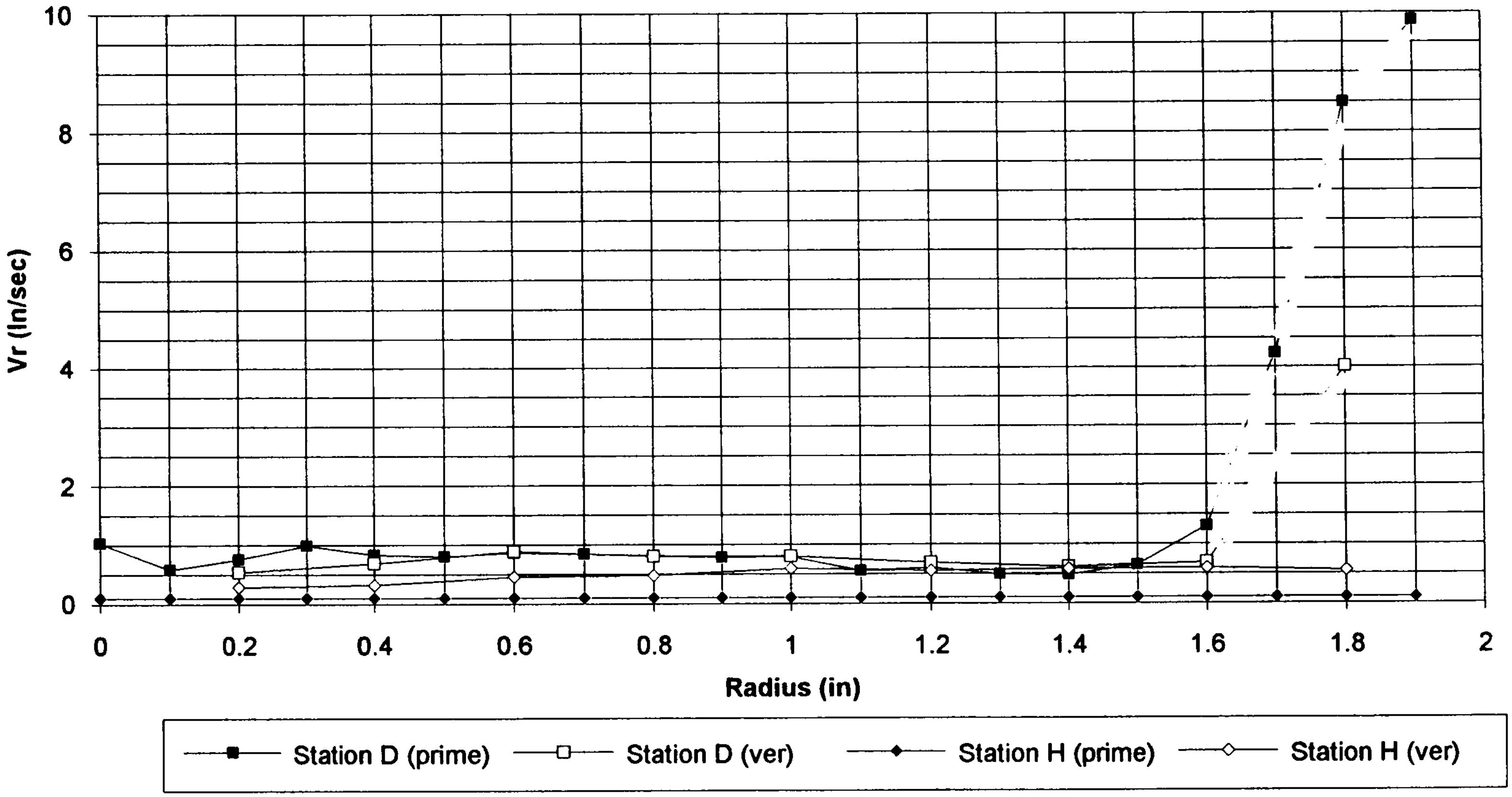

Figure 5-13: V_r , 5.6 gal/min

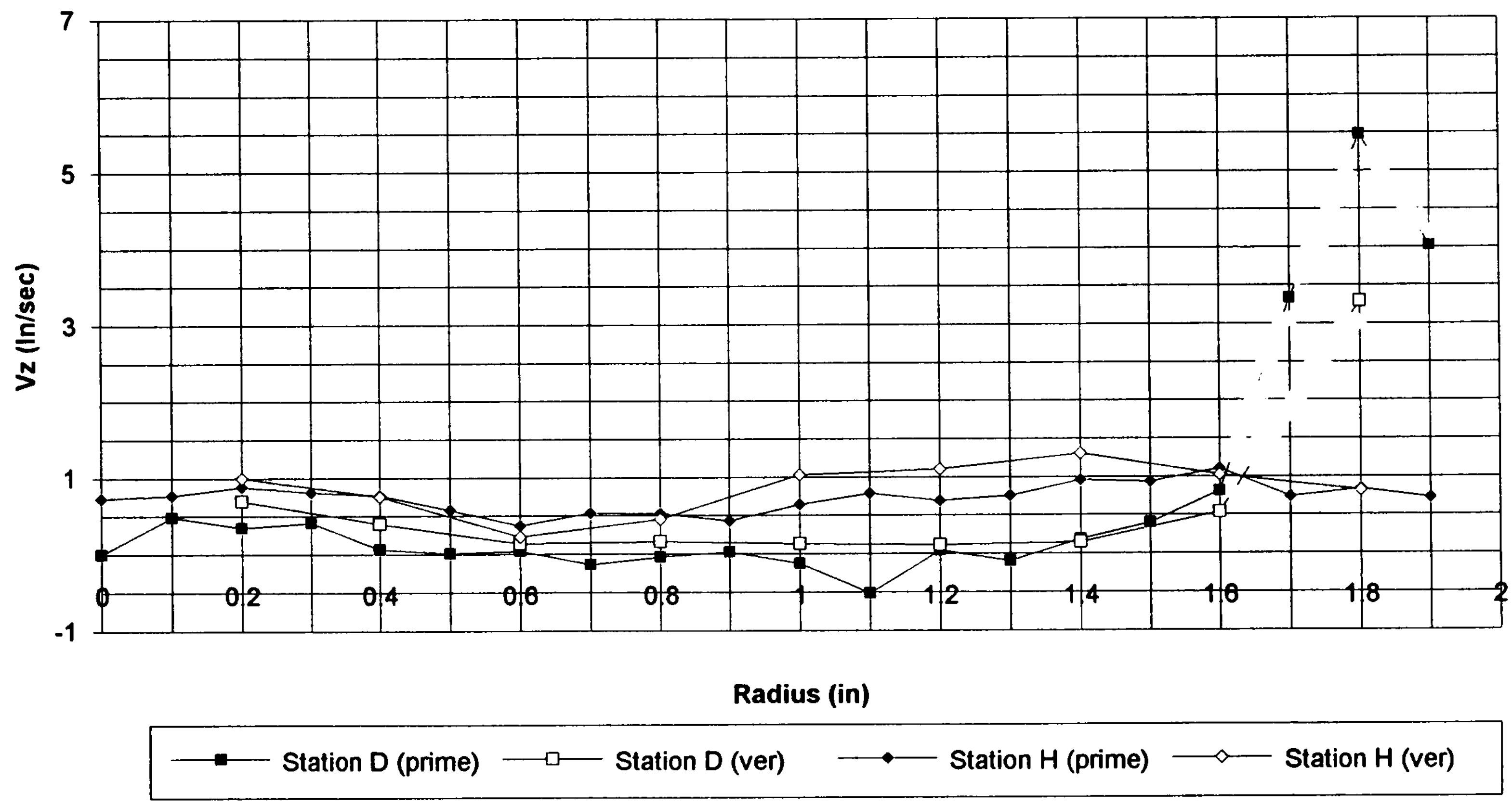

Figure 5-14: V_z , 5.6 gal/min

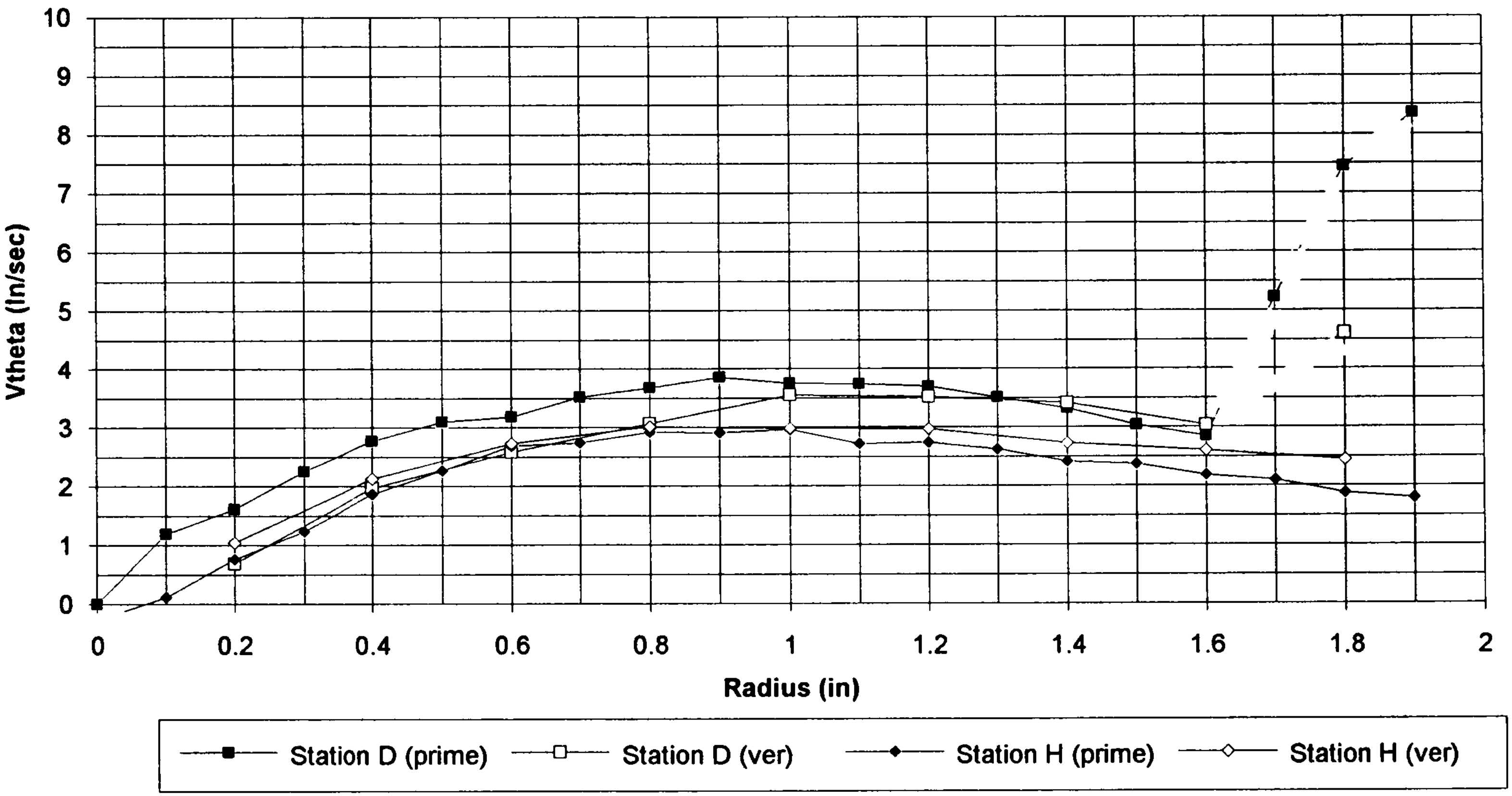

Figure 5-15: V_θ , 5.6 gal/min

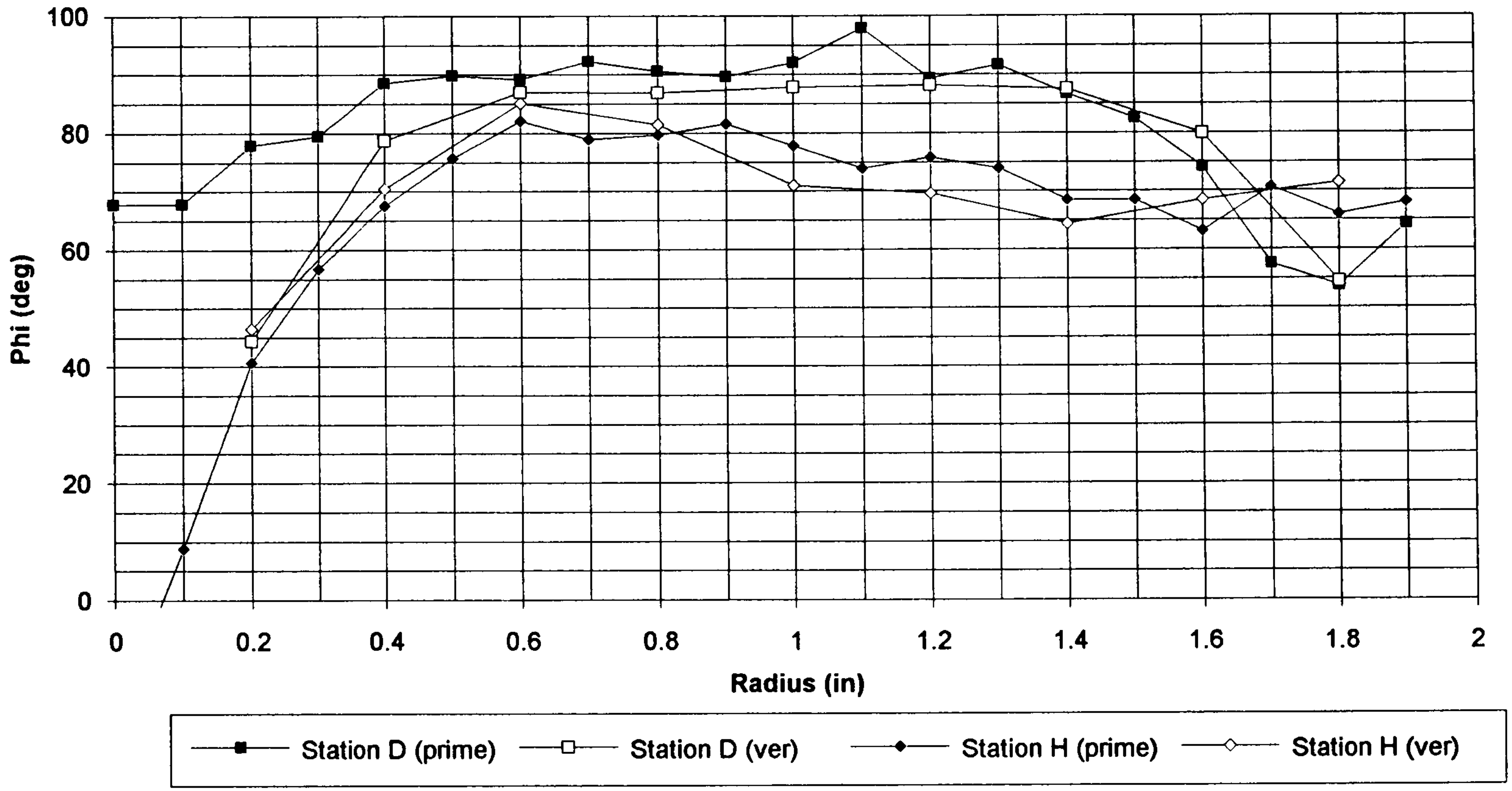

Figure 5-16: Phi , 5.6 gal/min

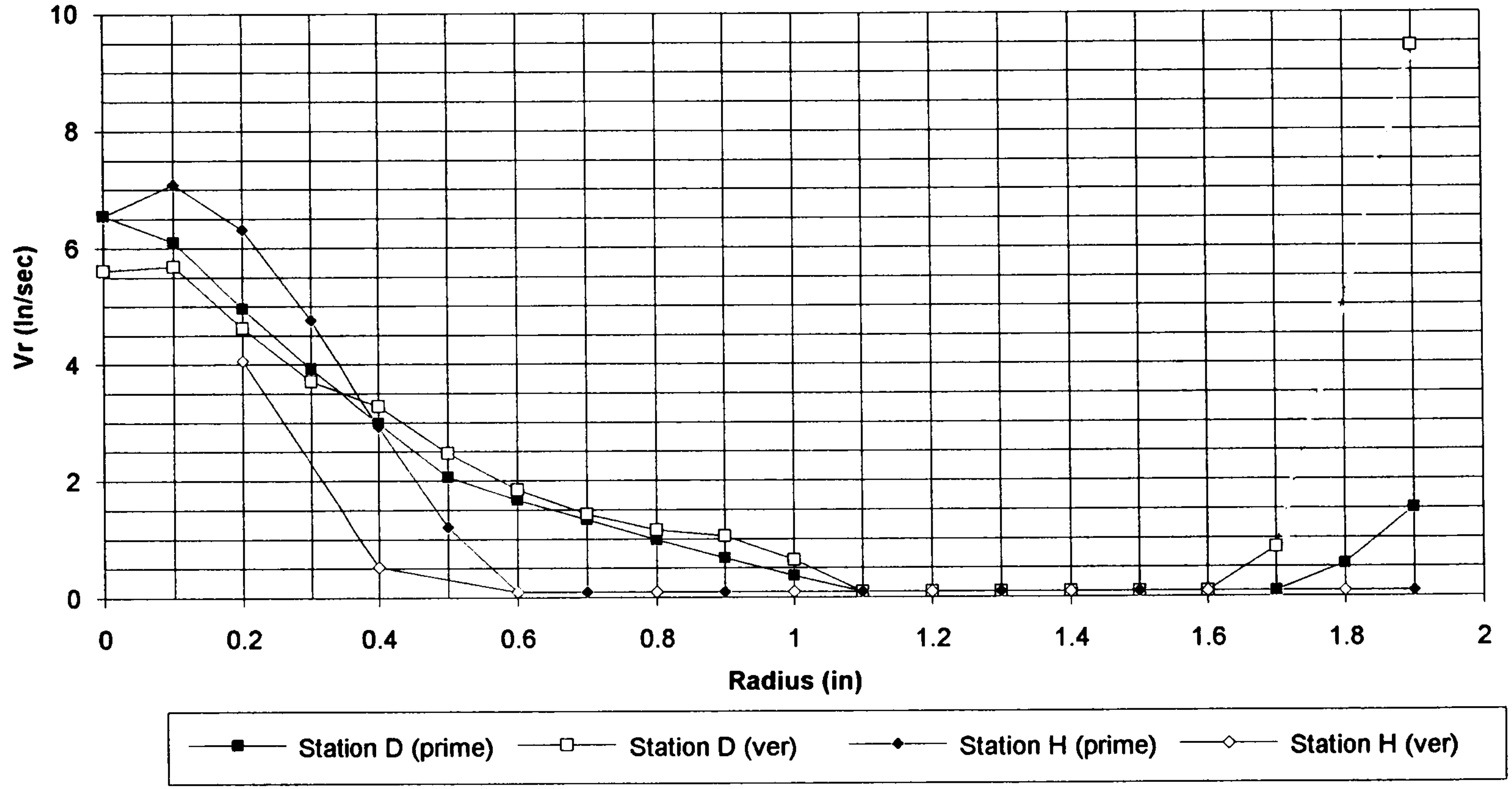

Figure 5-17: V_r, 10 gal/min

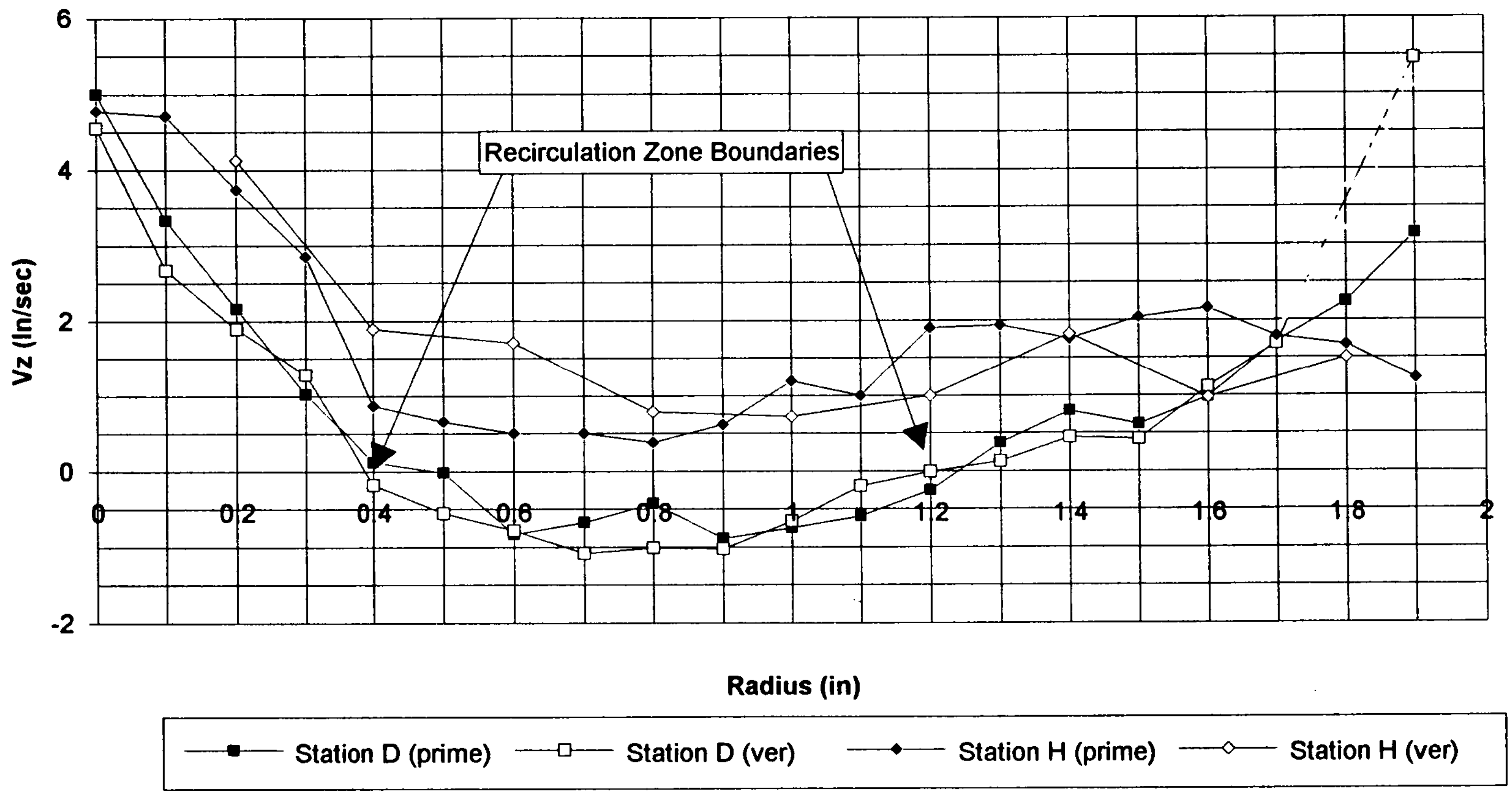

Figure 5-18: V_z, 10 gal/min

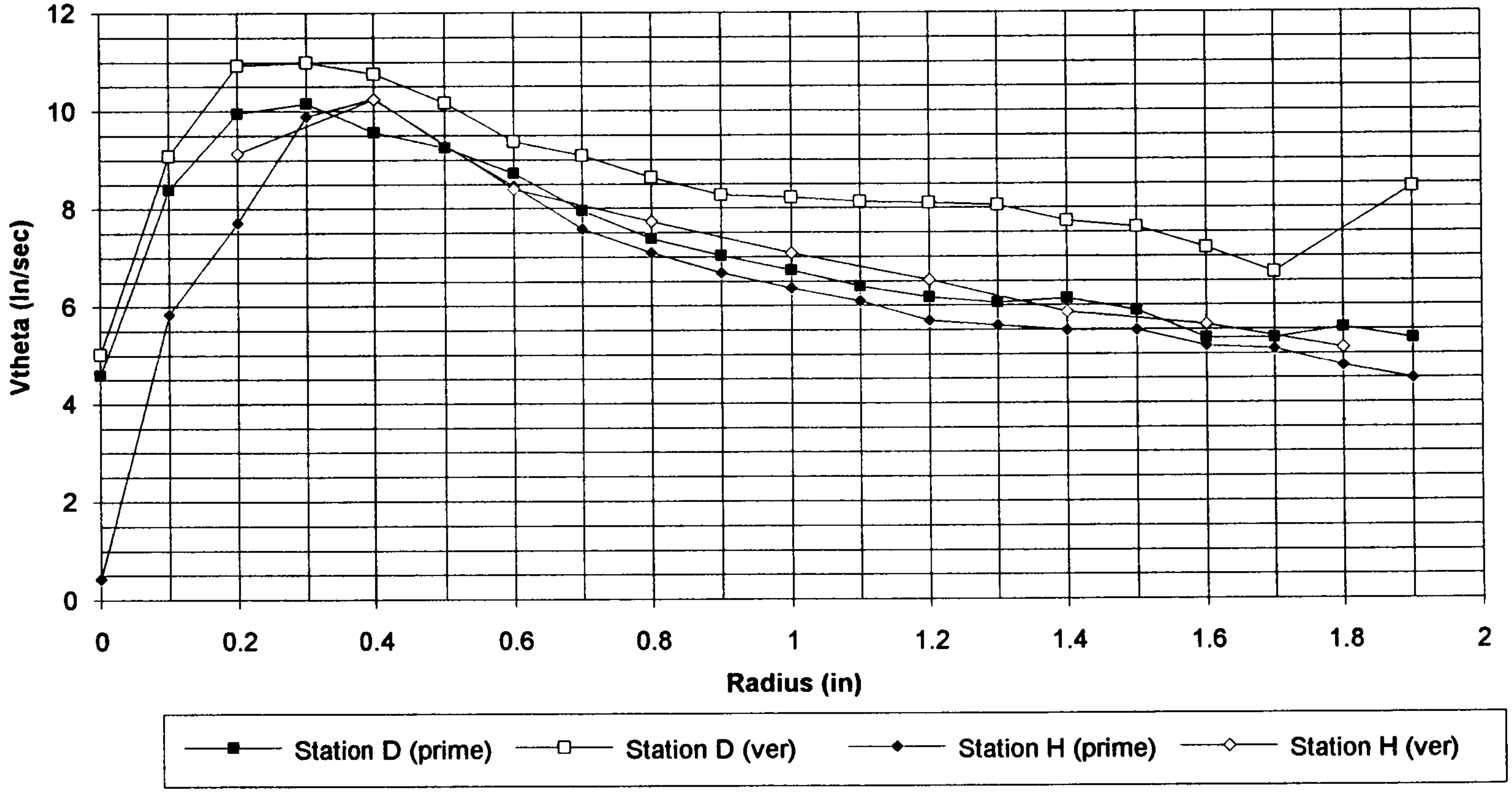

Figure 5-19: V_θ , 10 gal/min

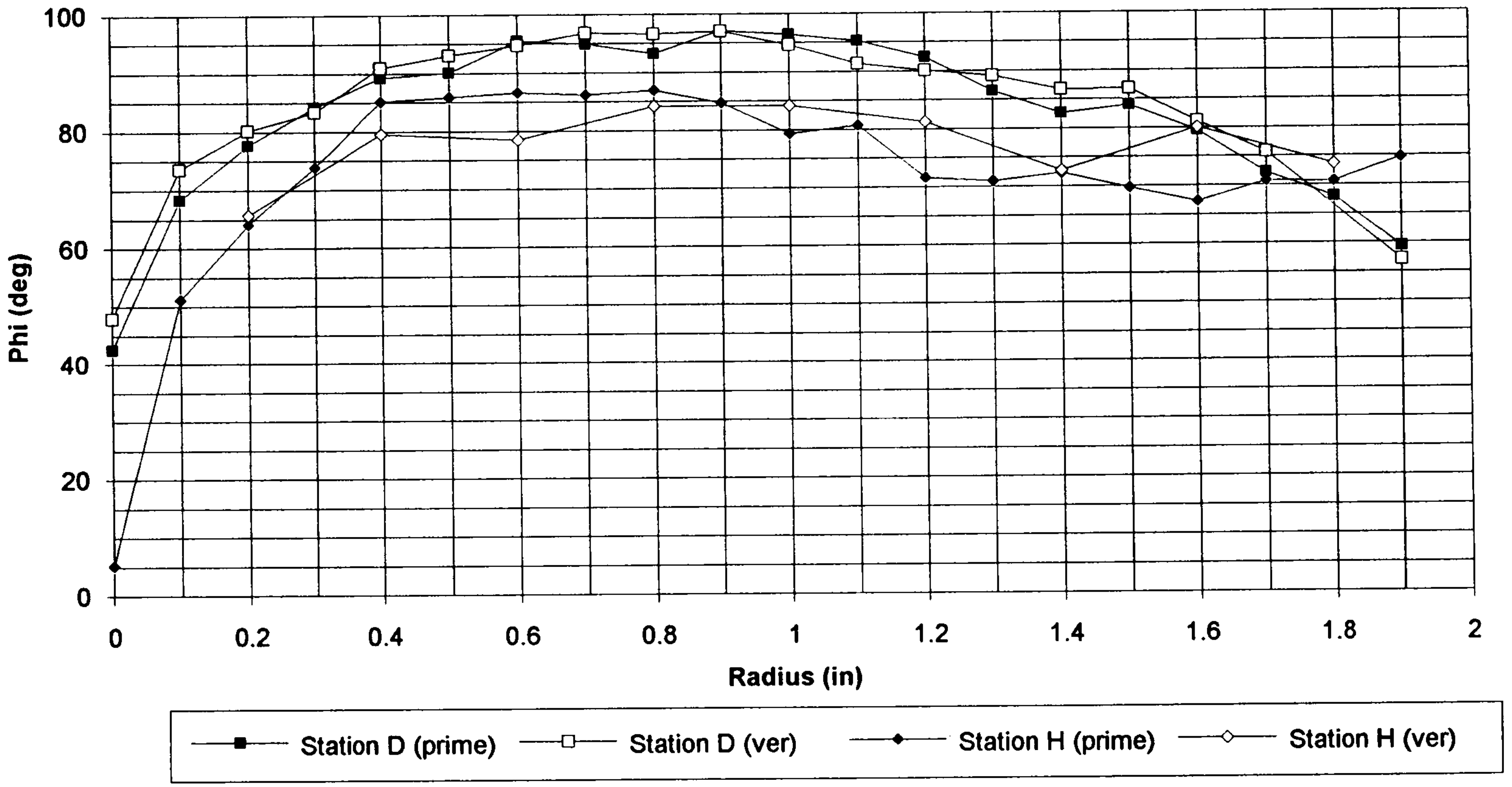

Figure 5-20: Phi, 10 gal/min

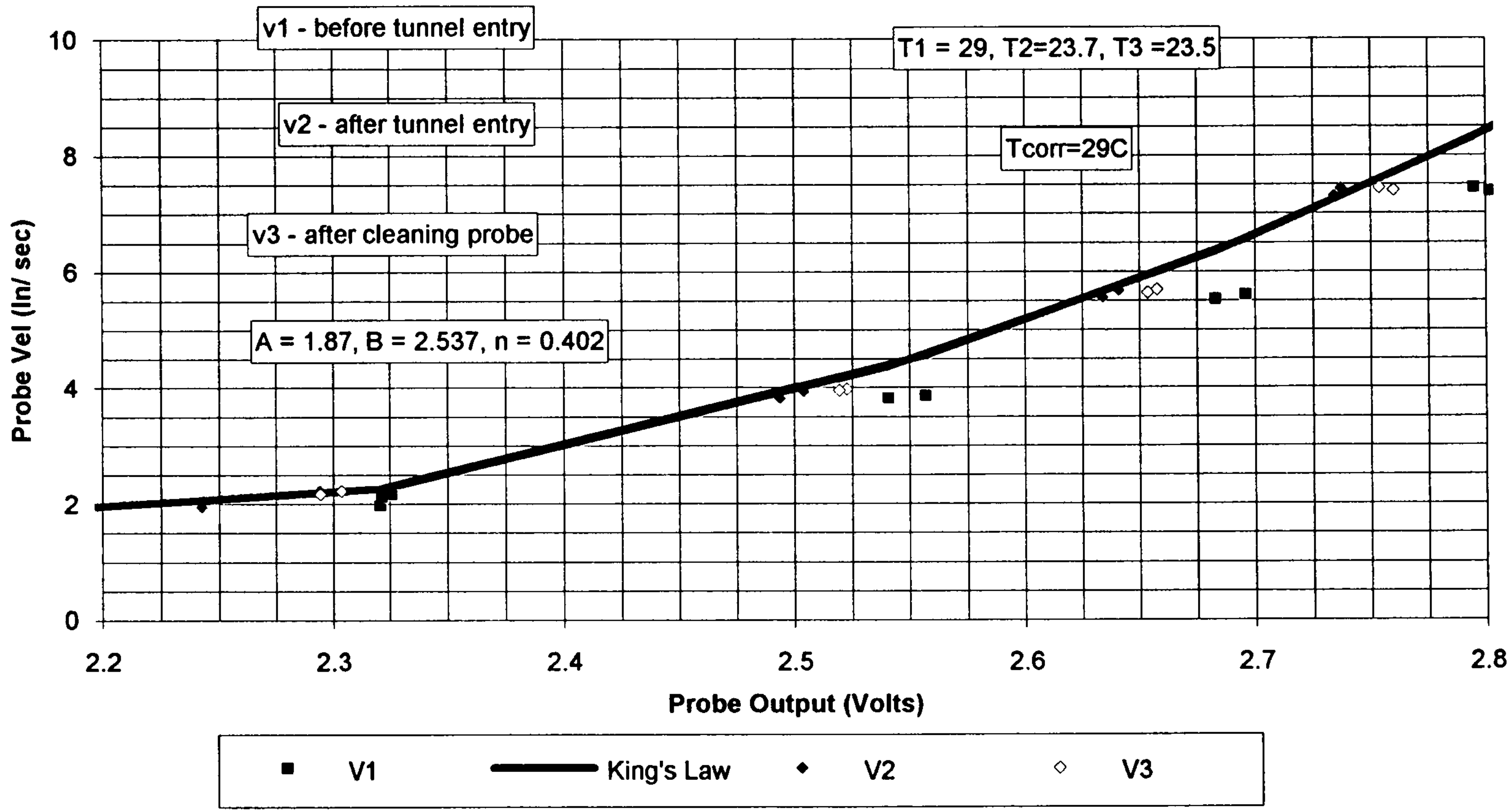

Figure 6-1: Run #6, Velocity Calibration

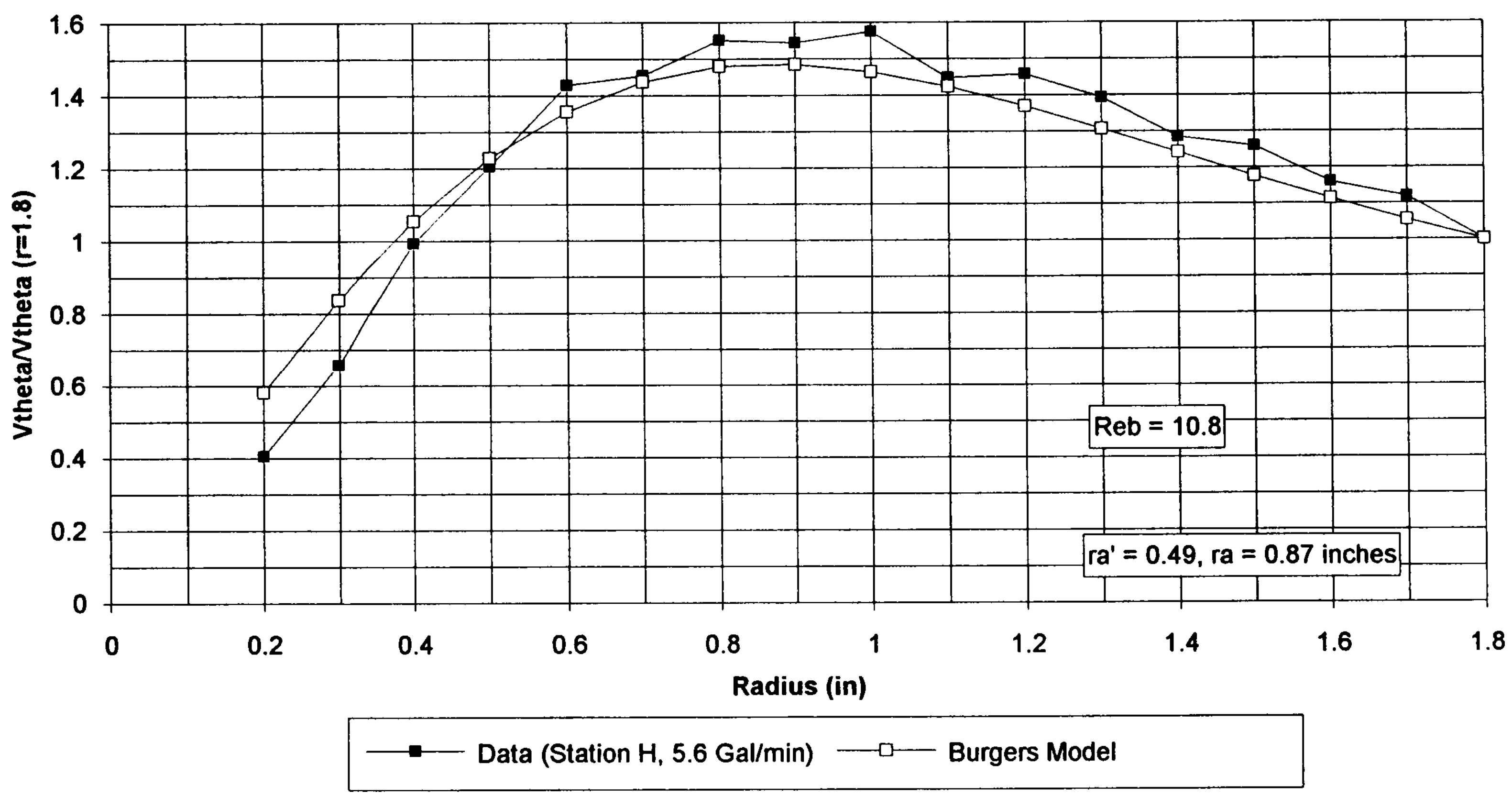

Figure 6-2: Burgers Model, Data Fit

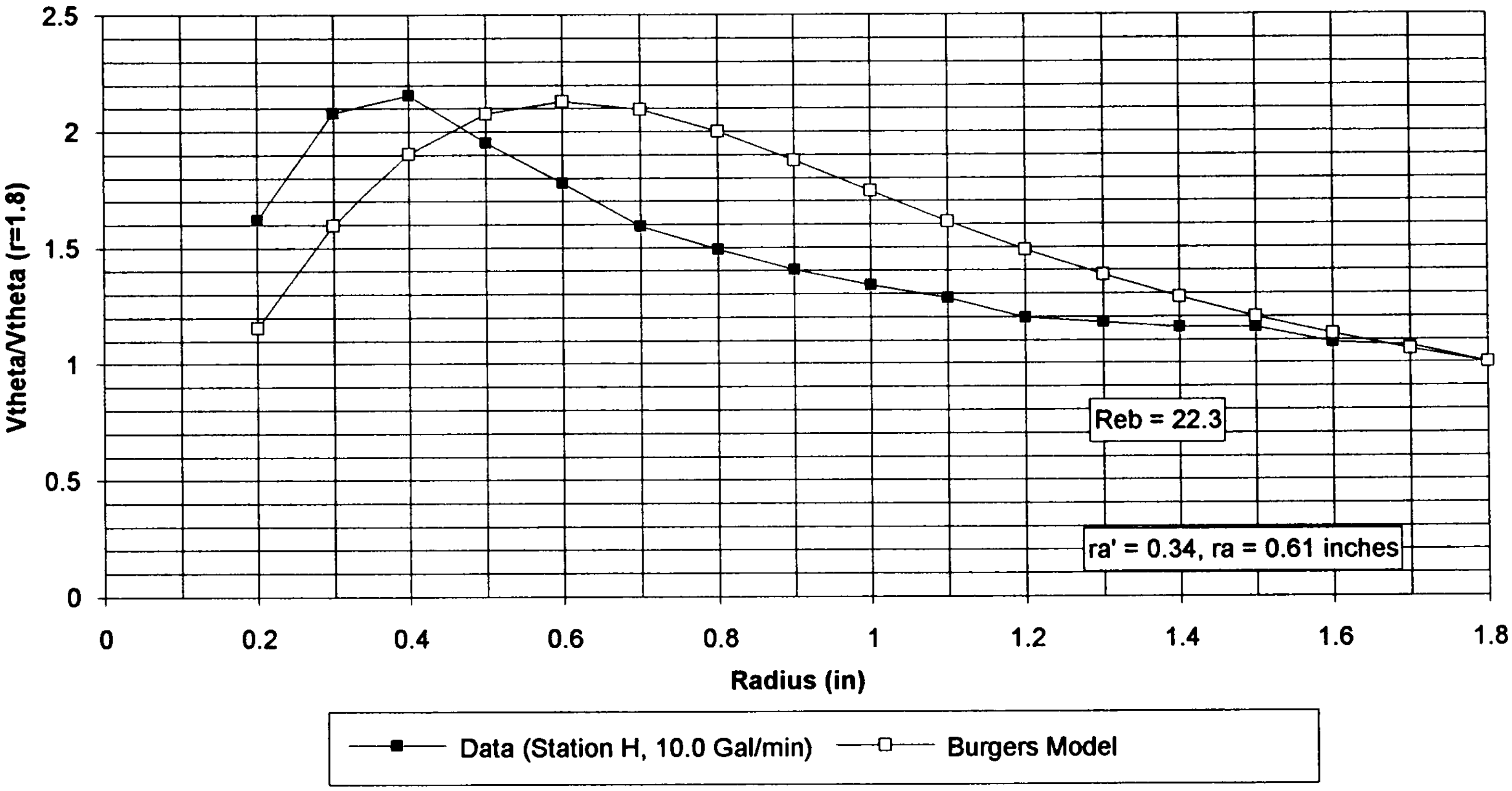

Figure 6-3: Burgers Model, Data Fit (Cont.)

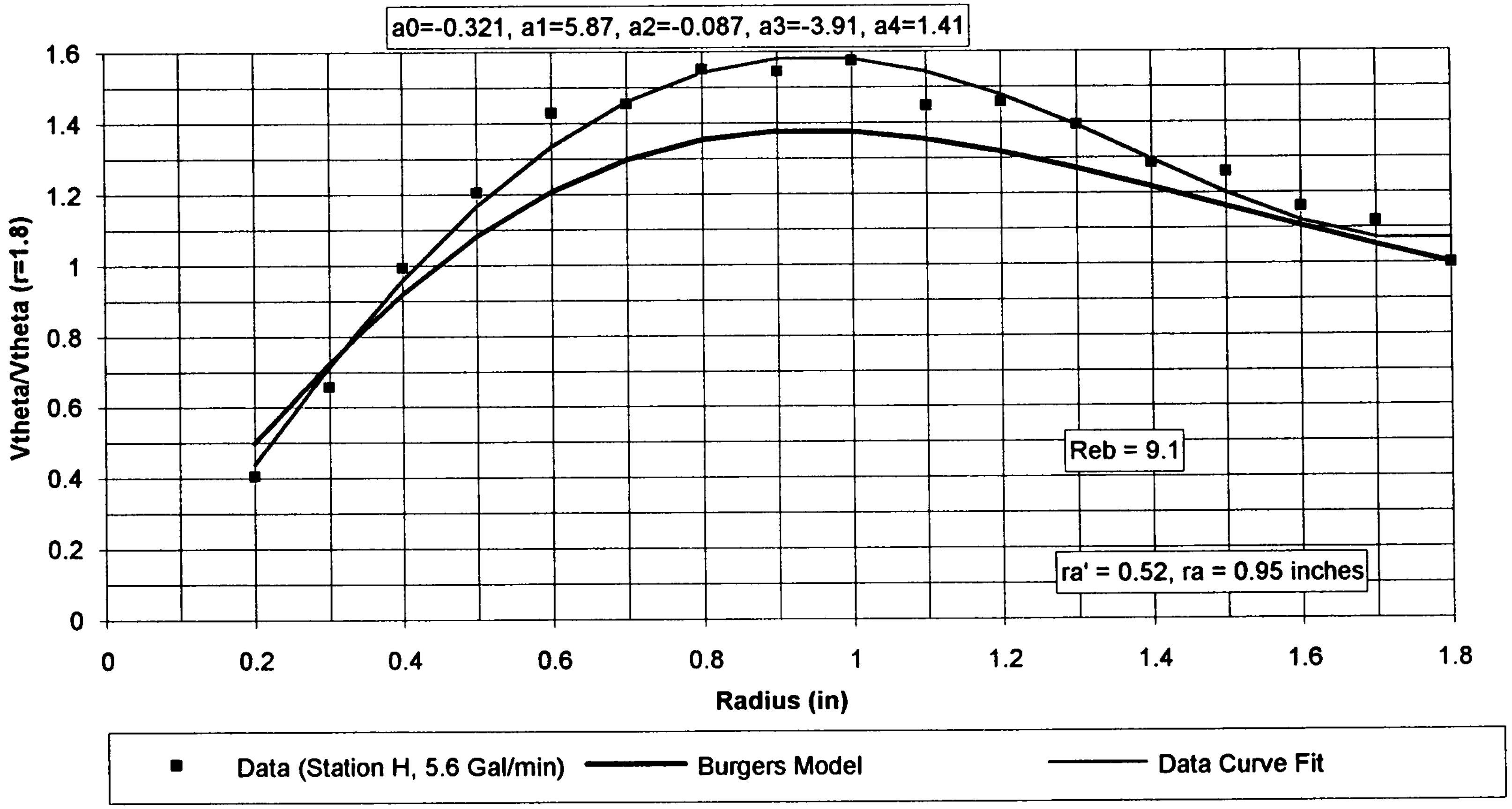

Figure 6-4: Burgers Model, Fixed Radius

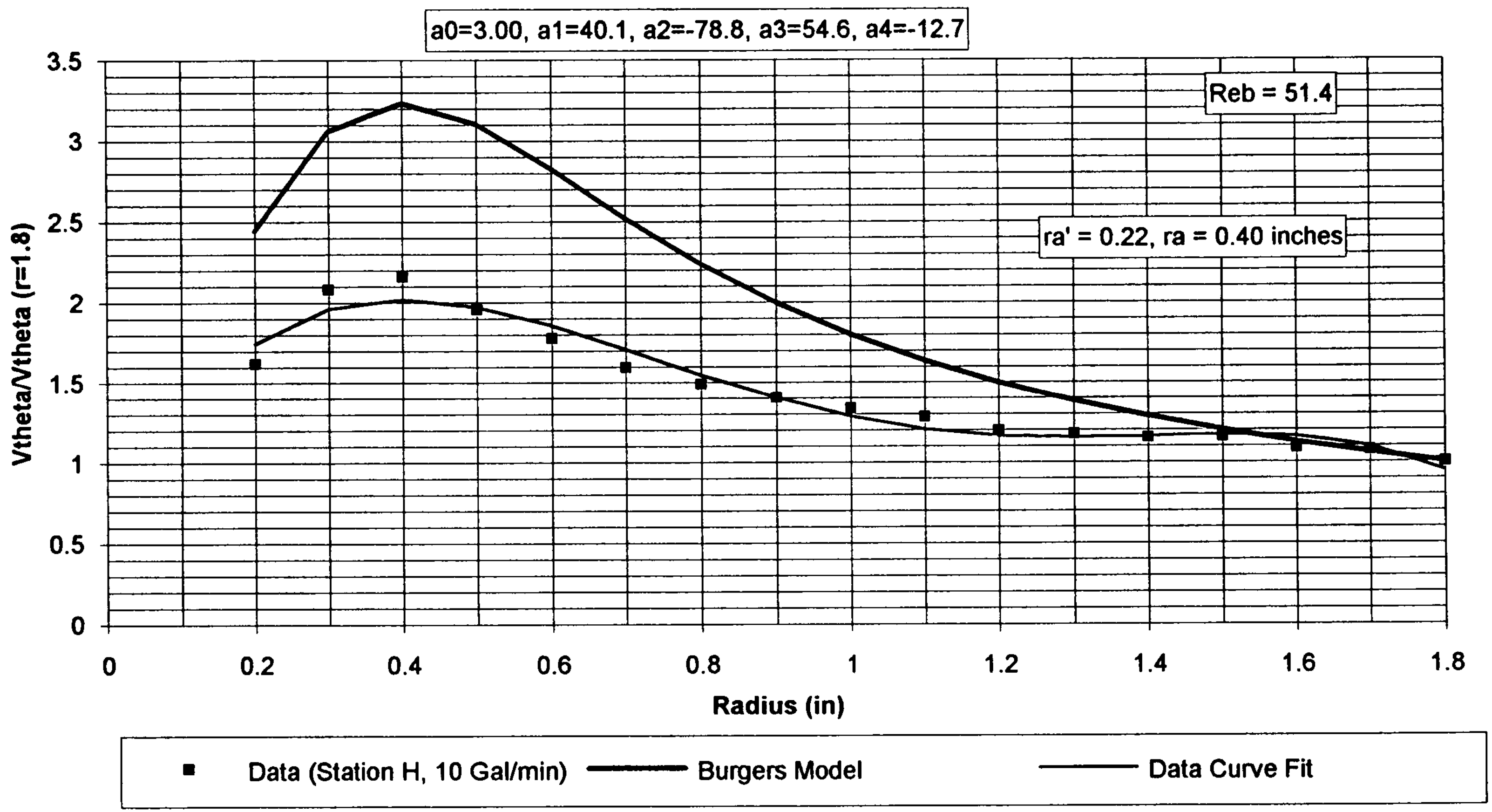

Figure 6-5: Burgers Model, Fixed Radius (Cont.)

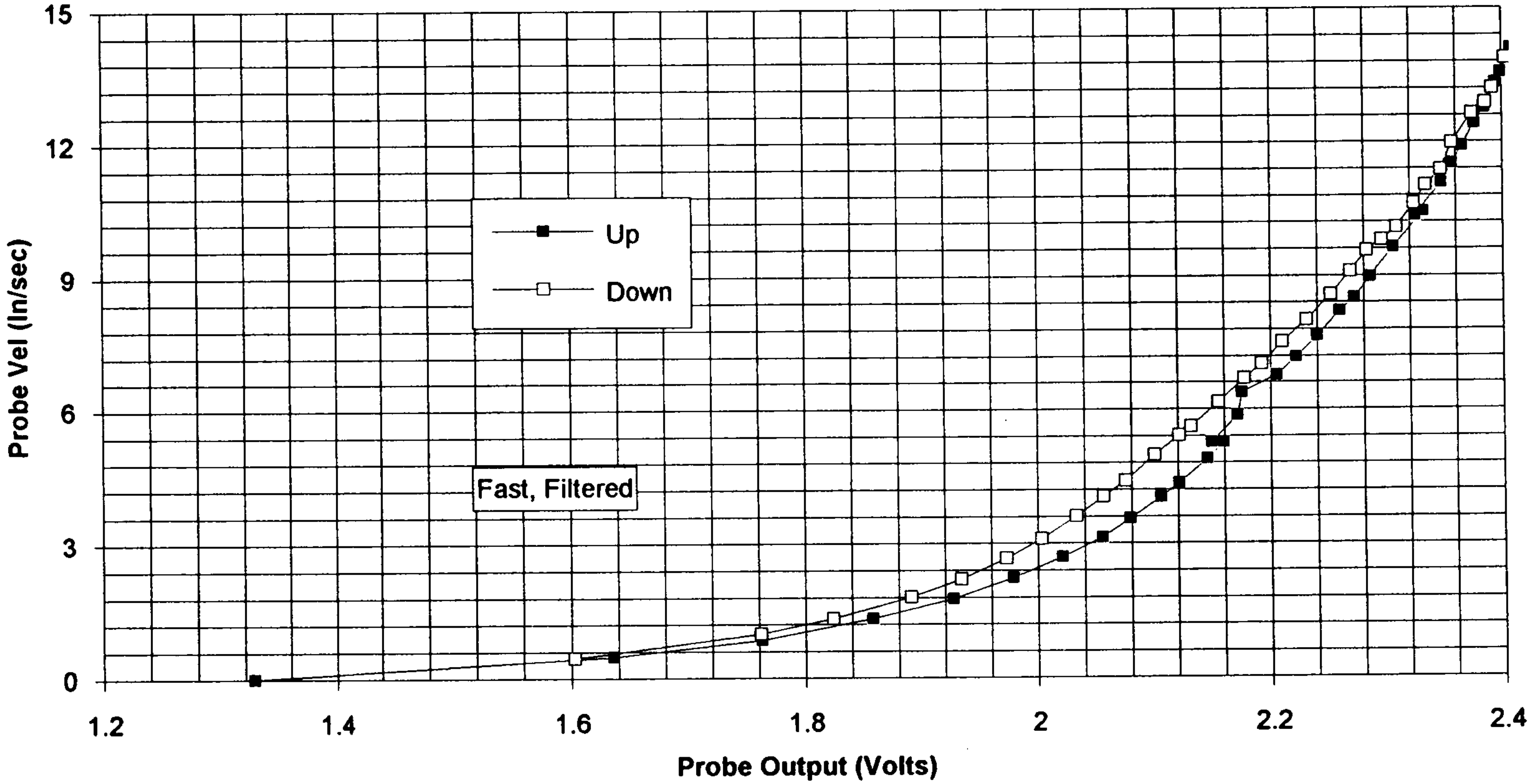

Figure A-1: Velocity Calibration, Hysteresis Error

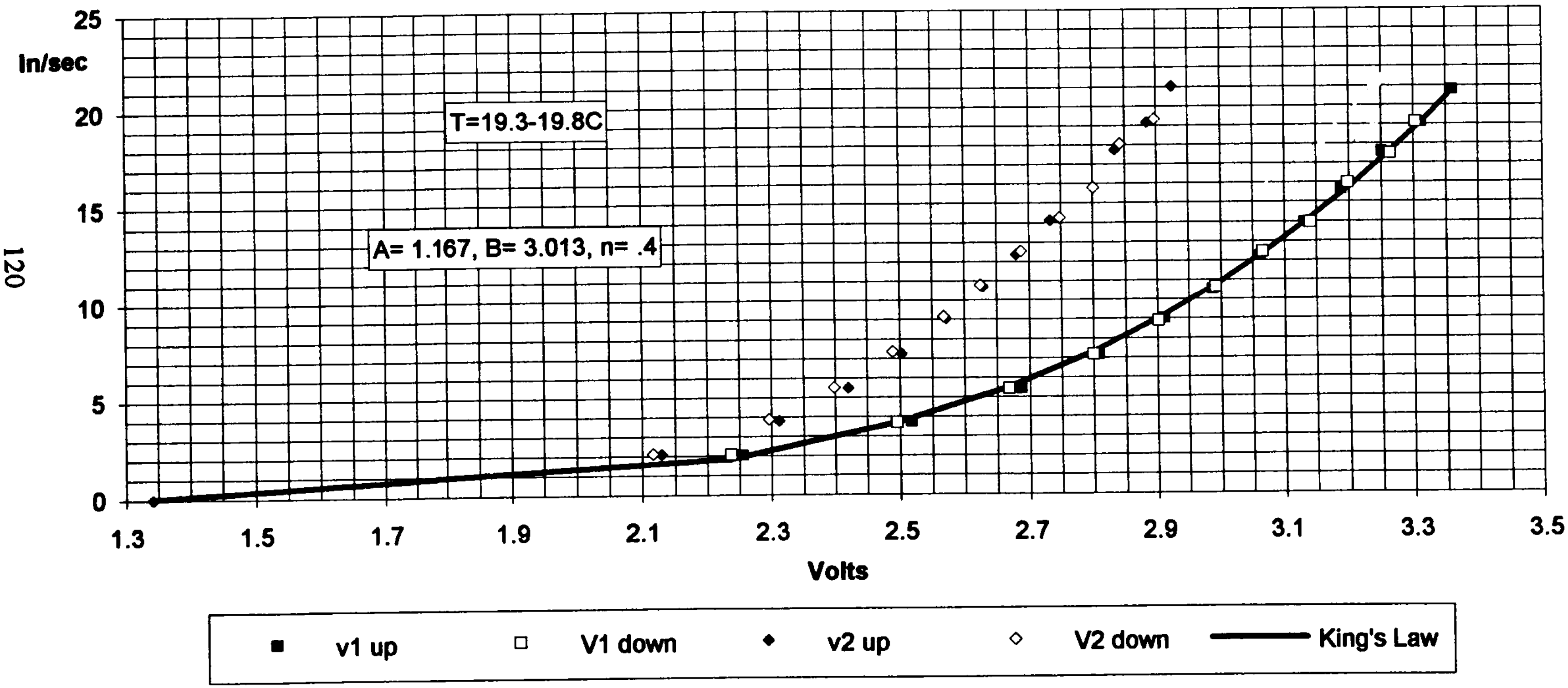

Figure A-2: Velocity Calibration, Repeatability Error

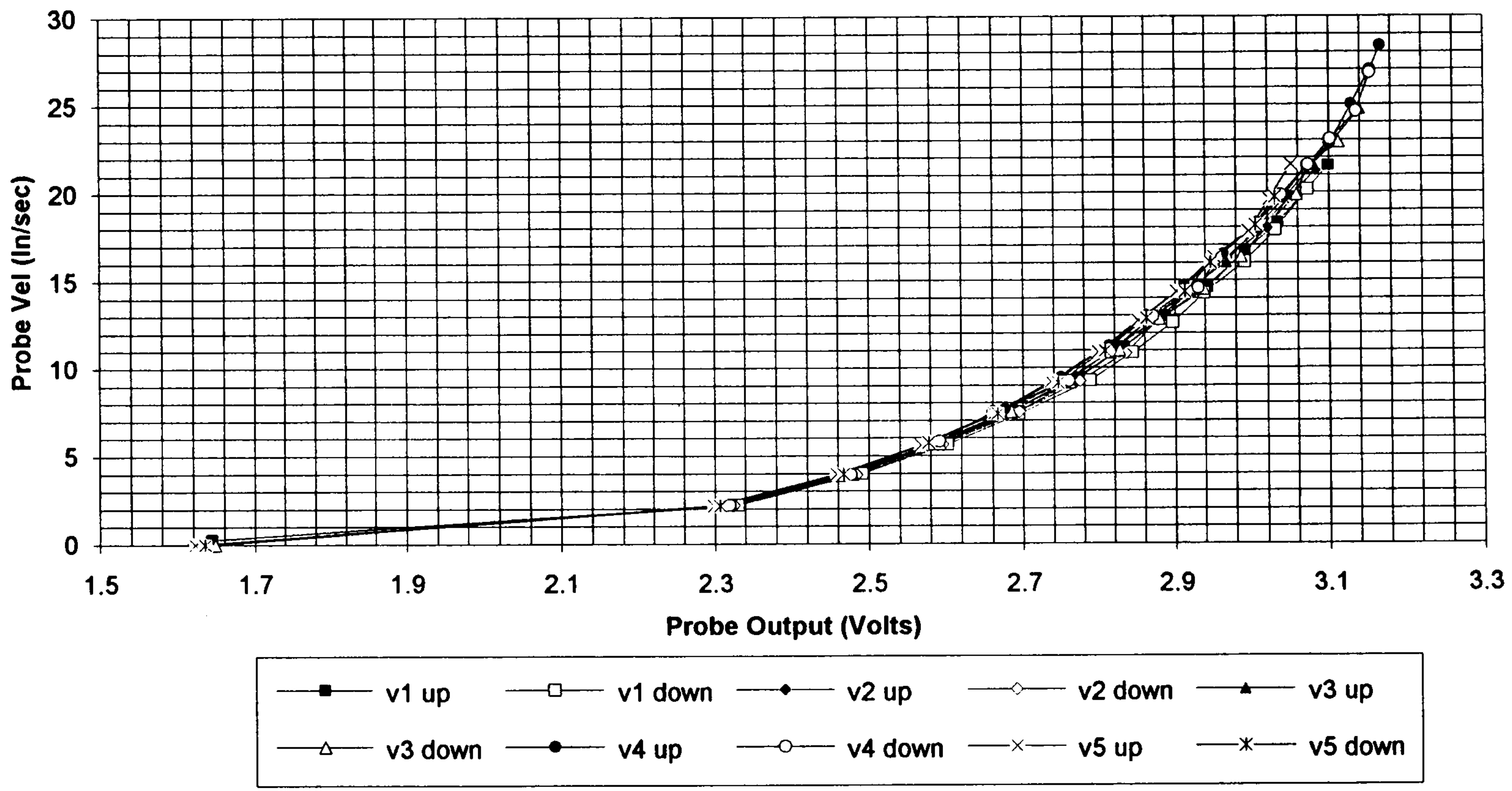

Figure A-3: Multiple Successive Velocity Calibrations

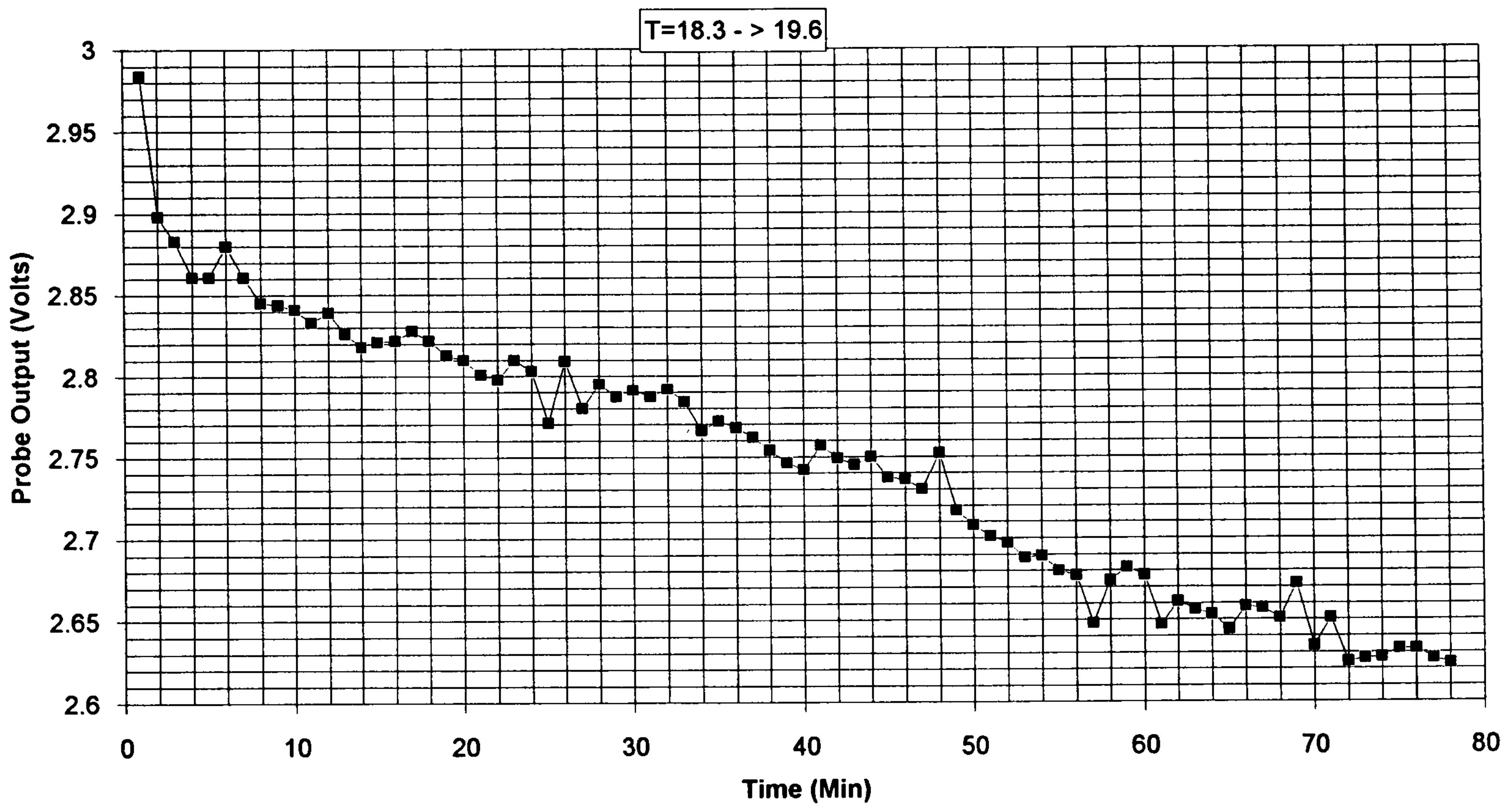

Figure A-4: Velocity Drift: Hot film Output

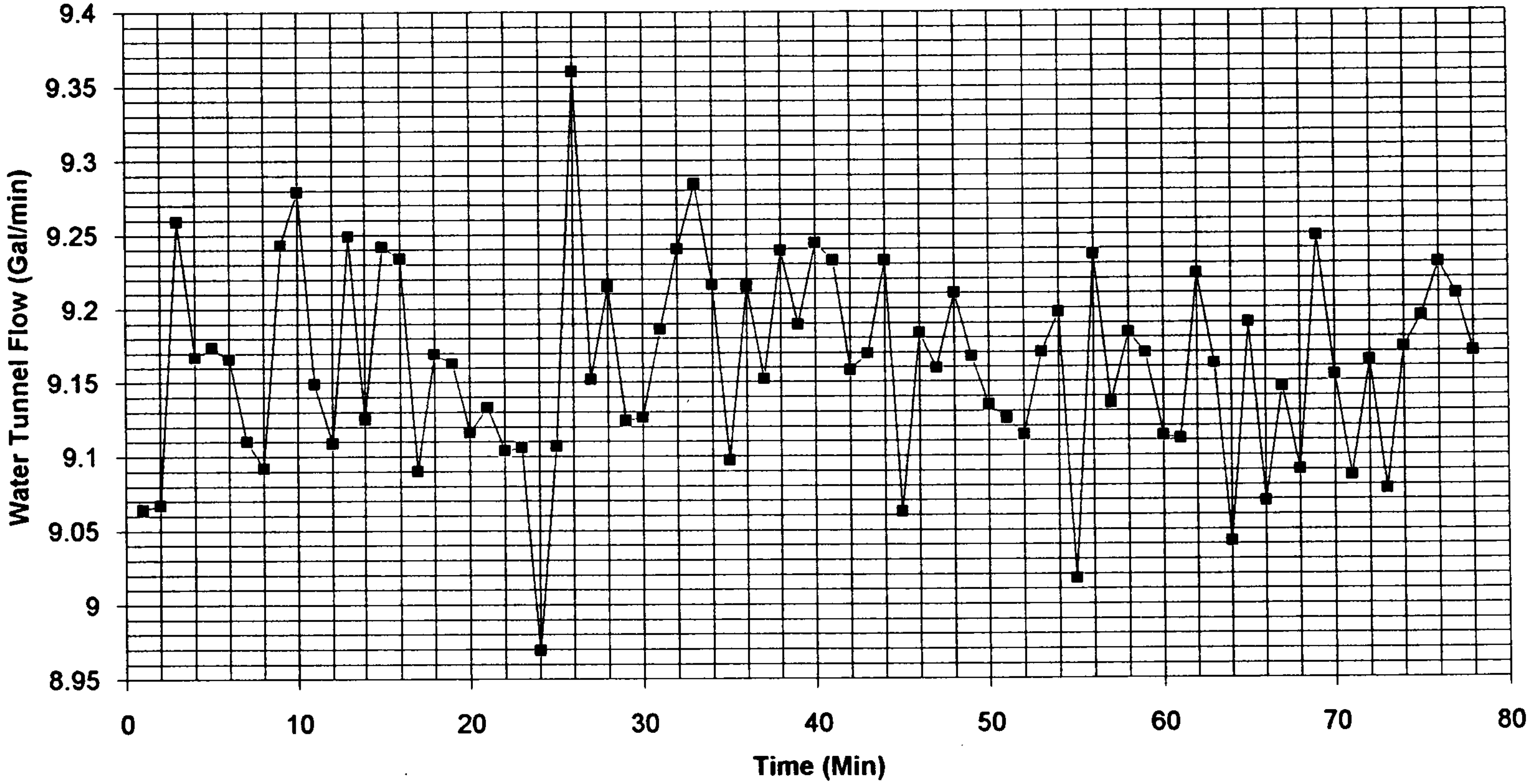

Figure A-5: Velocity Drift: Tunnel Flow Rate

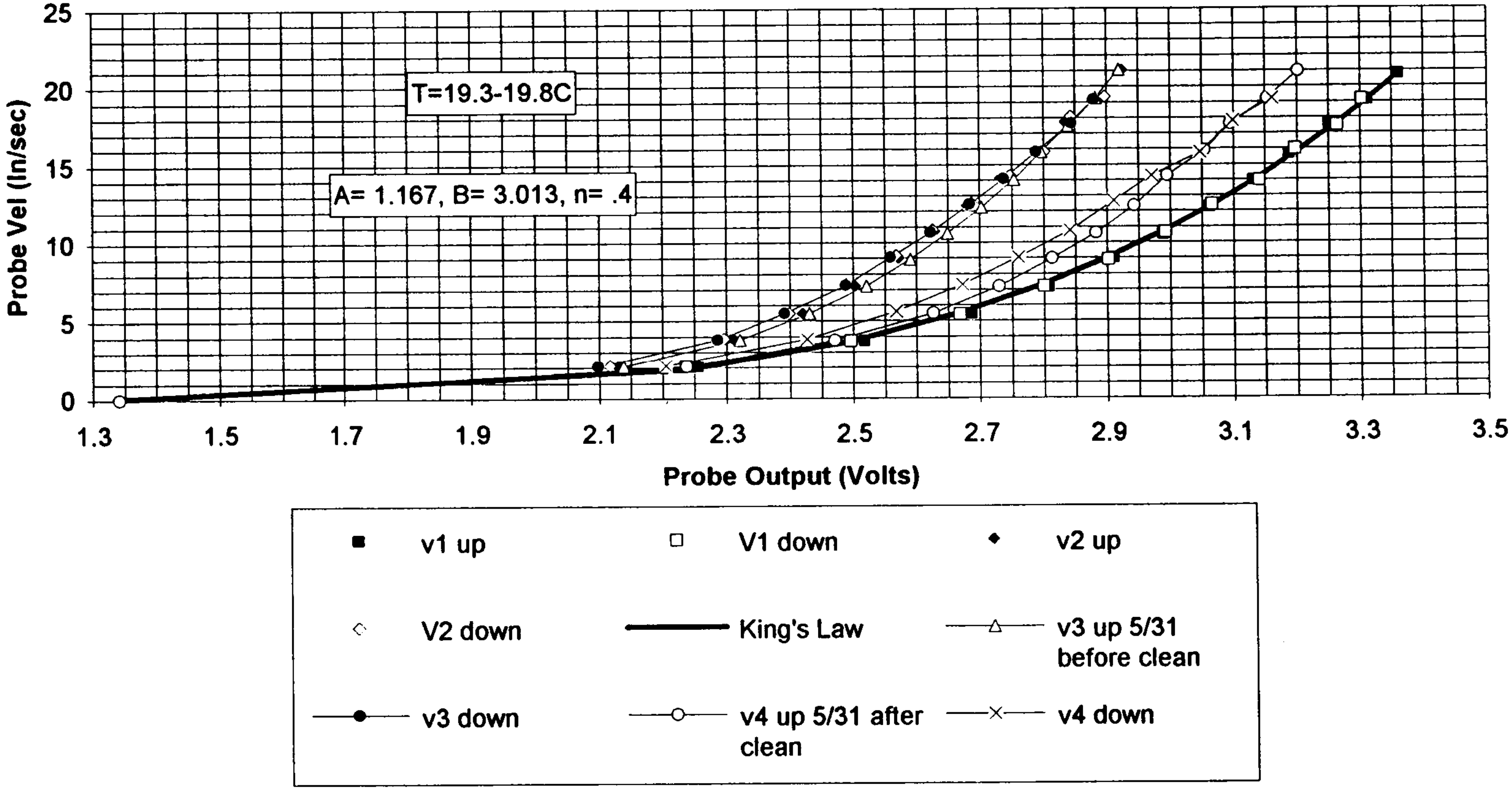

Figure A-6: Effect of Probe Cleaning

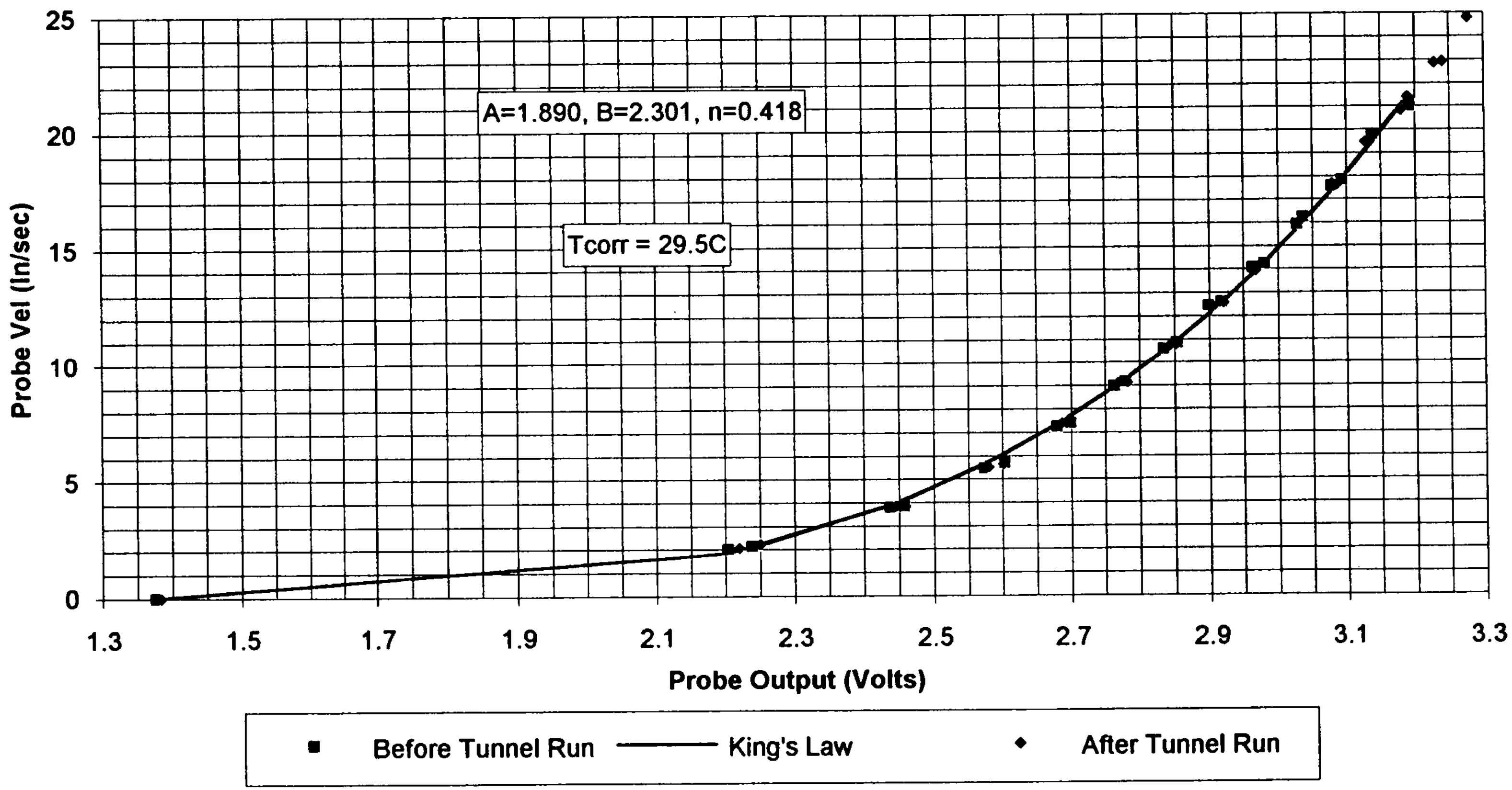

Figure A-7: Typical Accurate Velocity Calibration

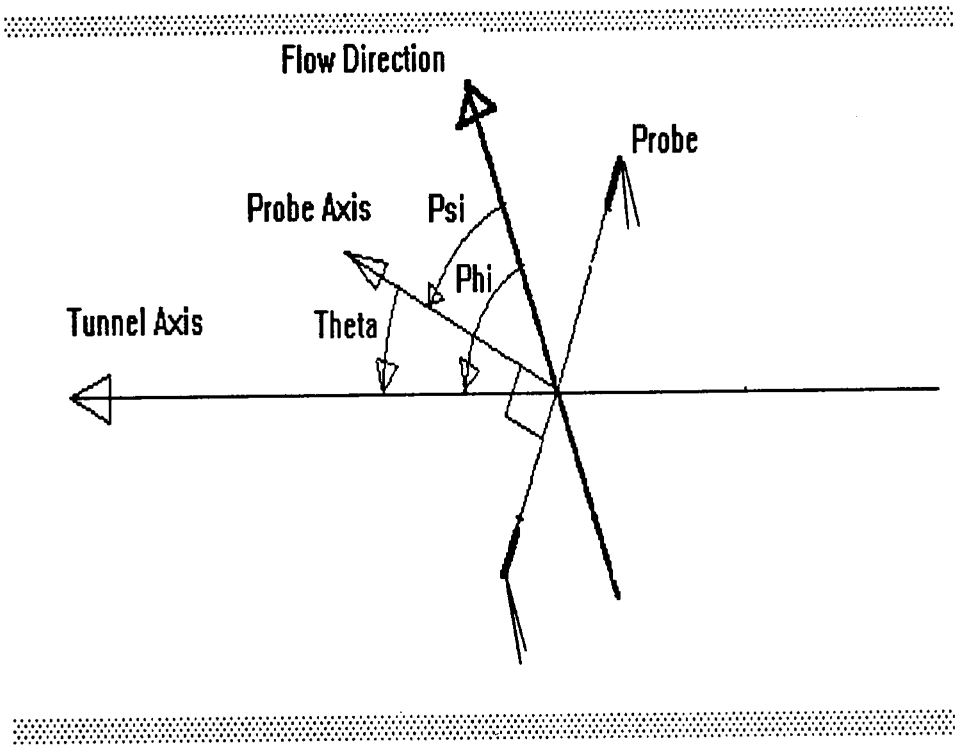

Figure B-1: Probe - Tunnel - Flow Angle Convention

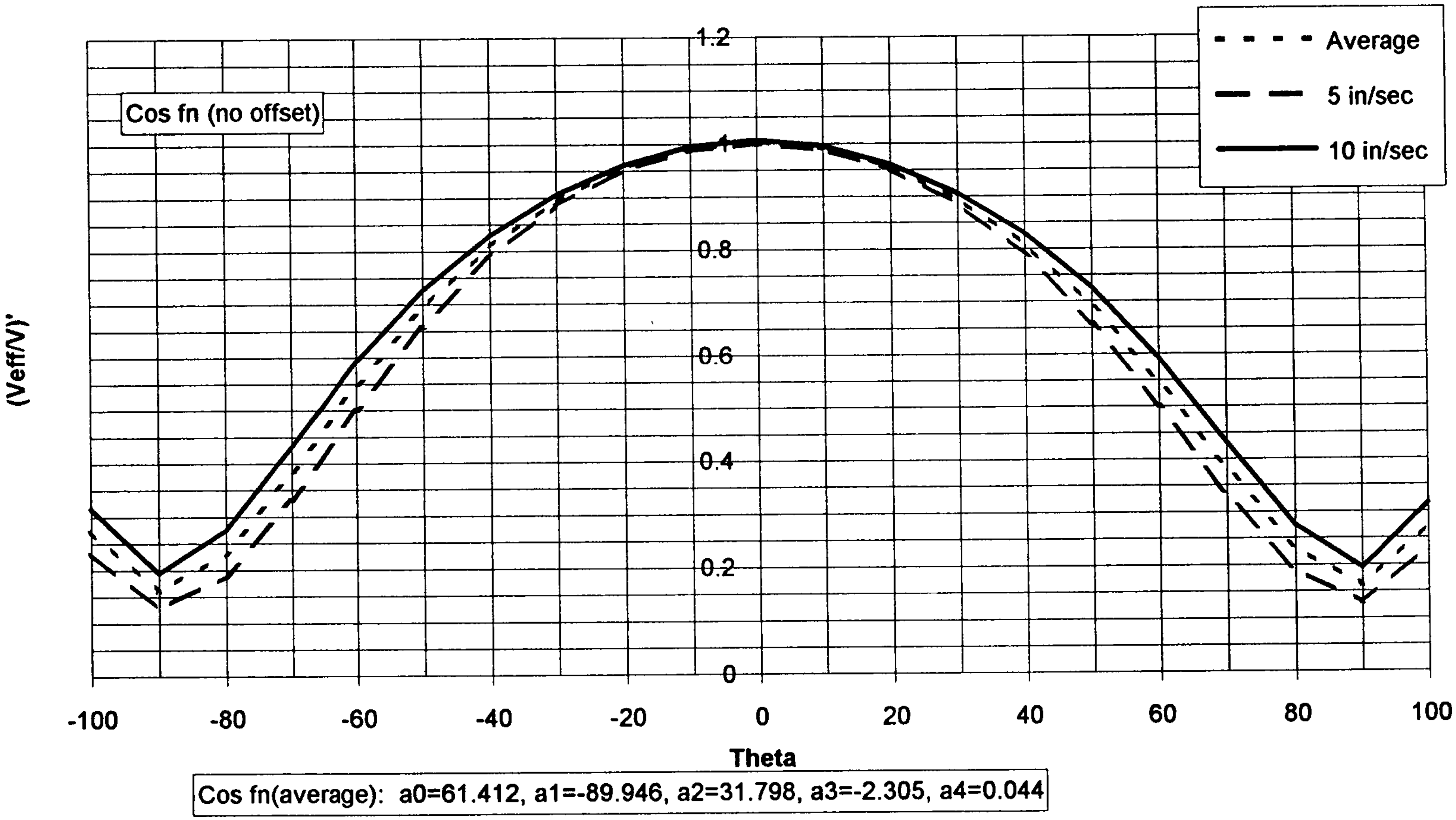

Figure B-2: Yaw Calibration Velocity Sensitivity

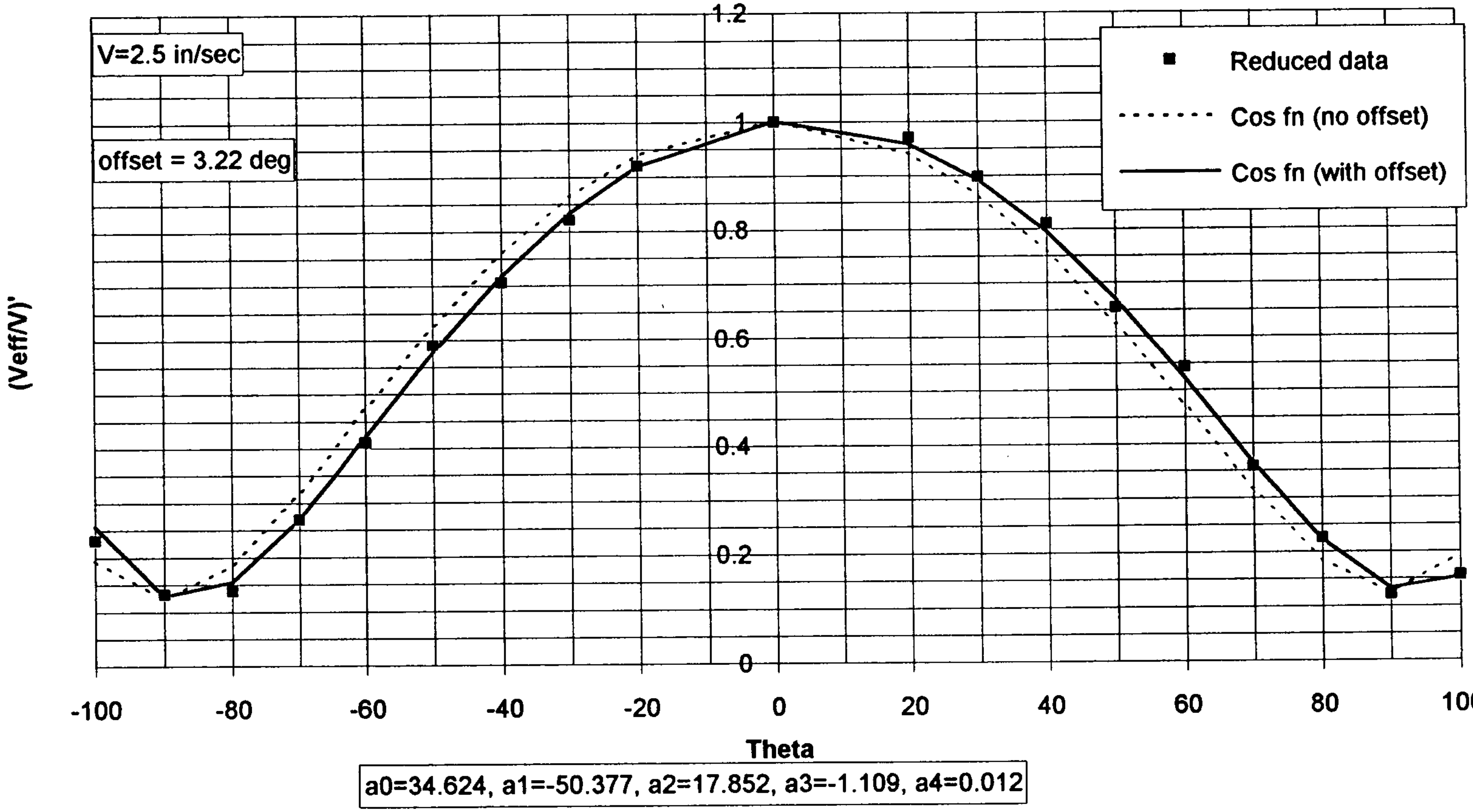

Figure B-3: 2.5 in/sec Yaw Calibration

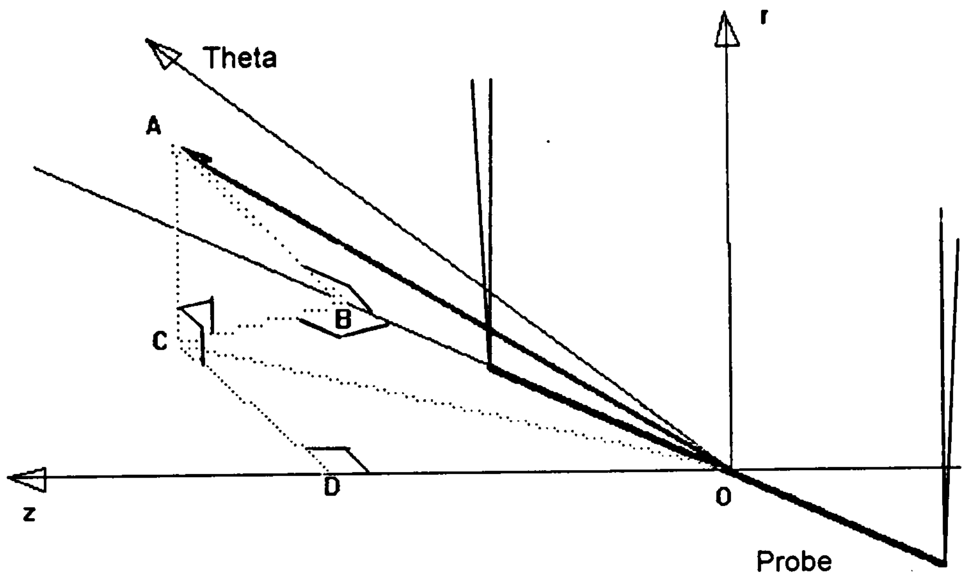

U' = Ray OA
V_r = Ray CA
V_θ = Ray DC (not the same as OB!)
V_z = Ray OD
U = Ray OC, Velocity component in the Θ-Z plane
U'_{perp} = Ray BA
$U'_{parallel}$ = Ray OB
$(\phi-\theta)$ = angle BOC
$(\phi-\theta)'$ = angle BOA

Notes:

The following are right angles: CDO, CBO, ABO, ACD, ACB
The following are <u>not</u> right angles: BOD
The following points are in the Θ-Z plane: B, C, D, O

Figure C-1: Water Tunnel Velocity Field

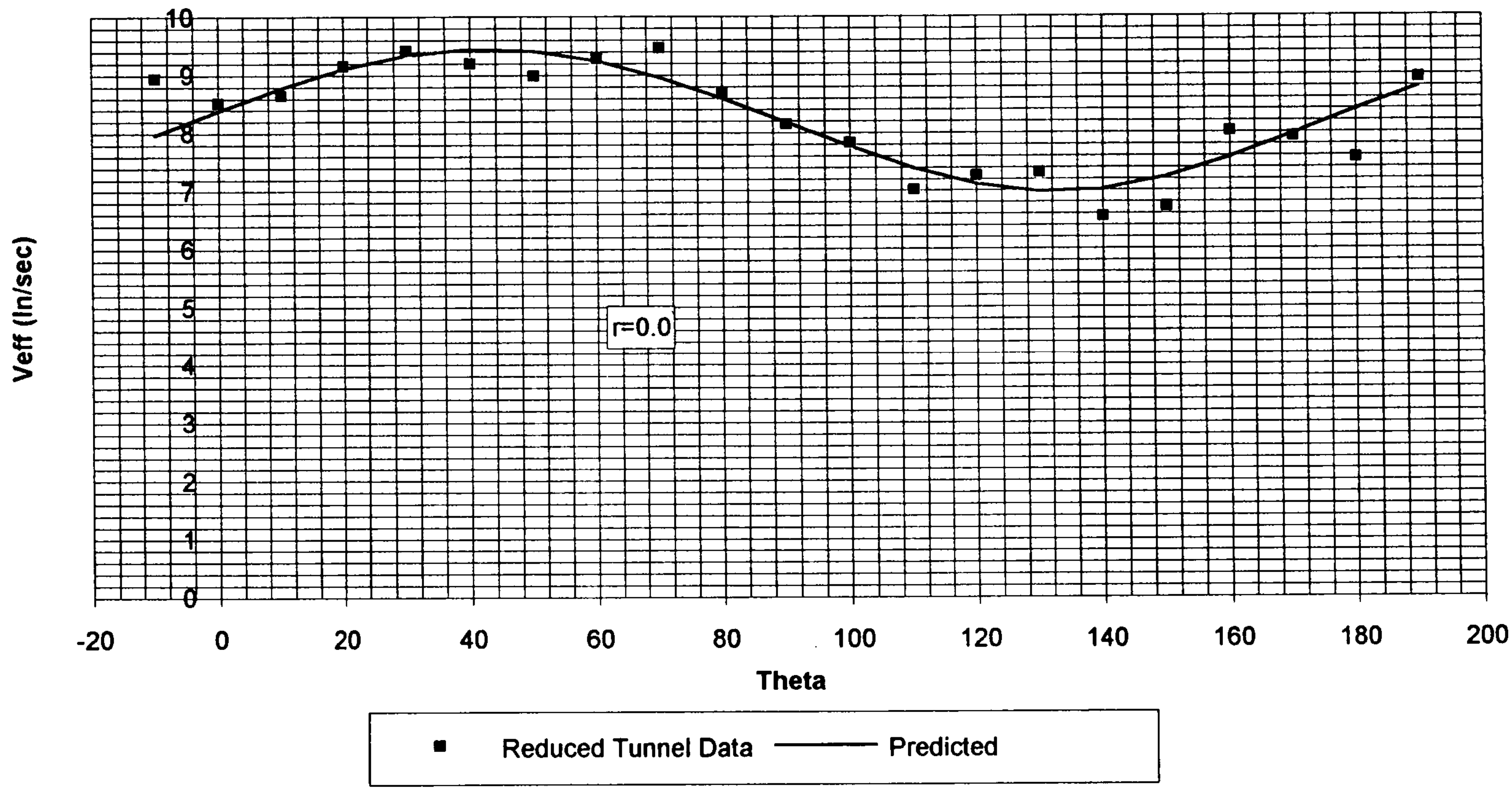

Figure C-2: Run #5, Velocity Reduction Curve fit, r = 0.0 in

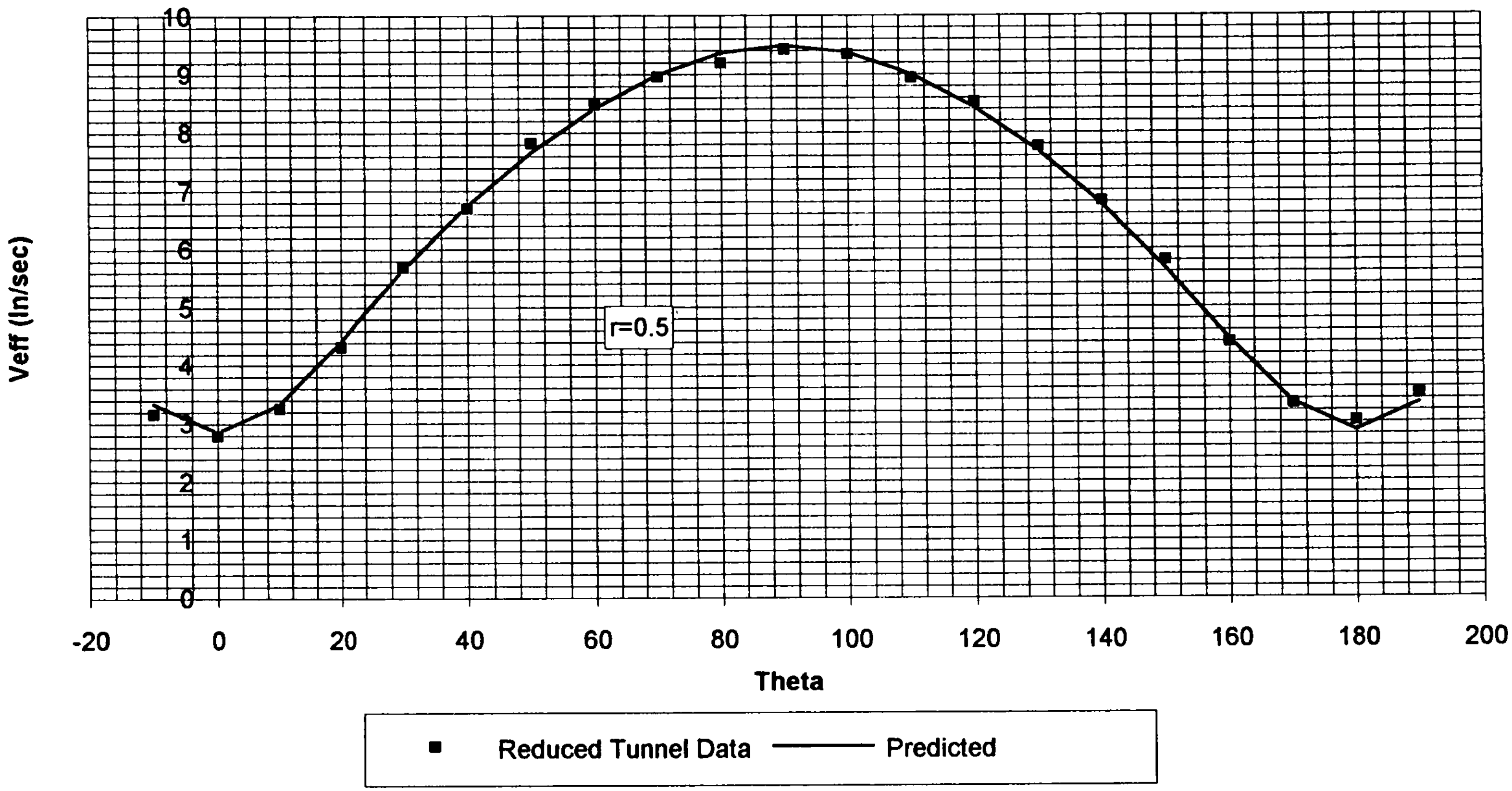

Figure C-3: Run #5, Velocity Reduction Curve fit, r = 0.5 in

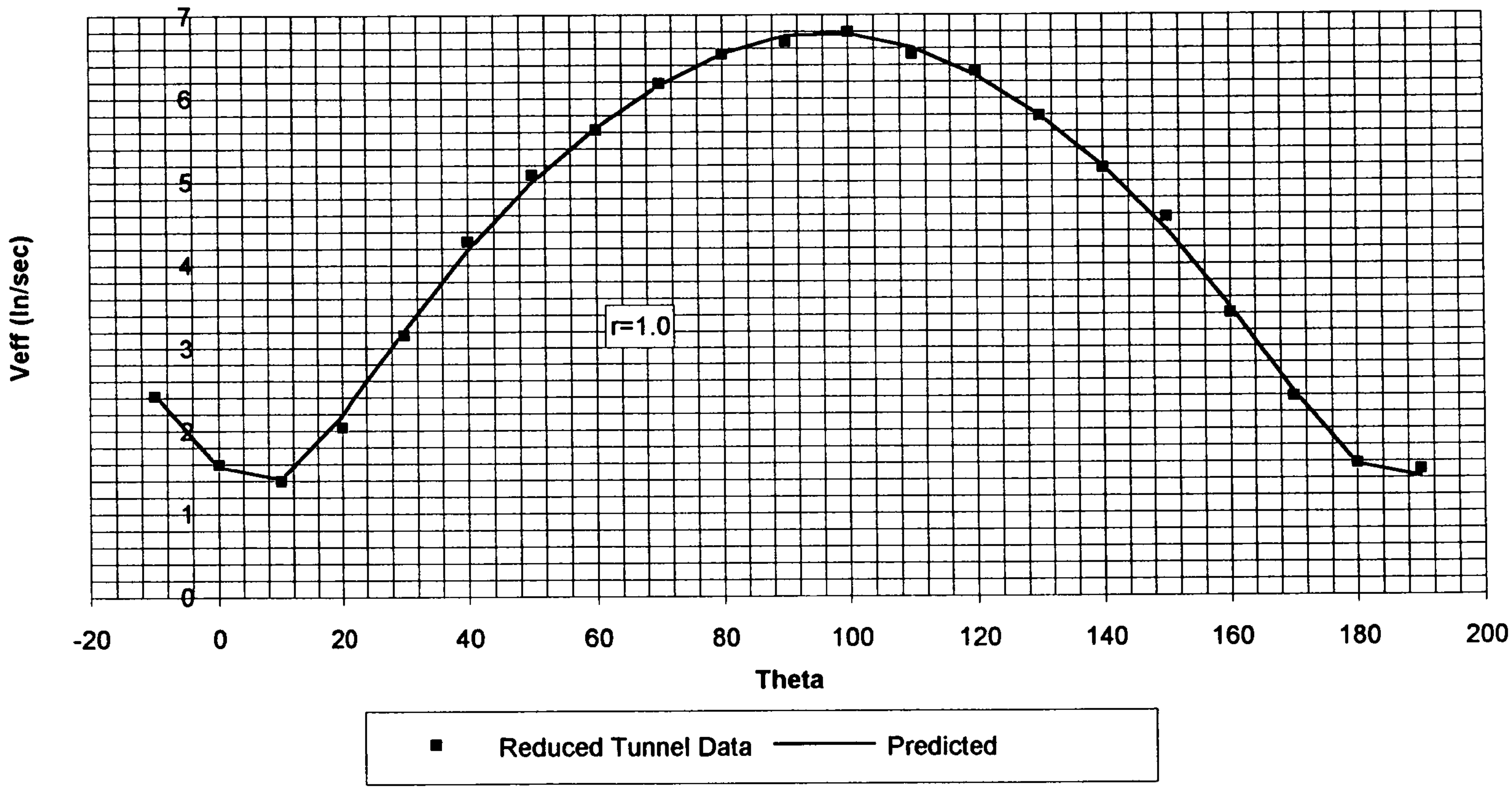

Figure C-4: Run #5, Velocity Reduction Curve fit, r = 1.0 in

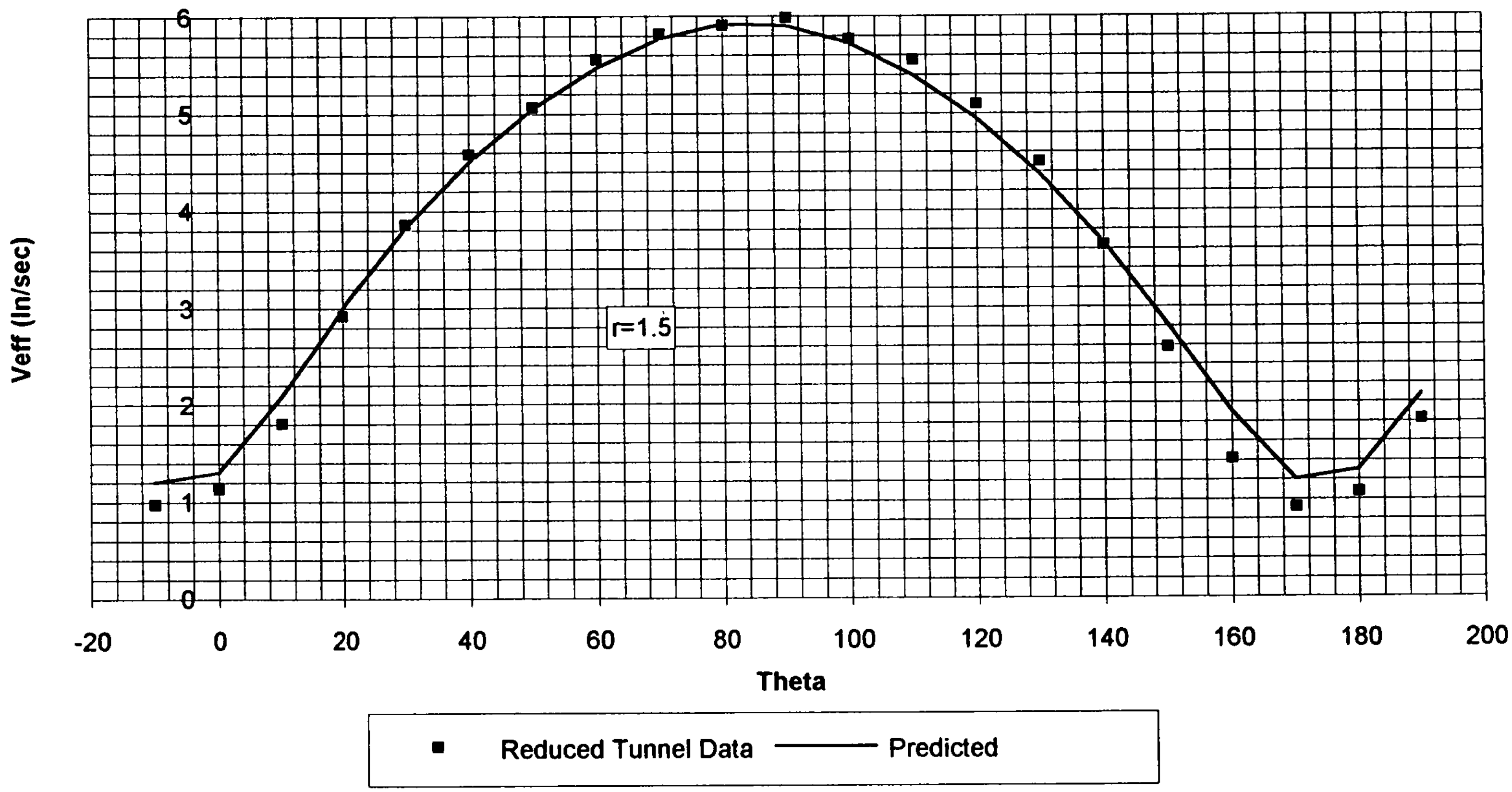

Figure C-5: Run #5, Velocity Reduction Curve fit, r = 1.5 in

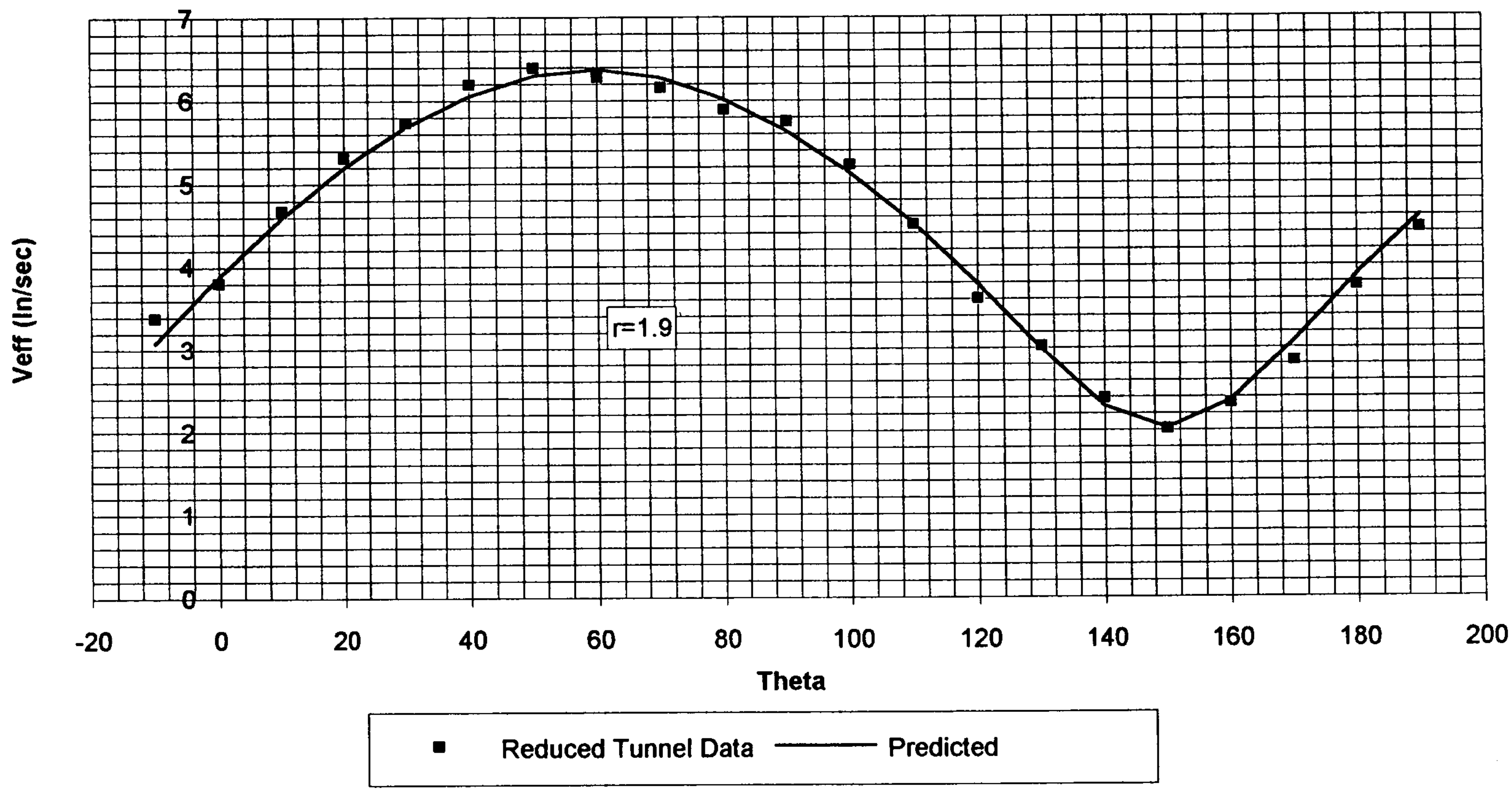

Figure C-6: Run #5, Velocity Reduction Curve fit, r = 1.9 in

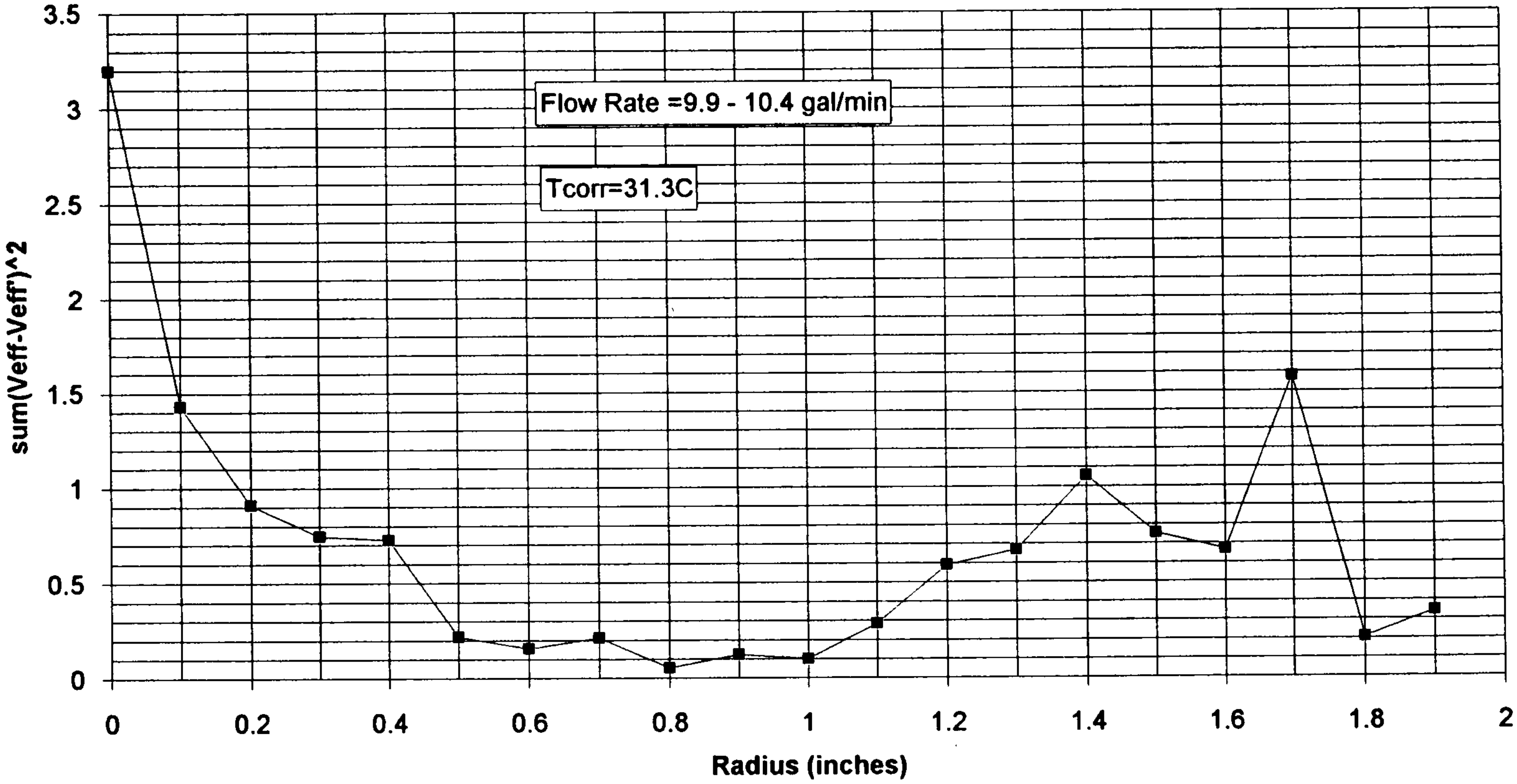

Figure C-7: Run#5, Least Squares Deviation

VITA

Scott Glenfield Tennent was born in Steven's Point, Wisconsin on January 23, 1967. He attended elementary schools in the State College, Pennsylvania area and graduated from State College Area High School in June, 1985. The following September he entered the Massachusetts Institute of Technology as a four-year USAF ROTC scholarship recipient. In May 1989, he received the degree of Bachelor of Science in Aeronautical Engineering and was commissioned in the USAF as a Second Lieutenant.

He was assigned to Arnold Engineering Development Center, Arnold Air Force Base, Tullahoma, Tennessee, in November 1989. Concurrently, he studied at the University of Tennessee Space Institute and received a Master of Science Degree in Aerospace Engineering in December 1993.